NACA RM L56A26

NACA

RESEARCH MEMORANDUM

A TRANSONIC WIND-TUNNEL INVESTIGATION OF STORE AND HORIZONTAL-TAIL LOADS AND SOME EFFECTS OF FUSELAGE-AFTERBODY MODIFICATIONS ON A SWEPT-WING FIGHTER AIRPLANE

By Joseph M. Hallissy, Jr., and Louis Kudlacik

Langley Aeronautical Laboratory
Langley Field, Va.

NATIONAL ADVISORY COMMITTEE
FOR AERONAUTICS

WASHINGTON

April 10, 1956
Declassified May 16, 1958

NATIONAL ADVISORY COMMITTEE FOR AERONAUTICS

RESEARCH MEMORANDUM

A TRANSONIC WIND-TUNNEL INVESTIGATION OF STORE AND HORIZONTAL-TAIL LOADS AND SOME EFFECTS OF FUSELAGE-AFTERBODY MODIFICATIONS ON A SWEPT-WING FIGHTER AIRPLANE

By Joseph M. Hallissy, Jr., and Louis Kudlacik

SUMMARY

An investigation has been conducted in the Langley 16-foot transonic tunnel on a model of a swept-wing fighter airplane to determine:

(a) Store and pylon loads and the effect of the store installation on drag and stability

(b) Horizontal-tail loads at sideslip angles of 0° and 5°

(c) The extent of drag-rise reductions possible by enlarging the fuselage afterbody to improve the cross-sectional-area progression

The investigation covered Mach numbers from 0.80 to 1.03, angles of attack to 17°, and sideslip angles of 0° and $\pm 5^\circ$. The wing had 40° sweepback, an aspect ratio of 3.43, a taper ratio of 0.578, and NACA 64A010 airfoil sections perpendicular to the quarter chord.

The store and pylon installation increased the drag coefficient 25 to 50 percent throughout the test Mach number range and decreased the directional stability as much as 20 percent. The side load on the store varied markedly with sideslip angle but little with angle of attack. On the pylon the side load was dependent on both sideslip angle and angle of attack. At the lower Mach numbers and higher test angles of attack, the horizontal-tail asymmetric bending moments became severe in the sideslip condition. Because of the influence of the downwash field, the distribution of load on the horizontal tail was such that relatively large hinge moments could exist for small total tail loads. The afterbody modifications decreased the transonic drag coefficient up to 0.01, but caused increases in the drag coefficient at Mach numbers below 0.92.

INTRODUCTION

Of frequent concern to the designer of military aircraft are the following two problems:

(a) What are the aerodynamic penalties and loads associated with the installation of large external stores?

(b) What horizontal-tail loads will be encountered within the operating range of the airplane?

Although information on problem (a) is becoming more available as the results of various stores research programs are reported, information in the transonic speed range is still limited. Some store force and moment data at these speeds are given in reference 1; however, only a few data are available giving detailed load distribution on the store. Reference 2, for example, gives some data from flight measurements on a fineness-ratio-5 store at moderately high subsonic speeds.

The total horizontal-tail loads for an airplane can be estimated and are usually determined in developmental wind-tunnel testing. The span load distributions, however, are less frequently resolved. Due to the flow field in which the horizontal-tail surfaces operate, their span loadings may be of unusual shape. For some recent designs with all-movable swept tail surfaces this has resulted in some unexpectedly large hinge moments even for small total tail loads. An additional problem arising from flow field irregularities may be large asymmetric tail loading in sideslip. For some types of attachment (as to a thin vertical fin) the resulting root bending moment could be a critical design condition.

In a recent test program completed in the Langley 16-foot transonic tunnel a swept-wing fighter model was instrumented for both force and pressure measurements so that some detailed information on these problems could be obtained. This report presents these results and also the results of an effort to reduce the transonic drag rise (at Mach number 1.0) by enlarging the fuselage afterbody so as to improve the cross-sectional-area progression of the model.

The tests covered Mach numbers from 0.80 to 1.03, angles of attack to 17°, and angles of sideslip of 0° and ±5°.

SYMBOLS

The model forces and moments are presented using the stability axis system. (See fig. 1.) The origin is a point in the plane of symmetry

opposite $0.21\bar{c}$ and located $0.0103\bar{c}$ below the fuselage center line. (See fig. 2.)

Store forces and moments are presented using a body axis system with the x-axis along the store center line and the origin at 50 percent of the store length.

The symbols used are defined as follows:

C_L lift coefficient, $\frac{\text{Lift}}{qS}$

C_D drag coefficient, $\frac{\text{Drag}}{qS}$

C_m pitching-moment coefficient, $\frac{\text{Pitching moment}}{qS\bar{c}}$

C_l rolling-moment coefficient, $\frac{\text{Rolling moment}}{qSb}$

C_n yawing-moment coefficient, $\frac{\text{Yawing moment}}{qSb}$

C_Y lateral-force coefficient, $\frac{\text{Lateral force}}{qS}$

C_{l_β} $\frac{\partial C_l}{\partial \beta} \times 57.3$, average value over the sideslip range

C_{n_β} $\frac{\partial C_n}{\partial \beta} \times 57.3$, average value over the sideslip range

C_{Y_β} $\frac{\partial C_Y}{\partial \beta} \times 57.3$, average value over the sideslip range

C_{N_s} store normal-force coefficient, $\frac{\text{Normal force}}{q\pi R^2}$

C_{Y_s} store lateral-force coefficient, $\frac{\text{Lateral force}}{q\pi R^2}$

C_{m_s} store pitching-moment coefficient, $\frac{\text{Pitching moment}}{q\pi R^2 l_s}$

C_{n_s} store yawing-moment coefficient, $\frac{\text{Yawing moment}}{q\pi R^2 l_s}$

c_{n_s} store section normal-force coefficient, $\frac{\text{Normal force per foot of length}}{qr}$

c_{y_s} store section lateral-force coefficient, $\frac{\text{Lateral force per foot of length}}{qr}$

$C_{B_{(R-L)}}$ net bending-moment coefficient at the horizontal tail attachment, $\frac{\text{(Right bending moment - Left bending moment)}}{q\frac{S_t}{2}\frac{b_t}{2}}$

C_{N_t} horizontal-tail normal-force coefficient, $\frac{\text{Normal force}}{qS_t}$

C_h horizontal-tail hinge-moment coefficient referred to the hinge axis (see fig. 1), $\frac{\text{Hinge moment}}{qc_t^2 b_t}$

c_{n_t} horizontal-tail section normal-force coefficient, $\frac{\text{Normal force per foot of span}}{qc_t}$

c_n wing section normal-force coefficient, $\frac{\text{Normal force per foot of span}}{qc}$

c_{y_p} pylon section load coefficient, $\frac{\text{Force per foot of span}}{qc_p}$

A model cross-sectional area, normal to fuselage center line

b wing span

b_t horizontal-tail span

c wing local chord

c_{av} average wing chord

$\bar{c}$ mean aerodynamic chord, $\frac{2}{S}\int_0^{b/2} c^2 dy$

c_p pylon chord

c_t horizontal-tail chord

i_t	horizontal-tail incidence (angle with respect to fuselage center line)
l_f	fuselage length
l_t	tail length, 0.21 $\bar{c}$ of wing to 0.25 $\bar{c}$ of horizontal tail
l_s	store length
P_b	base pressure coefficient, $\frac{p_b - p_o}{q}$
p_b	static pressure at model base
p_o	free-stream static pressure
q	free-stream dynamic pressure
R	maximum store radius
r	local store radius
S	wing area
S_t	horizontal-tail area
x	streamwise distance from the wing leading edge
x_f	distance from the nose of the fuselage
x_p	streamwise distance from the pylon leading edge
x_s	distance from the nose of the store
y	perpendicular distance from the plane of symmetry
α	angle of attack, referred to fuselage center line, deg
α_t	section angle of attack of the horizontal tail, $\alpha + i_t$ - local downwash angle, deg
β	sideslip angle, deg

MODEL AND INSTRUMENTATION

Model

Geometric details and dimensions of the model are given in figure 2. The term "basic model" in this report is used to indicate the configuration as shown in figure 2 less pylon and store. Some additional information on the location of the store is as follows: the 46.66-percent center-line point of the store is located 1.43 maximum store diameters directly below the wing quarter-chord point at the 0.218-semispan station.

Figure 3 indicates the various fuselage shape modifications. The "original fuselage shape" is included for reference only, since it was not one of the configurations tested. (An enlarged afterbody was required for the sting mounting.) The original nose inlet is also indicated for reference only, since all tests were made with the faired nose section installed. Two modifications to the fuselage afterbody shape and one to the wing-fuselage juncture were tried in the program to reduce the transonic drag rise by improving the model cross-sectional-area progression. Only the larger of the two afterbody modifications tested, or the "full afterbody modification," is indicated in figure 3. This modification was intended to provide the most favorable cross-sectional-area distribution, as shown in figure 4. The smaller, or "75-percent modification," was similar in shape, but had only about three-fourths of the area addition, which permitted less abrupt fuselage contours as compared with the full modification. A third modification incorporated the wing-root fillets indicated in figures 3 and 4 installed in combination with the full afterbody modification. The purpose of these fillets was to move the point of maximum area farther forward, thus increasing the afterbody fineness ratio. Photographs of the basic model and of the model with wing-root fillets and the full afterbody modification are given in figure 5.

Instrumentation

An electric strain-gage balance was mounted within the fuselage for force and moment measurement.

The model was equipped with flush pressure orifices at the locations indicated in figure 6. Four chordwise rows of 31 orifices each on the left and two rows of 11 orifices each on the right comprised the wing pressure instrumentation. The left semispan of the horizontal tail was instrumented with three chordwise rows of 16 orifices each. Seventy-seven pressure-measuring orifices at eleven stations having 4 to 9 peripheral orifices each were installed on the store, while one row of 9 orifices per side was employed on the pylon.

Base pressures were measured for all test conditions by two orifices located on the sting 0.35 inch inside the fuselage base.

TESTS

The investigation was conducted in the Langley 16-foot transonic tunnel which has an octagonal slotted test section permitting a continuous variation of speed to a Mach number slightly above 1.0.

For all test conditions six-component force and moment data were obtained. For most conditions extensive pressure data were also recorded.

The Mach numbers were 0.80, 0.90, 0.94, 0.98, 1.00 and 1.03 for all configurations. The angle-of-attack range was -2° to 15°, except that at the highest two Mach numbers the range was limited by the balance capacity. For the basic configuration and the store-on configuration tests were made at sideslip angles of $\pm 5^\circ$ as well as 0°. For one of the afterbody modifications tests also were made at a sideslip angle of $+5^\circ$.

The test Reynolds number (based on wing mean aerodynamic chord) was about 5.0×10^6.

ACCURACY AND CORRECTIONS

The measurement of Mach number in the test region is correct within ±0.002 (see ref. 3) and angles of attack and angles of sideslip presented are believed accurate to within ±0.1 degree.

The estimated accuracy of force and moment coefficients is as follows:

C_L	±0.01
C_D (at low lift coefficients)	±0.001
C_D (at high lift coefficients)	±0.003
C_m	±0.003
C_l	±0.001
C_n	±0.001
C_Y	±0.001
p_b	±0.01

A wind-stream upflow angle of 0.25 degree has been allowed for in the computation of the data.

Lift and drag data have been adjusted to the condition of free-stream static pressure at the model base. Base pressure coefficients are presented for the basic model at $i_t = 0^\circ$ (fig. 7(d)), the basic model at $i_t = -5^\circ$ (fig. 8(d)), the basic model with horizontal tail off (fig. 9(d)), and for the model with full afterbody modification (fig. 11(d)). No base pressure data are presented for the model with store and pylon, since these data were essentially the same as figure 7(d). Similarly, no base pressure data have been included for the full afterbody modification plus wing-root fillets or for the 75-percent modification, since these data are essentially the same as figure 11(d).

No corrections have been applied for sting interference or aeroelastic effects. Boundary interference effects for a wing-fuselage combination of this size are negligible in this test section up to and slightly above Mach number 1.0. (See ref. 4.)

RESULTS AND DISCUSSION

The basic force data obtained for all configurations are presented in figures 7 to 15 and for convenience are tabulated as follows:

Longitudinal data	Data presented	Figure
Basic model, $i_t = 0^\circ$	α against C_L	7(a)
	C_D against C_L	7(b)
	C_m against C_L	7(c)
	P_b against C_L	7(d)
Basic model, $i_t = -5^\circ$	α against C_L	8(a)
	C_D against C_L	8(b)
	C_m against C_L	8(c)
	P_b against C_L	8(d)
Basic model, horizontal tail off	α against C_L	9(a)
	C_D against C_L	9(b)
	C_m against C_L	9(c)
	P_b against C_L	9(d)
Model with store and pylon	α against C_L	10(a)
	C_D against C_L	10(b)
	C_m against C_L	10(c)

Longitudinal data	Data presented	Figure
Model with full afterbody modification	α against C_L	11(a)
	C_D against C_L	11(b)
	C_m against C_L	11(c)
	P_b against C_L	11(d)
Model with 75-percent afterbody modification	α against C_L	12(a)
	C_D against C_L	12(b)
	C_m against C_L	12(c)
Model with full afterbody modification and wing-root fillets	α against C_L	13(a)
	C_D against C_L	13(b)
	C_m against C_L	13(c)
Sideslip data	**Data presented**	**Figure**
Basic model	C_m against β	14
	C_l against β	15
	C_n against β	15
	C_Y against β	15
Model with full afterbody modification	C_m against β	14
	C_l against β	15
	C_n against β	15
	C_Y against β	15
Model with store and pylon	C_m against β	14
	C_l against β	15
	C_n against β	15
	C_Y against β	15

Store and Pylon Installation

Effect on wing loading.- The effects which installing the store and pylon had on wing pressures and loading are illustrated in figures 16 and 17. In general, the pressure coefficients were more negative on both the upper and lower surfaces, figure 16. The lower surface change is the greatest, however, especially inboard, so that the loads are also reduced as shown in figure 17.

Effect on airplane forces and moments.- The effects of the store and pylon installation on airplane forces and moments are presented in figures 18 through 23. The lift-curve slope, as shown in figure 18, was reduced by the store installation. The lift coefficient at zero angle of attack was also reduced slightly, as can be seen by comparing figures 7(a) and 10(a). This is at least partially caused by the reduction in loading on the right wing. The C_D increase at zero lift caused by the store installation, as shown in figure 19, varies from 25 to 50 percent, being 0.0025 at $M = 0.80$ and 0.016 at $M = 1.03$. Figure 20 shows the maximum lift-drag ratio and the lift coefficient at which it occurs. The loss in maximum lift-drag ratio caused by the store ranges from 2.0 at $M = 0.80$ down to 1.0 at higher speeds. At zero lift, no significant change in longitudinal stability parameter $\frac{\partial C_m}{\partial C_L}$ is shown by figure 21 for any point in the test Mach number region. The zero lift pitching-moment coefficient also is unchanged except at Mach numbers 0.98 and 1.00, as shown in figure 22. At these speeds the shock pattern may be strongly influenced by the presence of the store.

The store installation on the right wing resulted in a positive change in C_l of up to 0.01 at zero sideslip, figure 15. C_{l_β} is generally more negative (positive dihedral effect) with the store mounted, at least for the higher Mach numbers, as is shown in figure 23. C_n at zero sideslip is also generally shifted in the positive direction (fig. 15) and the directional stability parameter C_{n_β} is reduced as much as 20 percent (fig. 23). A 20-percent increase in C_{Y_β} is also shown in figure 23.

Store and pylon loads.- None of the actual pressures measured on the store have been included in the report, but the longitudinal distribution of load and the total integrated load, both in the normal and lateral directions, have been included, figures 24 to 26. Only 77 orifices were used to measure pressures on the store and this number is not considered to be sufficiently large to obtain a high degree of accuracy of the integrated loads. However, it is believed that the results are good qualitatively, and that the proper trends are shown.

In general, the normal load distribution on the store does not vary greatly with any of the test variables, figure 24. The forward 25 or 30 percent of the store supports a negative load due to the negative store incidence of $5\frac{1}{2}^\circ$ relative to the wing. This negative load is maintained through most of the angle-of-attack range due to the controlling effect of the wing on the flow in this region. The load on the store nose at the highest test angle of attack becomes slightly positive. The section of the store between 30 and 60 percent maintains a loading that is positive due to low pressures between the store and the wing in this region. Behind the 60 percent station the load is again negative.

The distribution of side load on the store is characterized by a load on the forward 50 percent, shown in figure 24(b), which varies considerably with angle of sideslip β generally being positive when β is -5° and negative when β is $+5^\circ$. From this point aft the load is less influenced by the test conditions. The load on the central area is always in an inboard direction due to the lowered pressure on the inboard side of the store. Both normal and side load section data have in general the same shape and characteristics as do the section normal and side load distributions of reference 2.

Integrated loads on the store are given in figure 25 as a function of angle of attack. At zero angle of sideslip the store side force is negative or inboard. The fact that only a small change in store side force occurs with angle of attack is in agreement with the supersonic data of reference 5 for a similar inboard store location. Large variations of the store side-force and yawing-moment coefficients occur with sideslip and are shown in figure 26, cross plotted from figure 25.

A sampling of the pressure distributions obtained at the one pylon station is included as figure 27. The integrated section load coefficients for the pylon at all test conditions are shown in figure 28. The loads on the pylon are seen to vary appreciably with both angle of attack and sideslip angle. For the right wing mounting employed, the side force becomes more positive (that is, toward the tip) with positive angles of attack and negative angles of sideslip. The increase in the load with angle of attack is associated with the usual outflow on the lower surface of a swept wing.

Horizontal-Tail Characteristics

Horizontal-tail loads were obtained by the integration of pressures measured on the upper and lower surfaces at the three stations on the left semispan. The span load distributions are shown in figure 29. For the sideslip case the left semispan data shown are those obtained on the left semispan at $\beta = +5^\circ$. The data shown on the right semispan were actually obtained by left semispan measurements at $\beta = -5^\circ$. For the unyawed case the left semispan data are plotted on both the left and right sides.

Tail normal force.- The tail normal-force coefficients for incidence angles of 0° and -5° are presented in figure 30. These data were obtained by the spanwise integration of section load data. There was some concern over the accuracy of the resulting tail normal-load values, since there were only three pressure orifice stations. Therefore, figure 30 also includes (at $i_t = 0^\circ$ only) tail load data obtained from the tail contribution to pitching moment. The results indicate very good agreement at all Mach numbers. It is believed, therefore, that accurate data have been obtained using only three semispan stations on the horizontal tail.

The reduction in tail normal force at the higher angles of attack may be attributed to the rate of change of downwash for a swept wing such as is shown, for example, in reference 6.

The slope of the tail lift with tail incidence as determined from the present data for low angles of attack varied from 0.055 to 0.068, having the higher values at the highest Mach numbers.

A comparison of the tail loads at zero sideslip and 5° sideslip is shown in figure 31. For all tested conditions the tail load was more positive at sideslip angles, or in a direction to cause a more negative pitching moment; the magnitude was of about the proper order to produce the pitching-moment coefficient reductions with sideslip shown in figure 14.

Asymmetric bending moment.- For the sideslip condition, as shown in figure 29, appreciable differences in loads between opposite semispans may be encountered. For a horizontal tail mounted on a vertical-tail surface, as it was on this model, bending-moment differences at the attachment may become critical. The load distributions were, therefore, integrated for differences in bending-moment coefficients and the results are presented in figure 32. For the lower Mach numbers at the highest test angle of attack the asymmetric bending moment becomes very large. This increase is apparently due to the wing vortex moving to a position inboard of the horizontal-tail tip. To show this, comparisons of the horizontal-tail span loading have been made with unpublished downwash data measured behind a wing-body model having 45° sweep of the quarter chord, aspect ratio 4, taper ratio 0.6, and having 6-percent-thick sections parallel to the stream. This wing is related closely enough to the wing of the present tests so that flow field characteristics would be similar. The downwash data were measured with pitch head probes at four points behind and above the wing corresponding to four locations on the tail semispan. These data are shown in figure 33 for Mach numbers 0.80 and 0.98 and for angles of attack of 11° and 15°. The downwash data are presented as the local angle of attack of the tail, α_t. As shown in figure 33(a) at $M = 0.80$ the general variation of local angle of attack across the span, as measured with probes, is similar to that of the tail load distribution shown immediately below in the same figure. Note that at the tip the local angle of attack and the load at $\alpha = 11°$ are both negative, indicating large downwash, while at $\alpha = 15°$ the tip angle and load are both positive, indicating greatly reduced downwash. The former condition indicates a wing vortex position outside the tail tip, while the latter indicates that at $\alpha = 15°$ the wing vortex has moved inside the tail tip. At the bottom of the page (figure 33(a)) are shown the span loads obtained for the same angles of attack at $\beta = 5°$. It can be seen that at 11° some asymmetry in load has developed due, apparently, to the right tip moving into the low downwash region

outside the wing vortex. At $\alpha = 15^\circ$, however, the asymmetry in load is very large because not only is a large part of the right tip outside the wing vortex in the low downwash region, but the left tip has become completely unloaded due to having moved inside the vortex. These results are typical of Mach numbers 0.80, 0.90, and 0.94. Figure 33(b) indicates that for $M = 0.98$ at $\alpha = 15^\circ$ the wing vortex is still outside the tail tip (for $\beta = 0^\circ$) and thus at this speed a sideslip angle of 5° does not produce the large asymmetry of loading obtained at lower speeds. Downwash measurements at higher angles, however, indicate that at $\alpha = 17^\circ$, the vortex would be inside the wing tip and the loading would become similar to that at $\alpha = 15^\circ$ at lower speeds.

Tail hinge moments.- Hinge-moment coefficients about the hinge axis indicated in figure 1 have been determined from the pressure data obtained at the three orifice stations on the horizontal tail and are presented in figure 34. Comparing these data with the tail normal-force data in figure 30, it will be noticed that the hinge moments are quite large for some conditions where the normal load is small, and vice versa. This results, of course, from the influence of the downwash field on the span loading on the tail.

The slope of the hinge-moment coefficient with tail incidence angle has been determined from figure 34 and is shown in figure 35. The rapid increase with Mach number is due to the spanwise and rearward center-of-pressure shift generally associated with transonic speeds.

Tail incidence for trim was calculated from the pitching-moment data (of figs. 7(c) and 8(c)) and is shown on the left side of figure 36. Using these trim tail incidences and the tail hinge-moment data, C_h for trim has been determined and is plotted against angle of attack on the right side of figure 36. The average slope of $C_{h(\text{trim})}$ between $\alpha = 0^\circ$ and 4° through the Mach number range is presented in figure 37 as $\partial C_{h(\text{trim})}/\partial\alpha$. The increase of this parameter with Mach number, which represents a stiffening of the tail control characteristics, is very severe, and would be reflected in a correspondingly increased tail actuator force. The actuator force change, for example, which would be required to make an angle-of-attack change of 1° at $M = 1.03$ is more than 40 times as great (allowing for change in q) as at $M = 0.80$. The large value of $\partial C_{h(\text{trim})}/\partial\alpha$ at high Mach numbers could be reduced by a more rearward position of the hinge line, but this would result in an overbalanced tail at lower speeds.

Effects of "Area-Rule" Modifications

The modifications tried, which were discussed earlier in the Model and Instrumentation Section, all involved the addition of fuselage volume

without indentation. The drag results from the basic model data of figure 7(b) and from the modified model data of figures 11(b), 12(b), and 13(b) have been cross plotted at two lift coefficients against Mach number in figure 38. At zero lift coefficient all modifications reduce the drag at Mach numbers greater than 0.92 but all increase the drag for lower Mach numbers. A maximum reduction of 0.01 in drag coefficient is realized at 0.96 Mach number at zero lift coefficient with the full afterbody modification and wing root fillets. Drag reductions become less at the highest test Mach numbers and at increased lift coefficients. Of the three modifications tried the full modification without fillets appears to have generally the best characteristics. Maximum L/D values for the full afterbody modification without root fillets are shown in figure 20, and, as would be expected, indicate some improvements at the higher speeds but some losses at the lower speeds.

The effect of the full afterbody modification without root fillets on the longitudinal stability parameter $\partial C_m/\partial C_L$, as shown in figure 21, is a small decrease in absolute value through the Mach number range. The pitching moment at zero lift, figure 22, is more positive with the modified afterbody, which is probably due to the downflow on the horizontal tail caused by the modification. The nose-down pitching-moment change with sideslip is usually less for the model with afterbody modification, figure 14.

The effective dihedral, C_{l_β}, shown in figure 23, becomes more positive at the higher speeds and angles of attack for the configuration with full afterbody modification, perhaps due to a change of the wing shock pattern. The directional stability derivative C_{n_β} generally decreases as much as 10 percent at the lower Mach numbers but no consistent change prevails at the higher speeds, figure 23. It might be expected that at high angles of attack the full afterbody modification would adversely affect C_{n_β} through a blanketing effect on the vertical tail, but this did not occur in the test angle-of-attack range.

CONCLUSIONS

The results of a transonic wind-tunnel investigation - which included the measurement of loads on a store mounted on a swept-wing fighter configuration, horizontal-tail loads at sideslip angles of 0° and 5°, and fuselage modifications to improve the cross-sectional-area progression of the model - lead to the following conclusions:

1. A 25- to 50-percent increase in the minimum drag occurred throughout the Mach number range with the store installed.

2. The directional stability was reduced as much as 20 percent when the store was installed.

3. There were large changes in the store side force with sideslip angle, but only small changes with angle of attack for the inboard location used in these tests. The side force on the pylon, however, varied considerably with angle of attack as well as with angle of sideslip.

4. Because of the influence of the downwash field, the distribution of load on the horizontal tail was such that relatively large hinge moments could exist for small total tail loads. The slope of the tail hinge-moment coefficient at trim with angle of attack increased throughout the test Mach number range, the rate of increase being greatest above a Mach number of 0.94.

5. At the lower Mach numbers and higher test angles of attack, the horizontal-tail asymmetric bending moments became severe in the sideslip condition.

6. Reductions up to 0.01 in minimum drag coefficient were obtained in the transonic range by afterbody enlargement, but all modifications increased drag below a Mach number of 0.92.

Langley Aeronautical Laboratory,
National Advisory Committee for Aeronautics,
Langley Field, Va., January 16, 1956.

REFERENCES

1. Guy, Lawrence, D., and Hadaway, William M.: Aerodynamic Loads on an External Store Adjacent to a 45° Sweptback Wing at Mach Number From 0.70 to 1.96, Including an Evaluation of Techniques Used. NACA RM L55H12, 1955.

2. Hamer, Harold A., and O'Bryan, Thomas C.: Flight Measurements of the Loads and Moments on an External Store Mounted Under the Wing of a Swept-Wing Fighter-Type Airplane During Yawing and Rolling Maneuvers. NACA RM L55G22, 1955.

3. Ward, Vernon G., Whitcomb, Charles F., and Pearson, Merwin D.: Air-Flow and Power Characteristics of the Langley 16-Foot Transonic Tunnel With Slotted Test Section. NACA RM L52E01, 1952.

4. Whitcomb, Charles F., and Osborne, Robert S.: An Experimental Investigation of Boundary Interference on Force and Moment Characteristics of Lifting Models in the Langley 16- and 8-Foot Transonic Tunnels. NACA RM L52L29, 1953.

5. Smith, Norman F., and Carlson, Harry W.: The Origin and Distribution of Supersonic Store Interference From Measurement of Individual Forces on Several Wing-Fuselage-Store Configurations. II - Swept-Wing Heavy-Bomber Configuration With Large Store (Nacelle). Lateral Forces and Pitching-Moments; Mach Number 1.61. NACA RM L55E26a, 1955.

6. Bandettini, Angelo, and Selan, Ralph: The Effects of Horizontal-Tail Height and a Partial-Span Leading-Edge Extension on the Static Longitudinal Stability of a Wing-Fuselage-Tail Combination Having a Sweptback Wing. NACA RM A53J07, 1954.

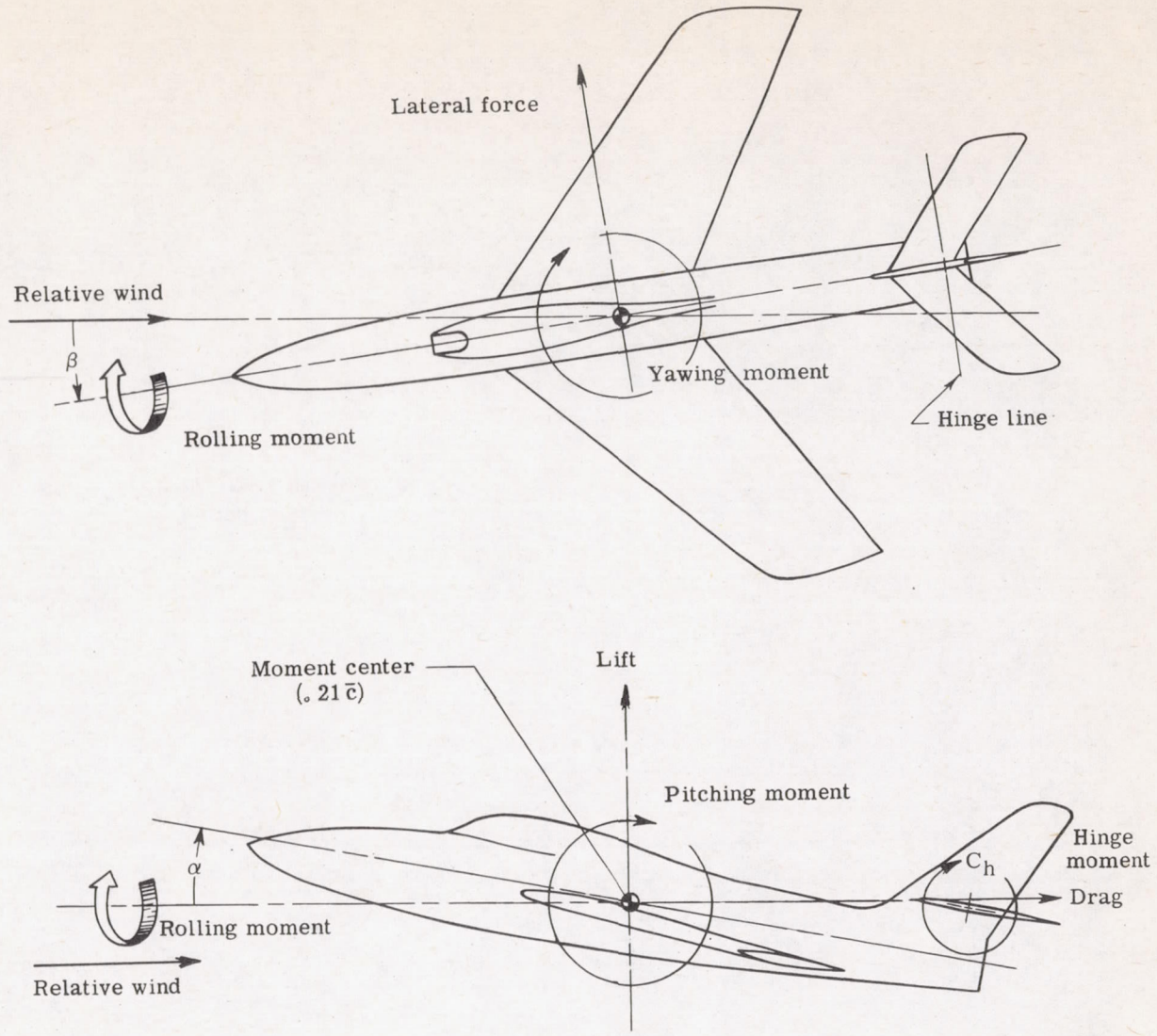


Figure 1.- Stability system of axes. Positive direction of forces, moments, and angles are indicated by arrows.

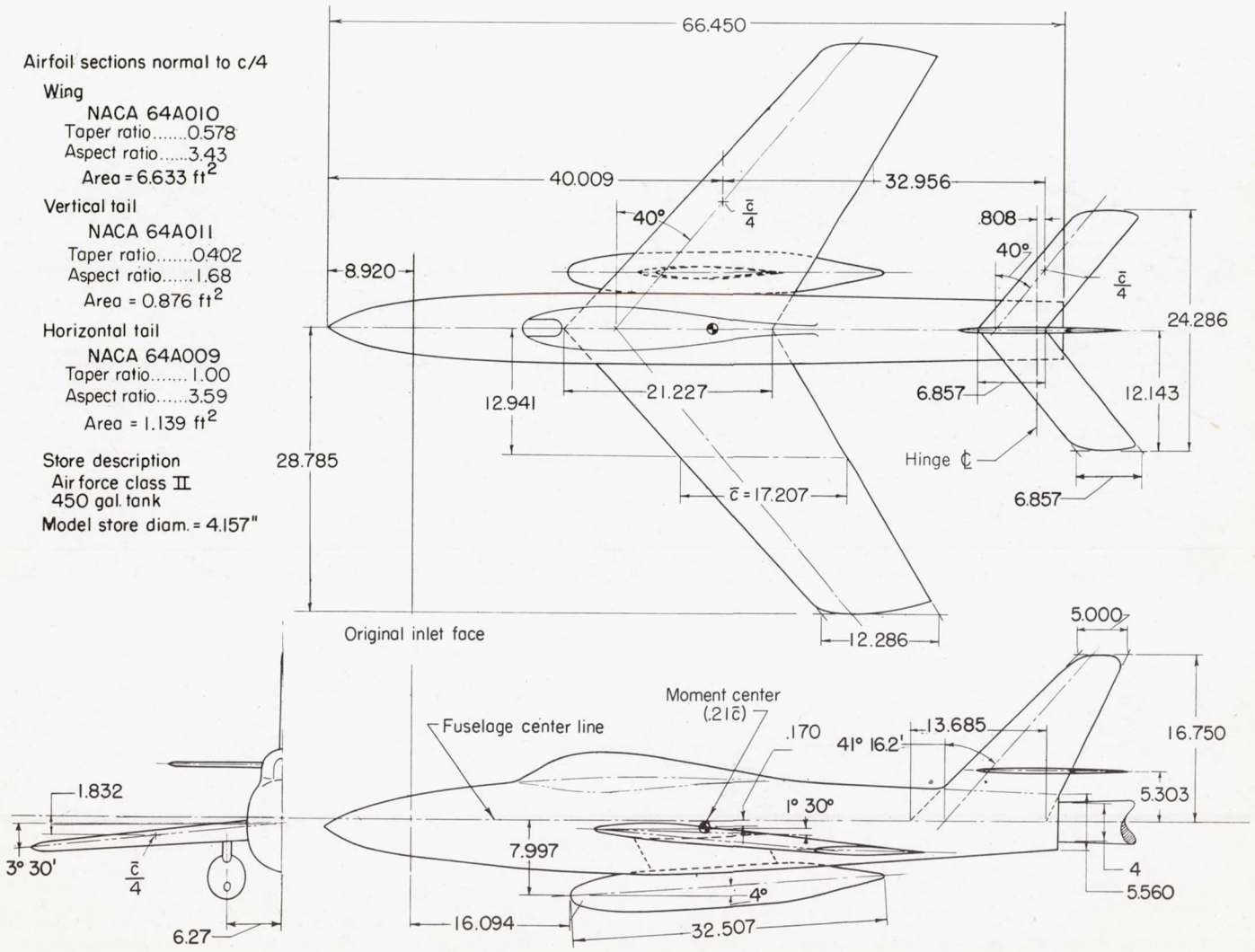


Figure 2.- Pertinent model dimensions. All dimensions are in inches except as indicated.

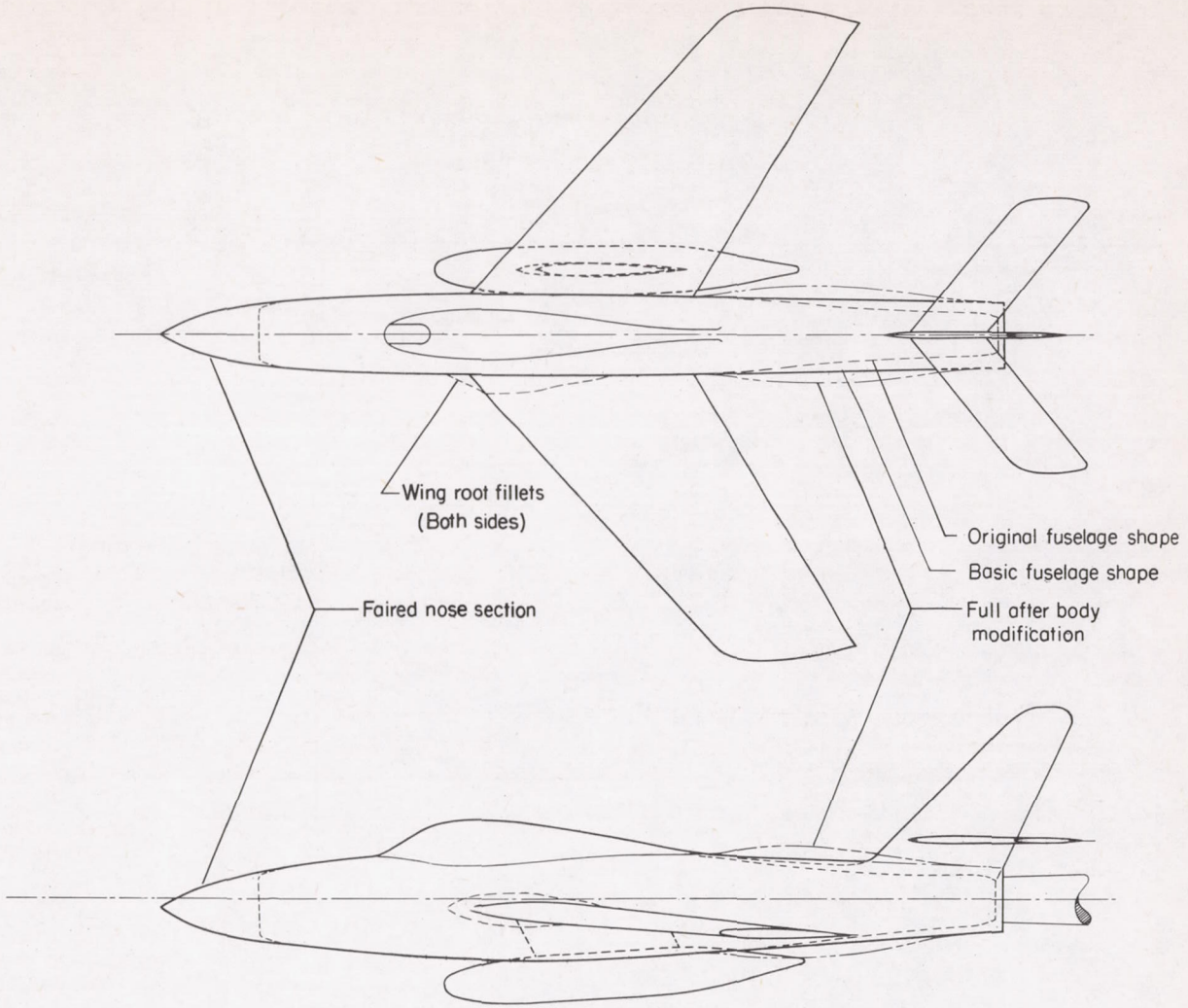


Figure 3.- Model fuselage modifications.

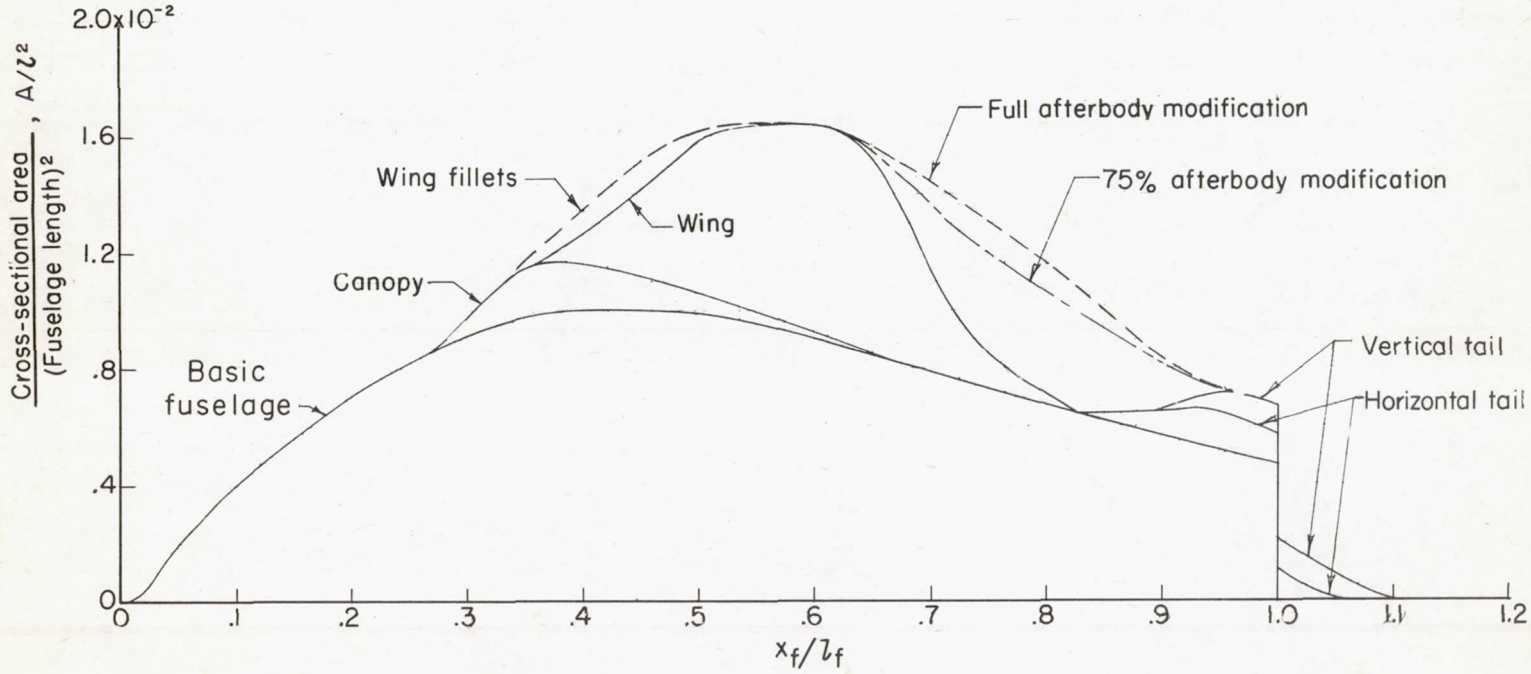
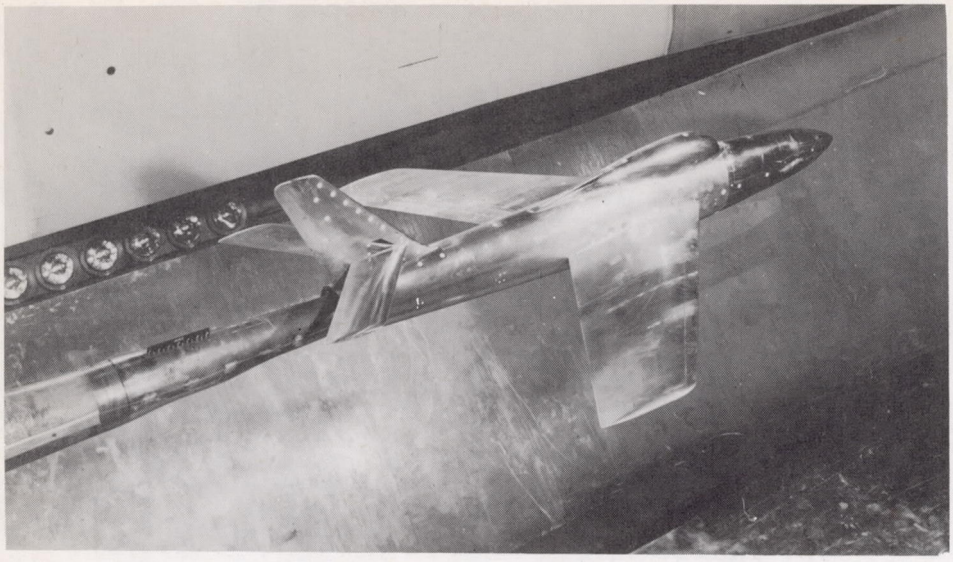
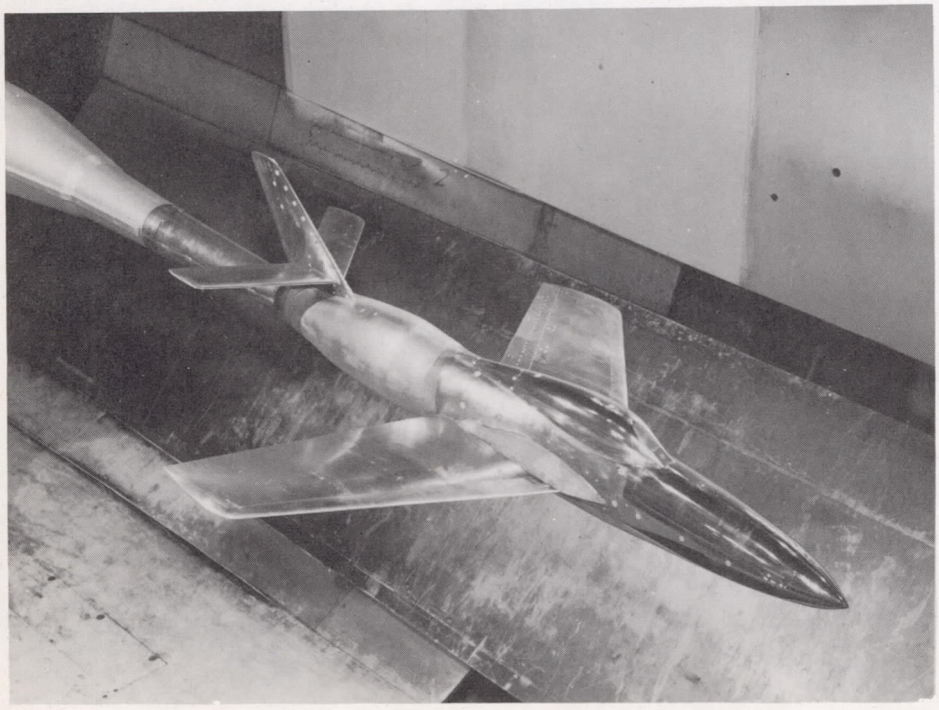


Figure 4.- Cross-sectional-area progression.



L-85146

(a) Basic model.



L-85236

(b) Model with full afterbody modification and wing-root fillets.

Figure 5.- Photographs of the model mounted in the test section.

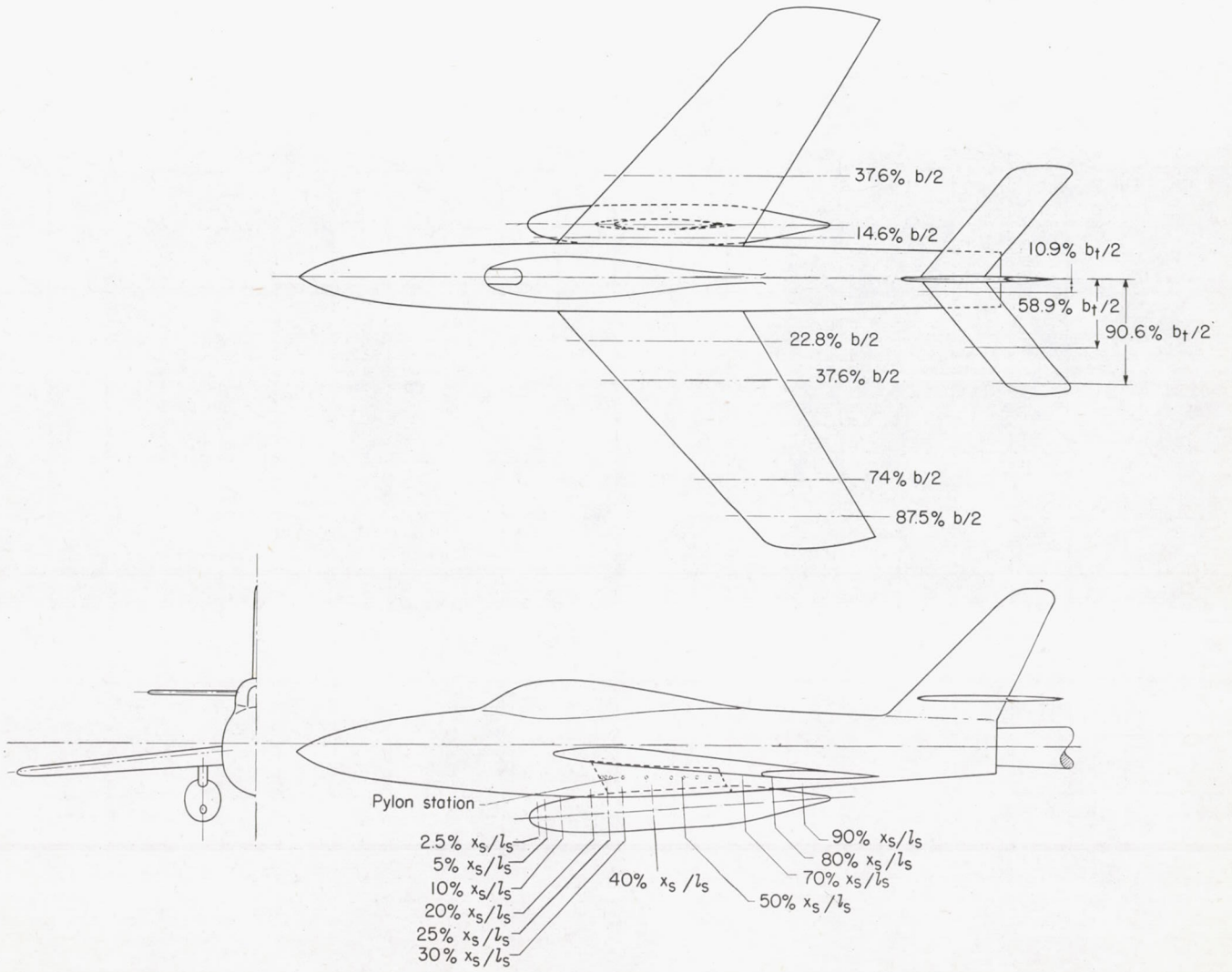
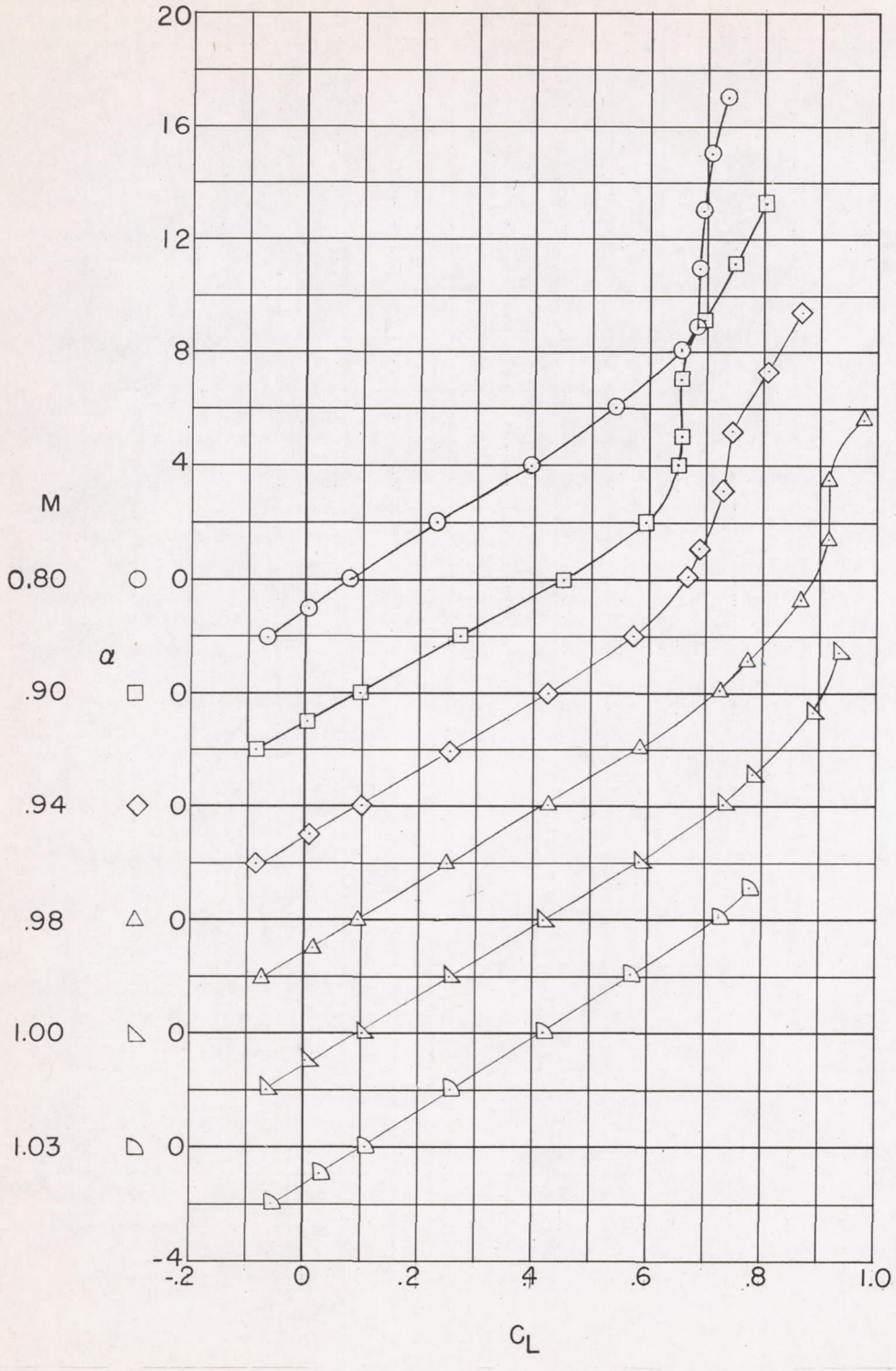
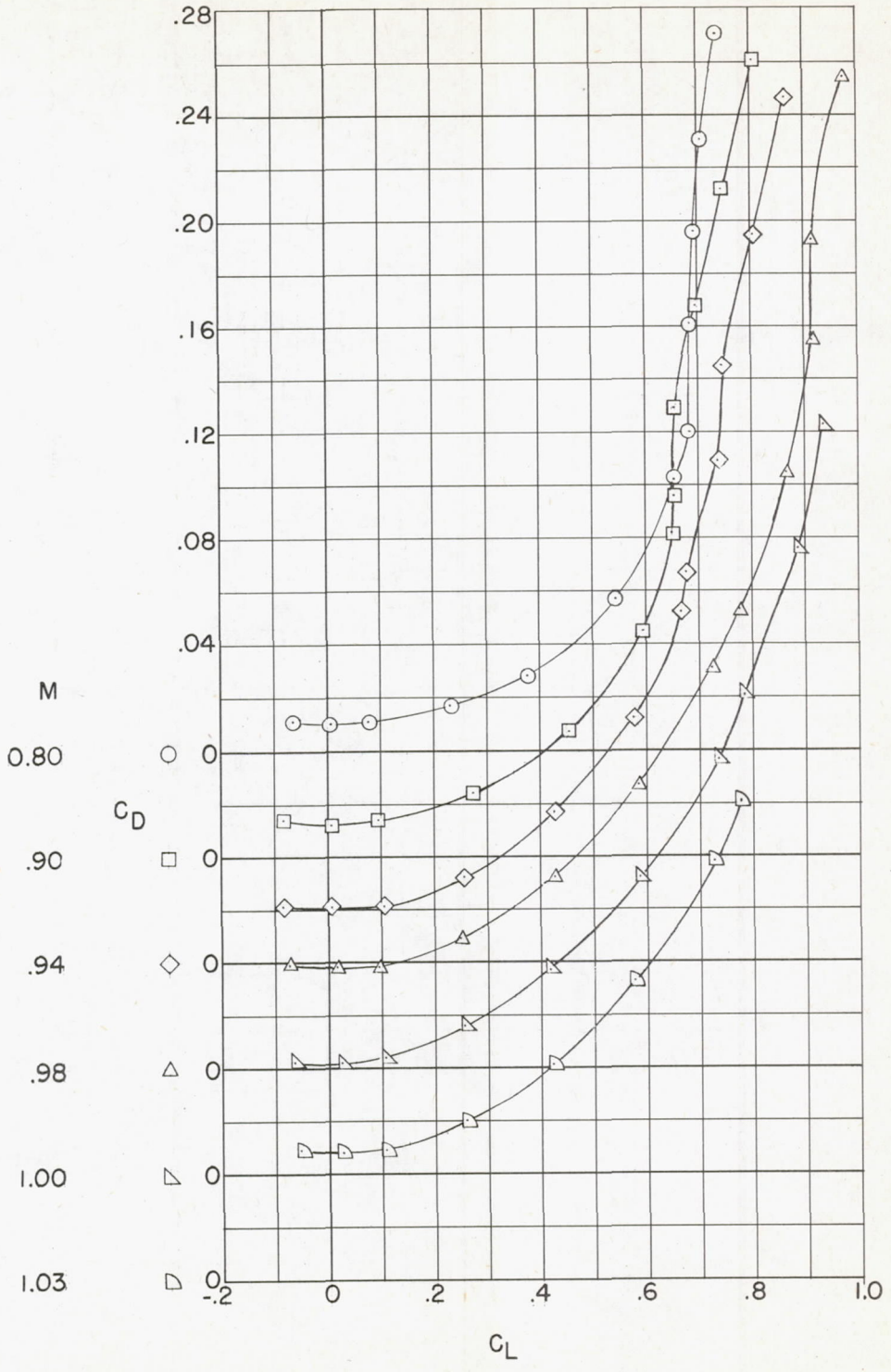


Figure 6.- Orifice station locations.



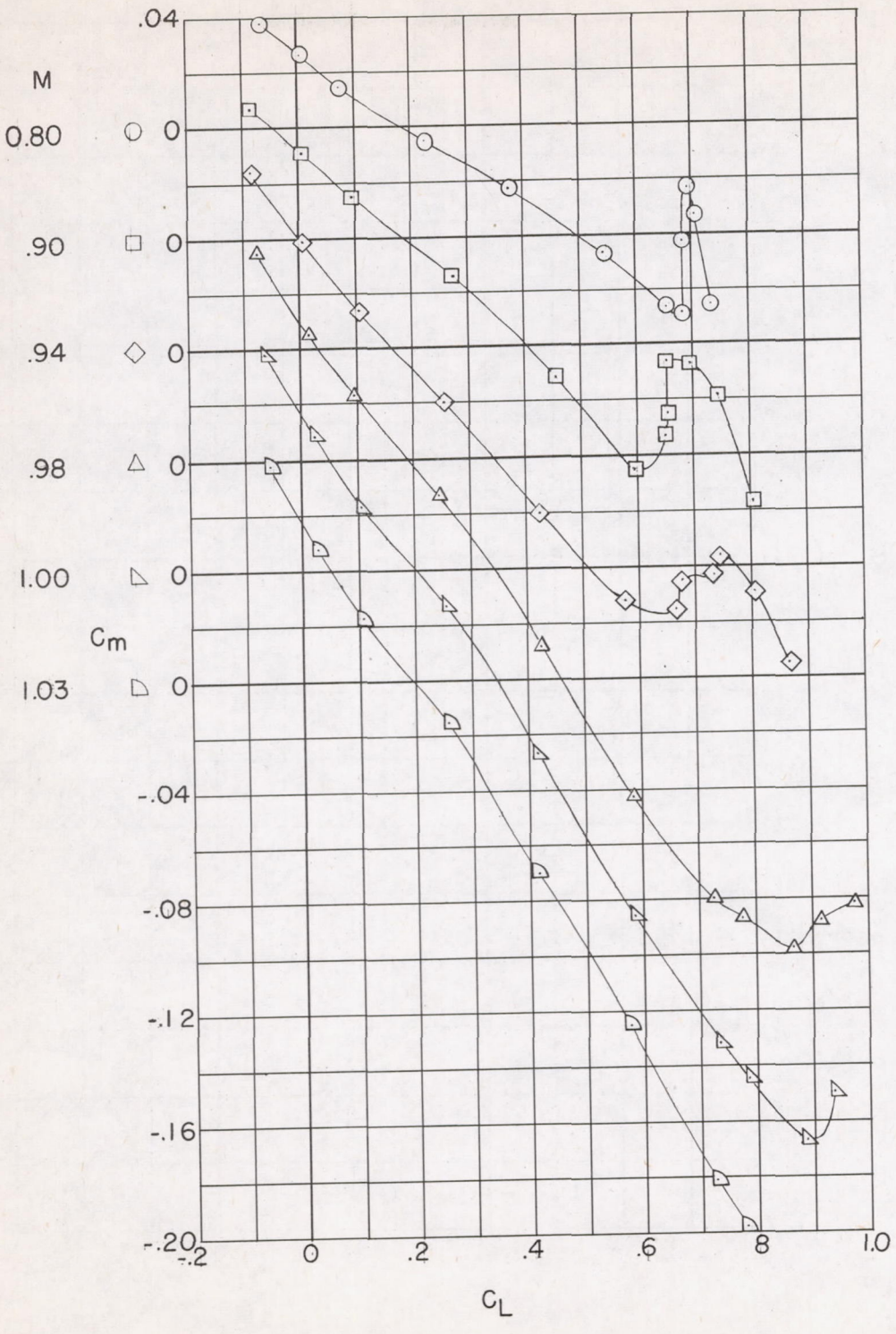
(a) Angle of attack.

Figure 7.- Longitudinal characteristics of the complete basic model. $i_t = 0^\circ$.



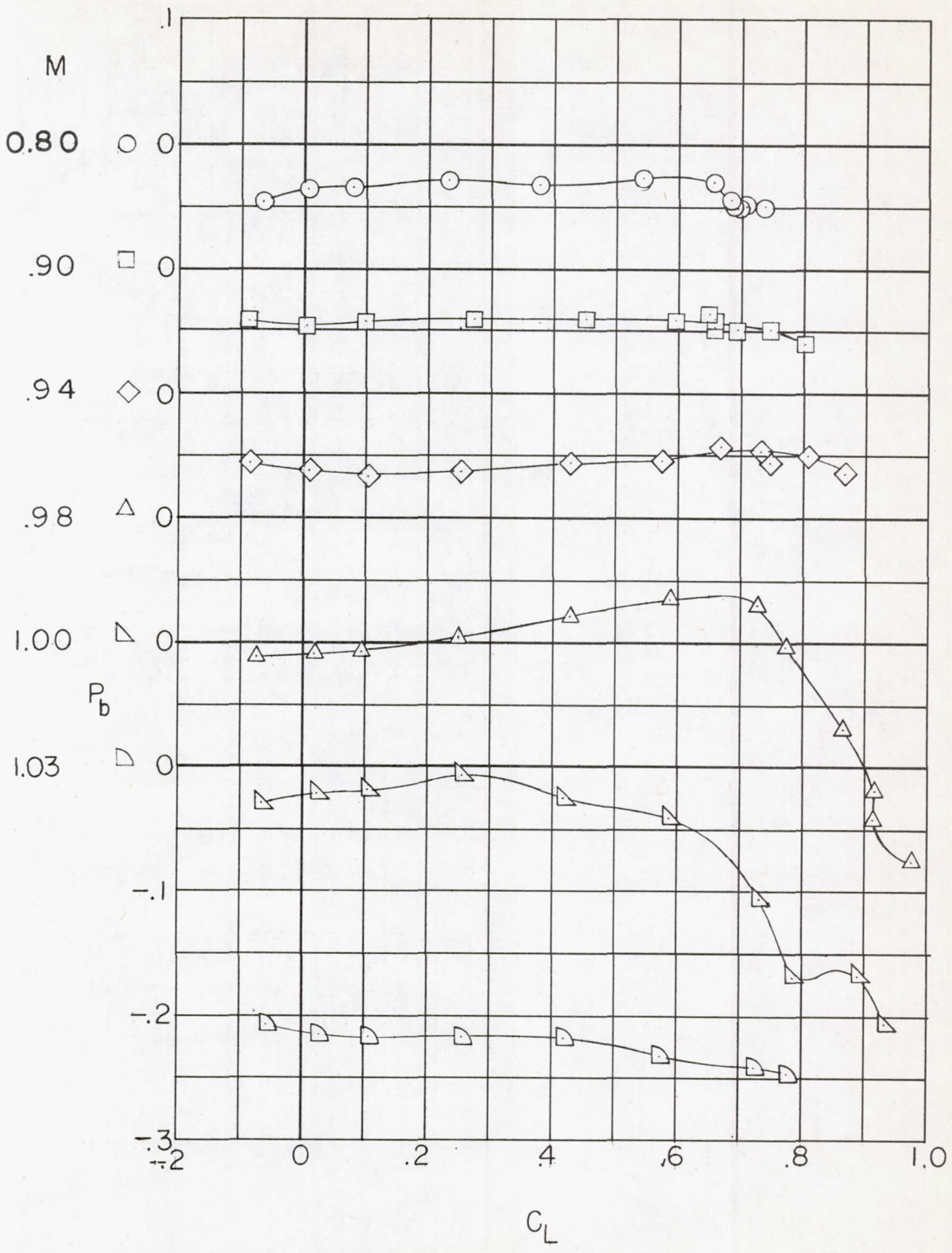
(b) Drag coefficient.

Figure 7.- Continued.



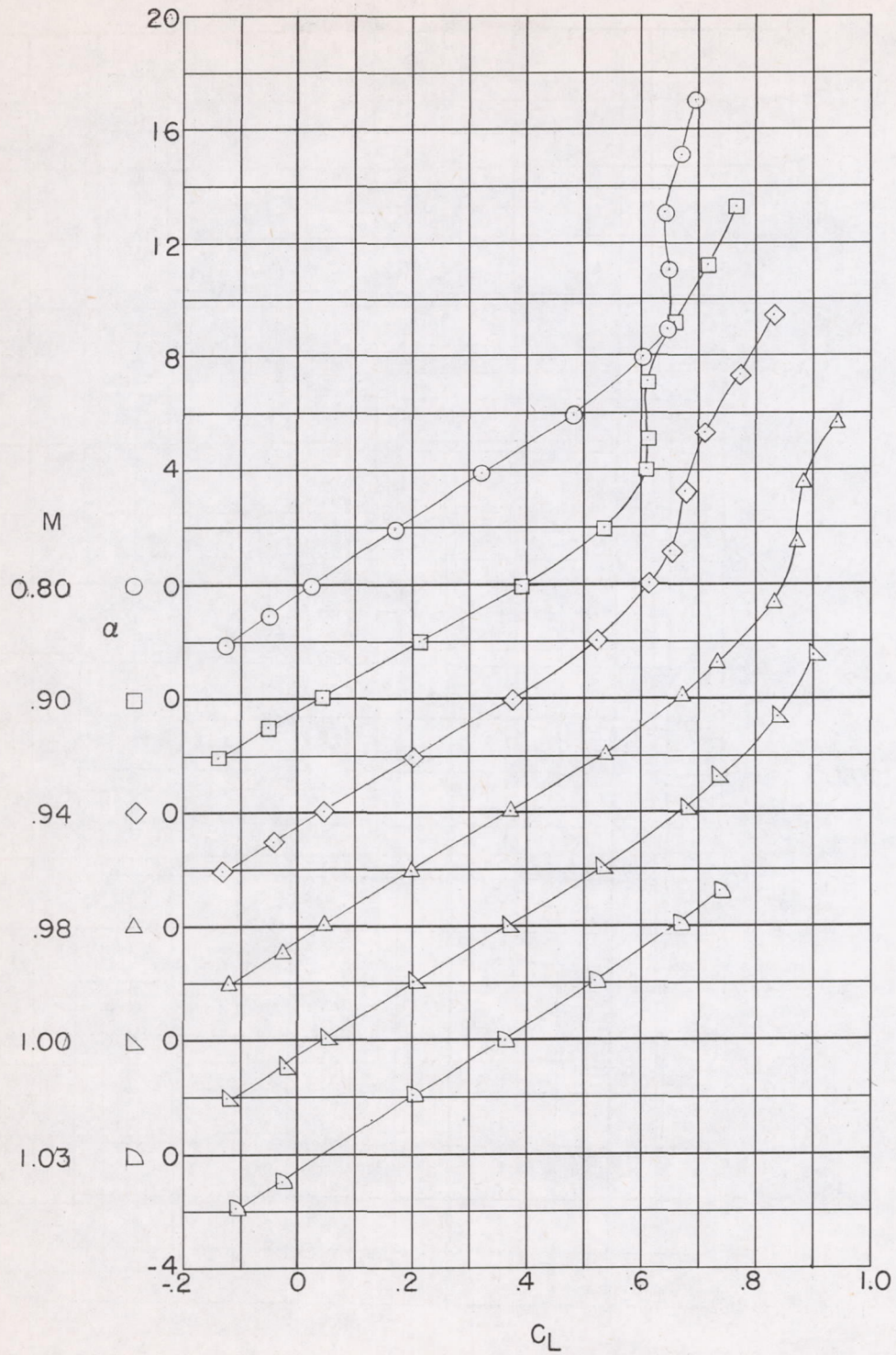
(c) Pitching-moment coefficient.

Figure 7.- Continued.



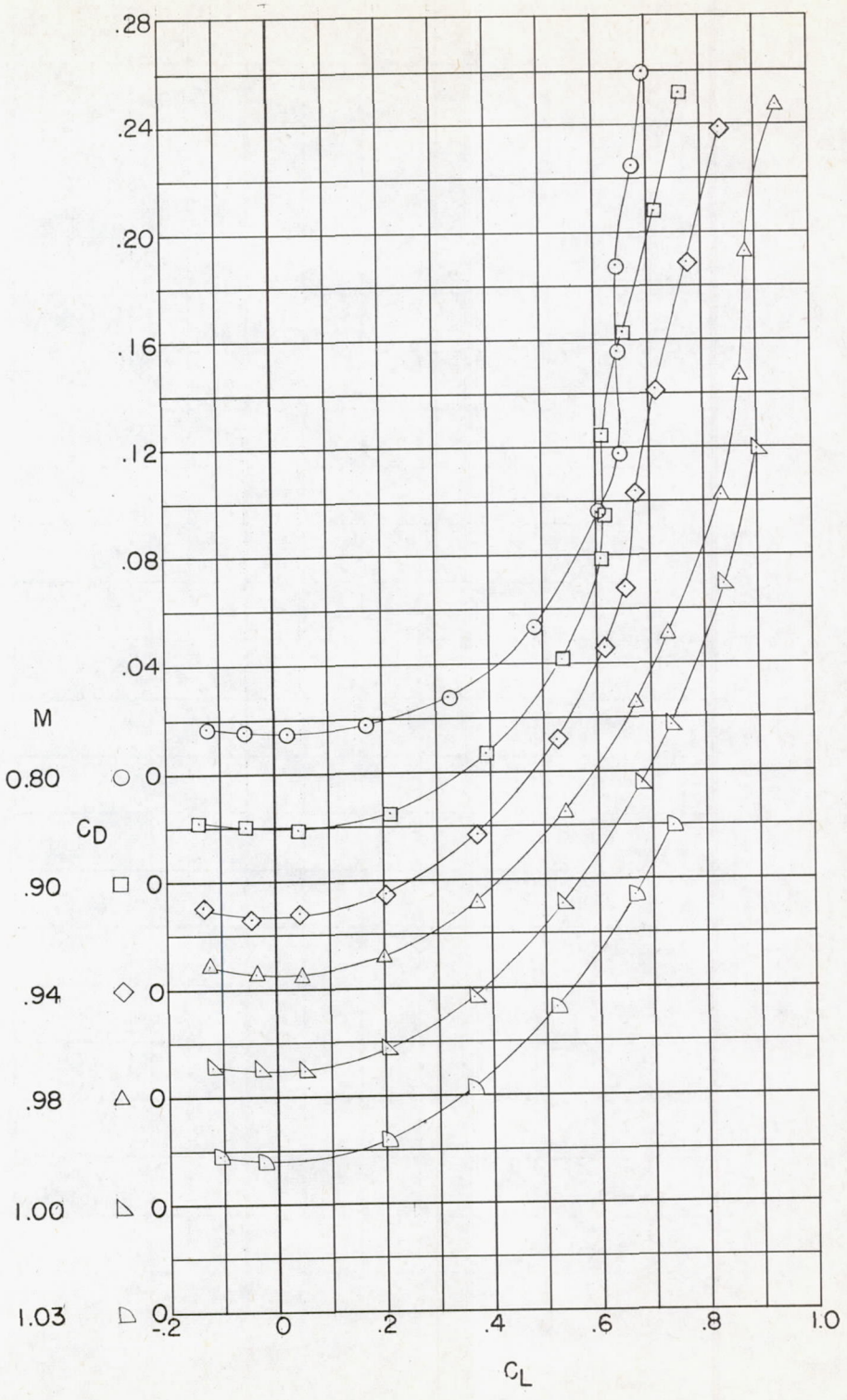
(d) Base pressure coefficient.

Figure 7.- Concluded.



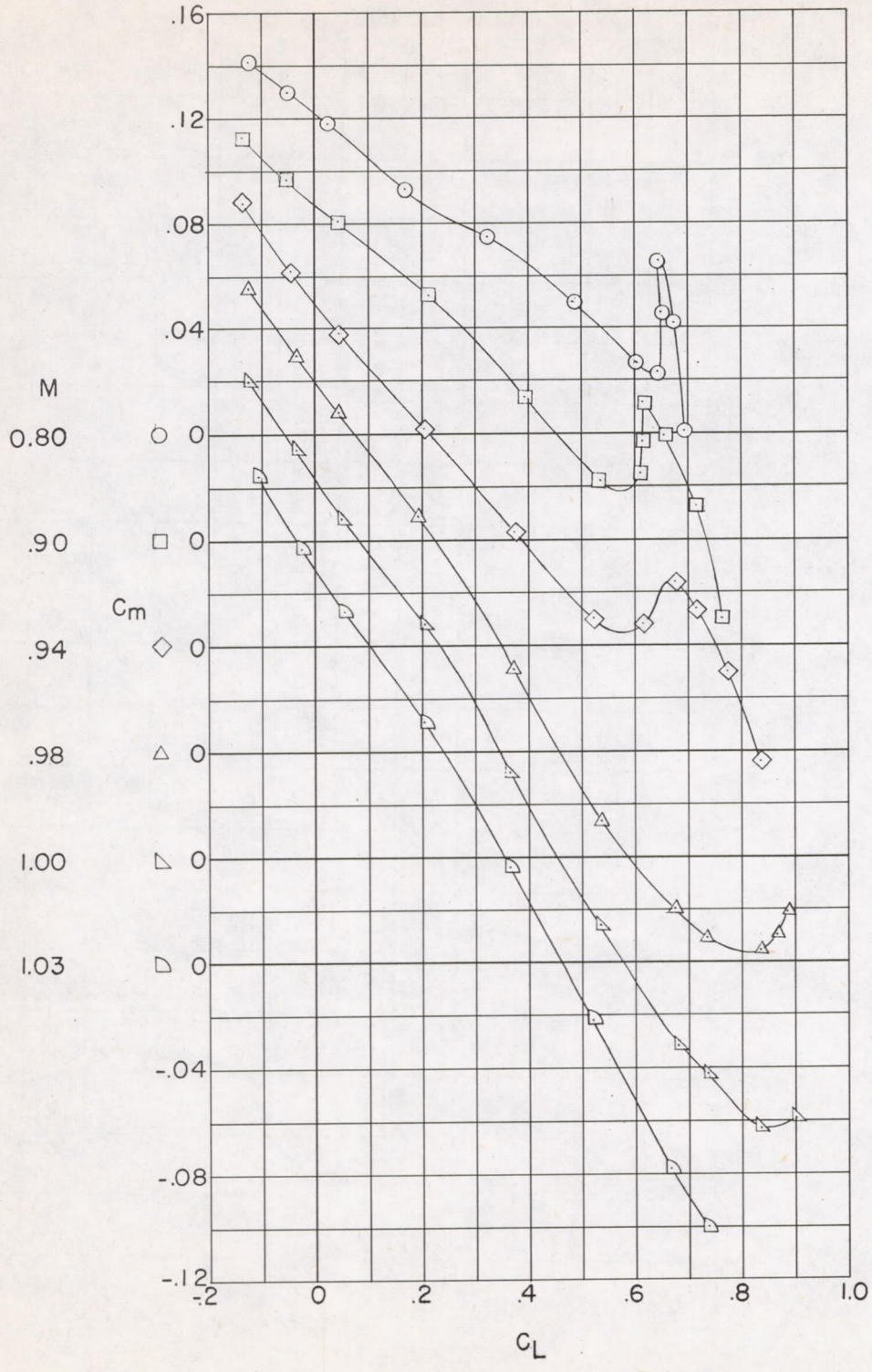
(a) Angle of attack.

Figure 8.- Longitudinal characteristics of the complete basic model. $i_t = -5^\circ$.



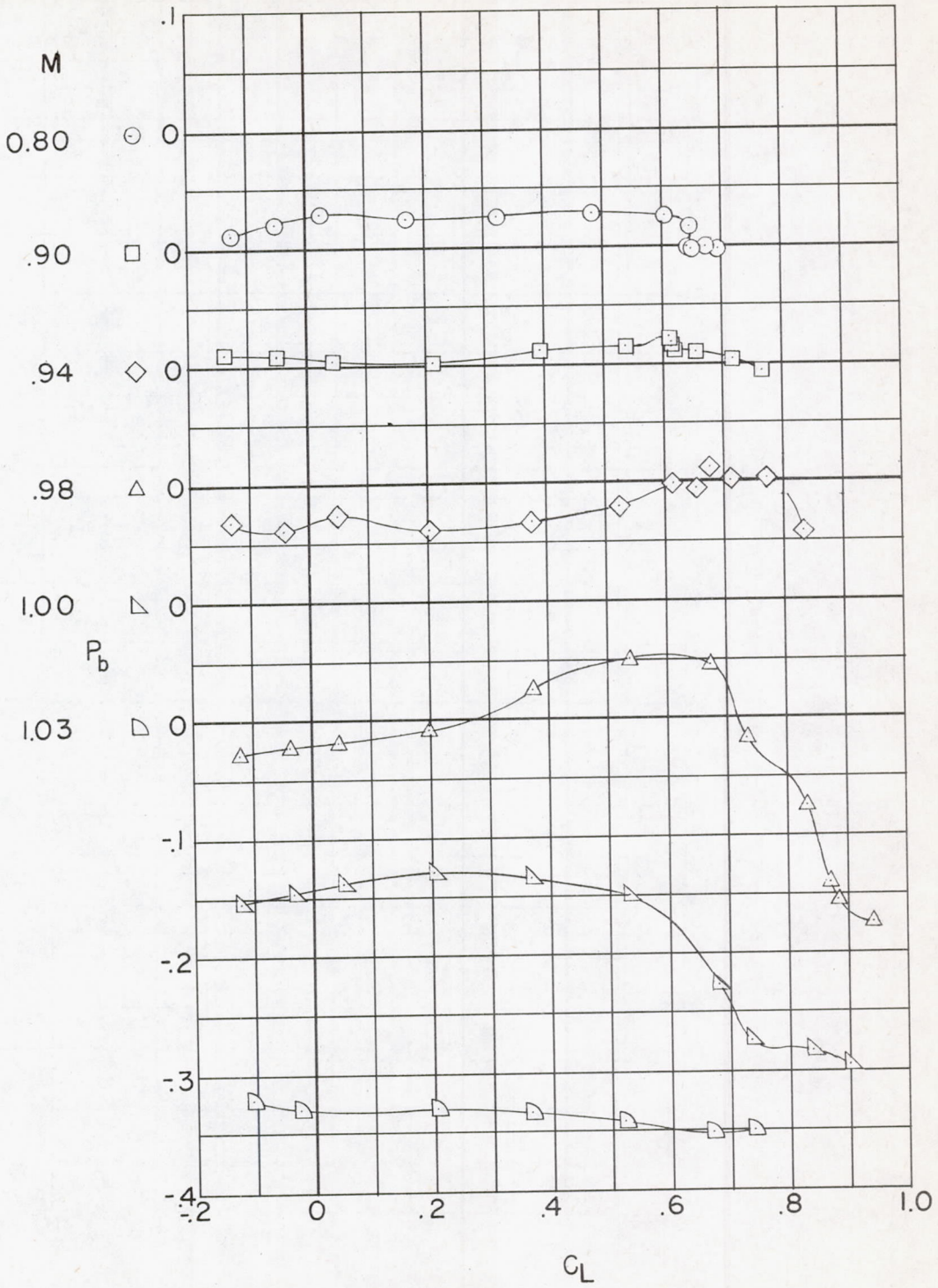
(b) Drag coefficient.

Figure 8.- Continued.



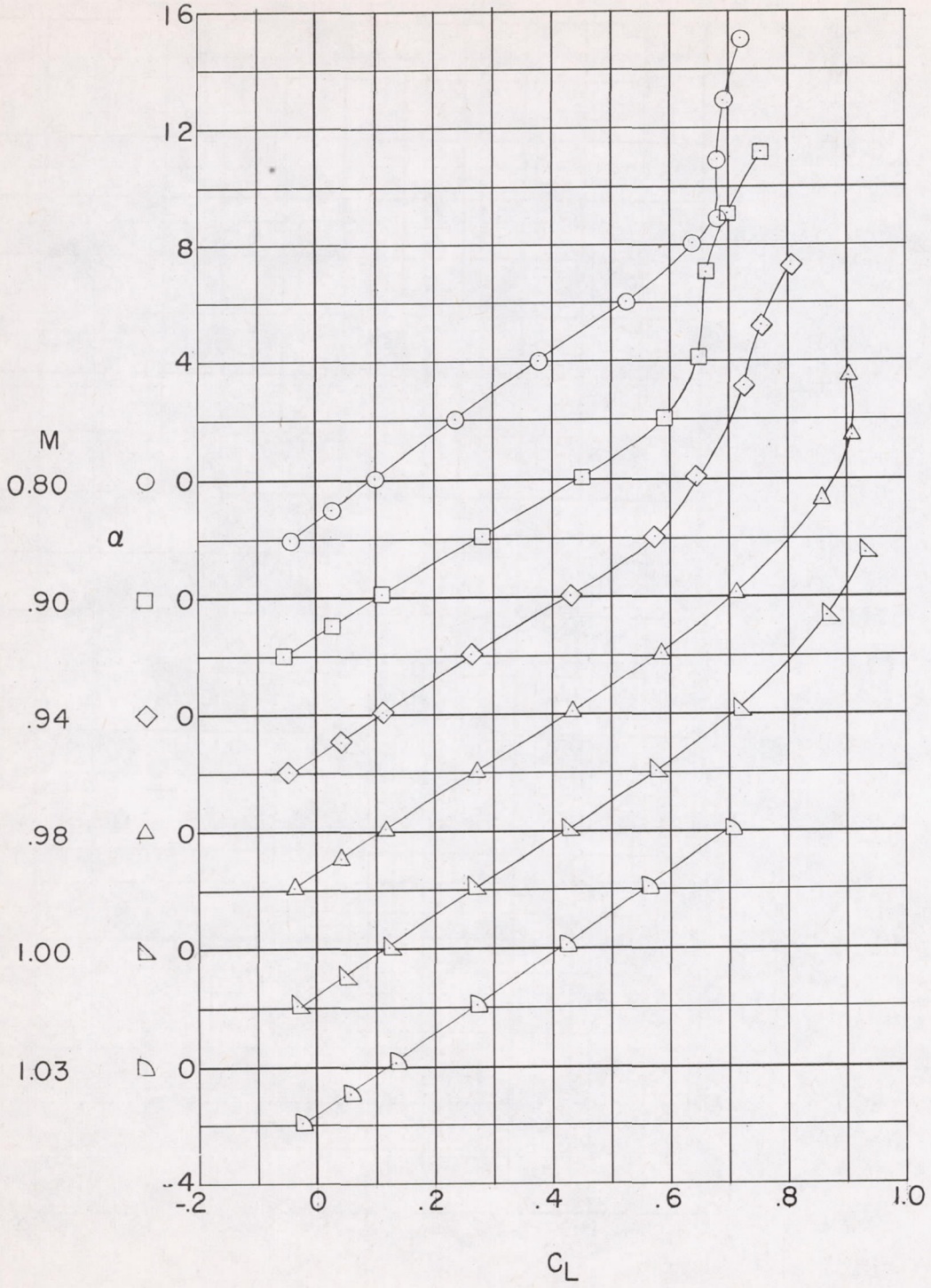
(c) Pitching-moment coefficient.

Figure 8.- Continued.



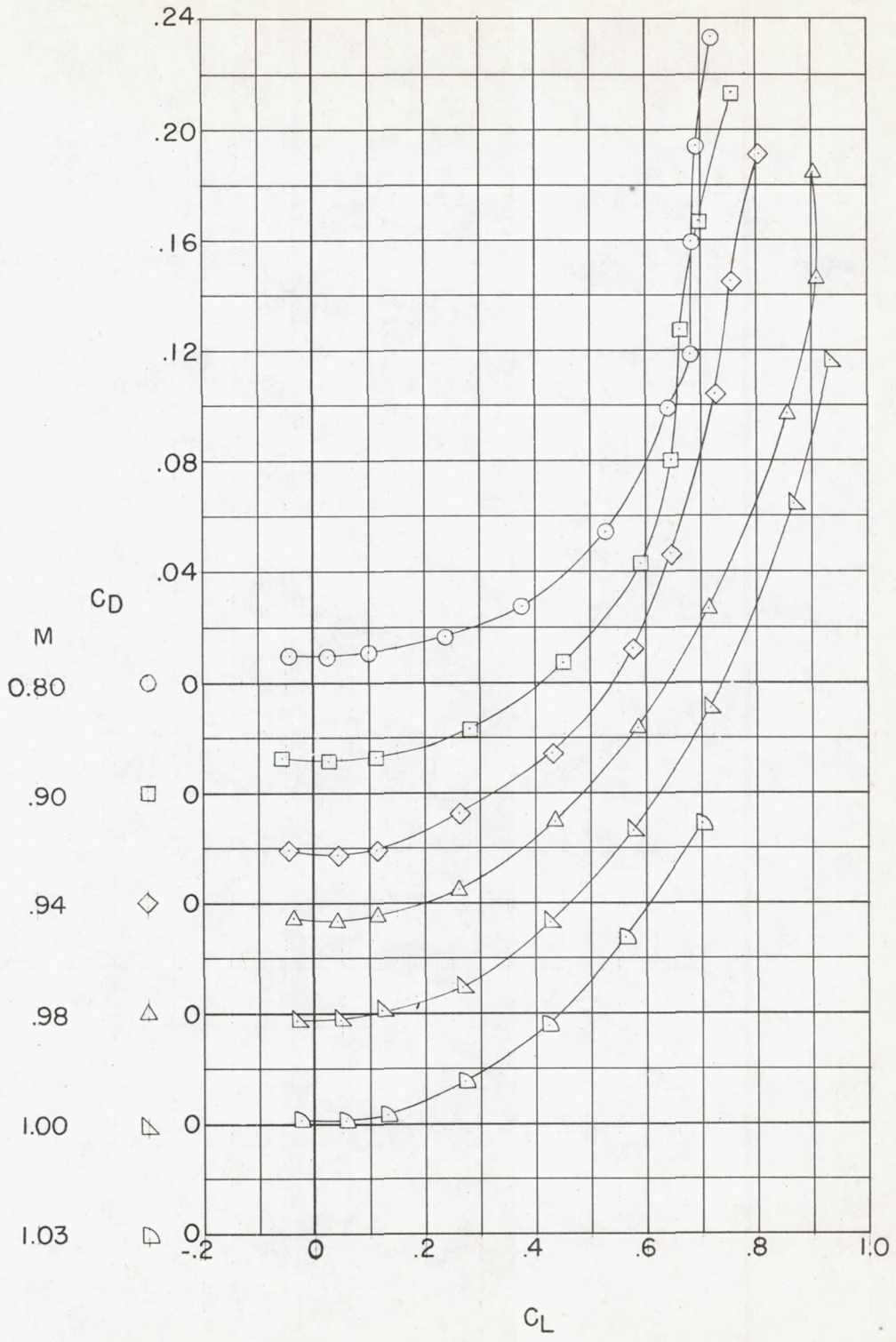
(d) Base pressure coefficient.

Figure 8.- Concluded.



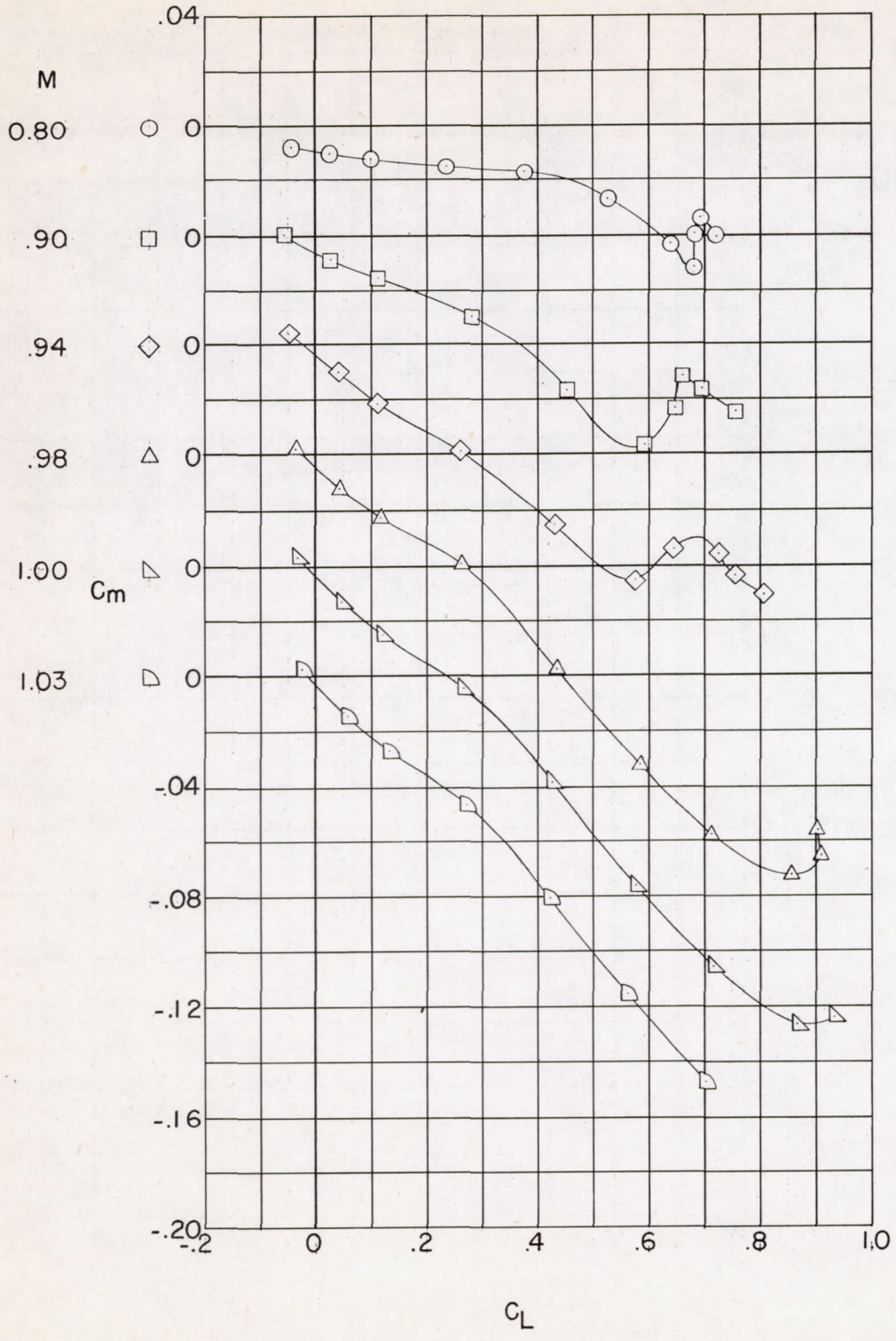
(a) Angle of attack.

Figure 9.- Longitudinal characteristics of the basic model. Horizontal tail off.



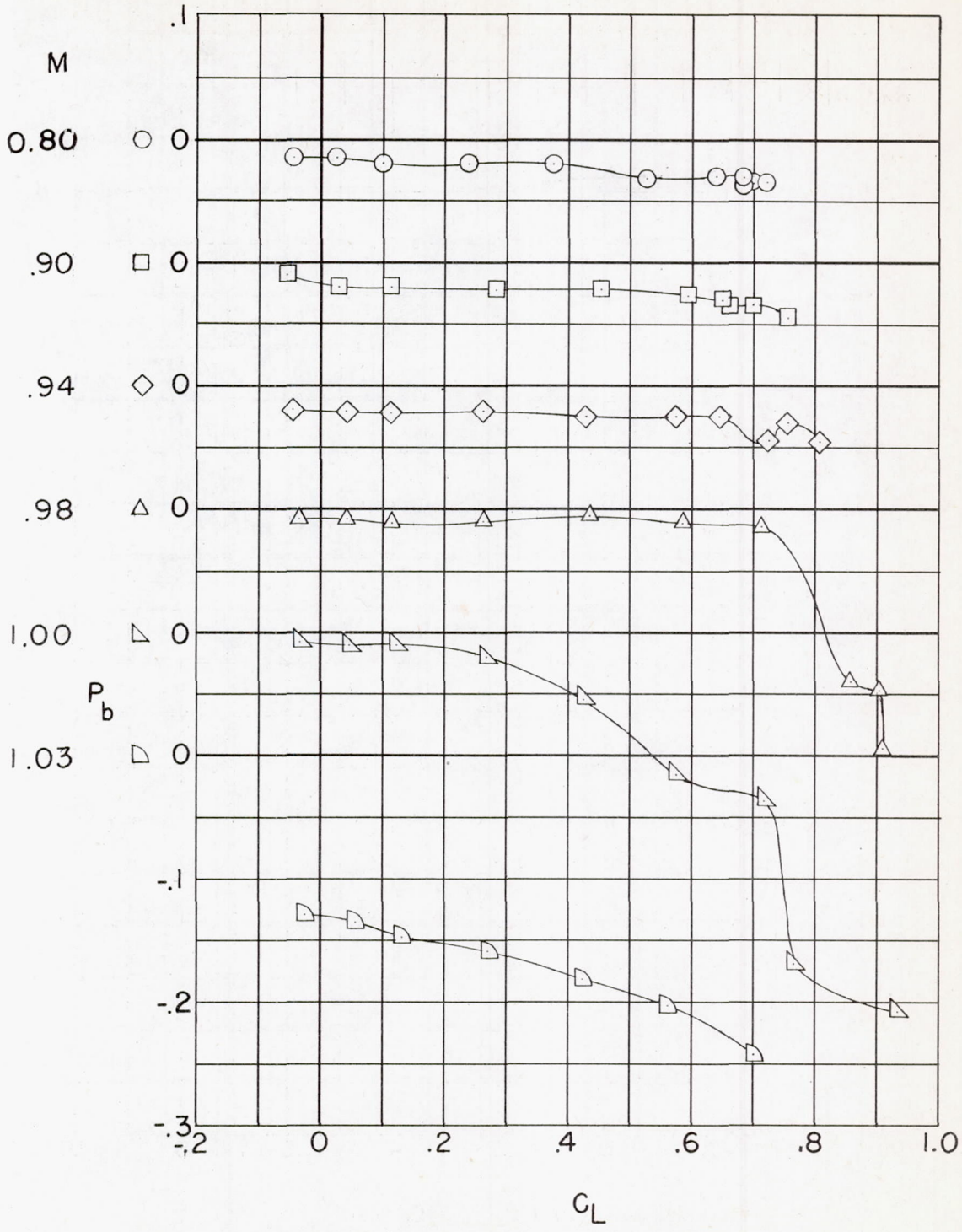
(b) Drag coefficient.

Figure 9.- Continued.



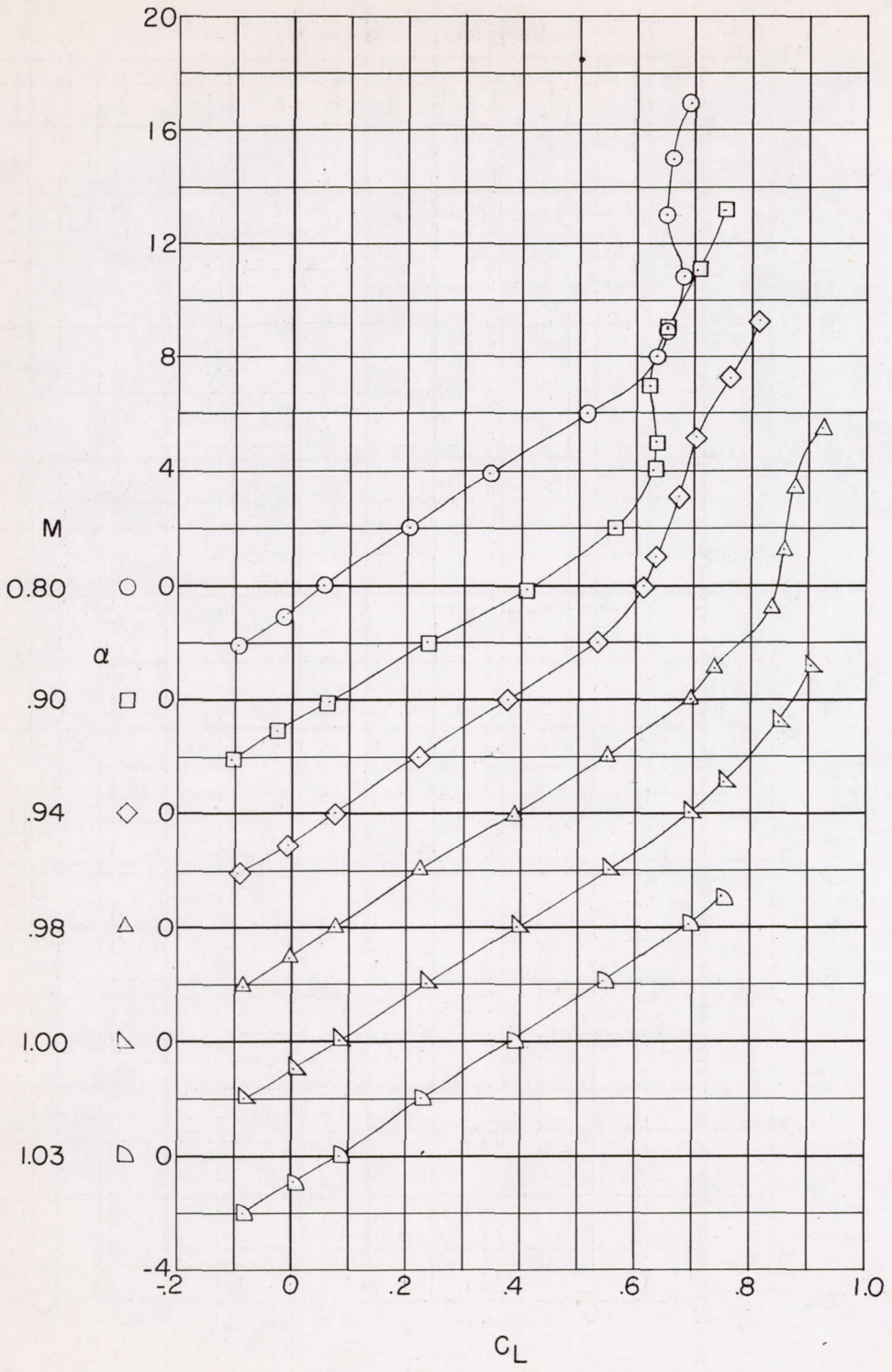
(c) Pitching-moment coefficient.

Figure 9.- Continued.



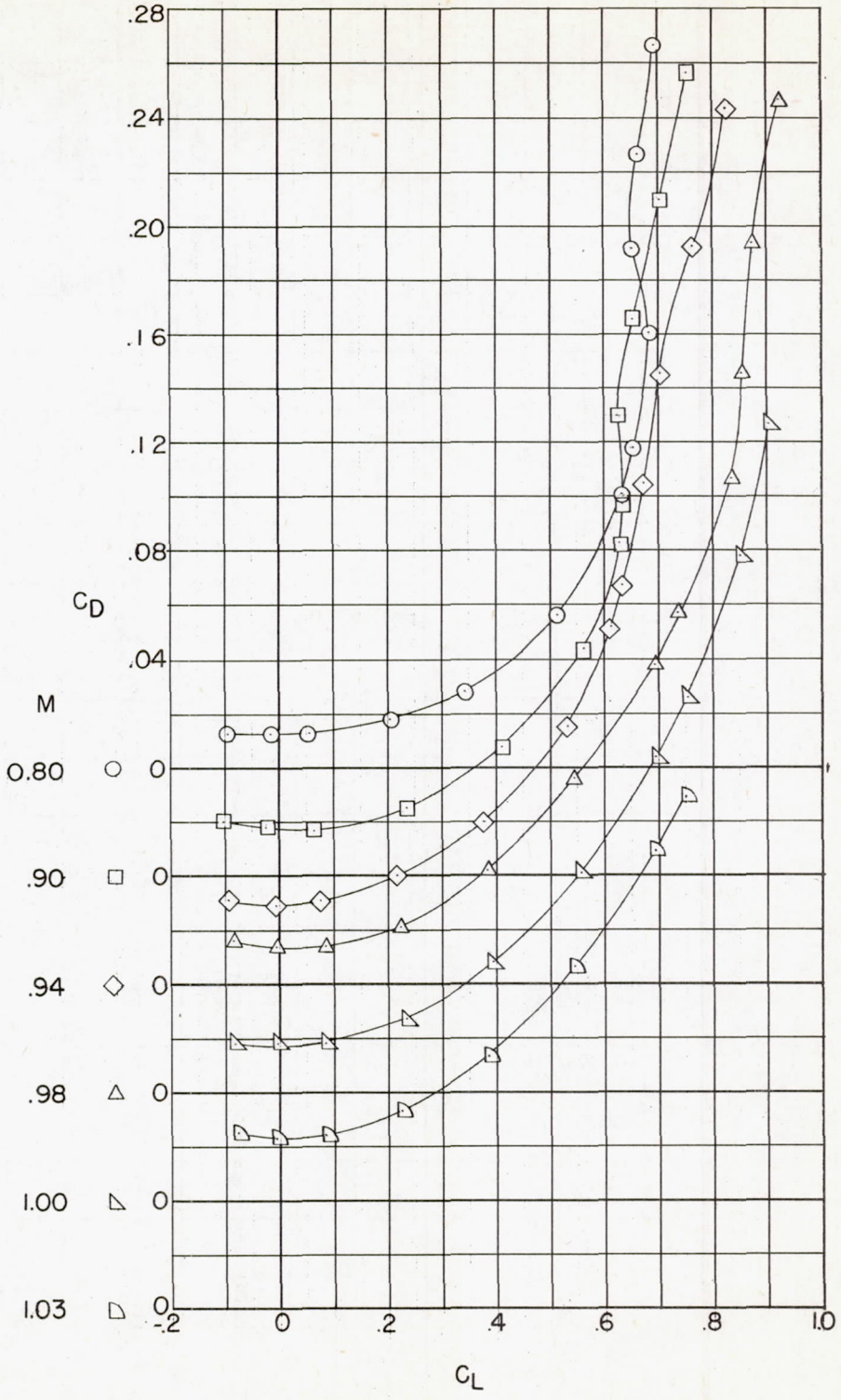
(d) Base pressure coefficient.

Figure 9.- Concluded.



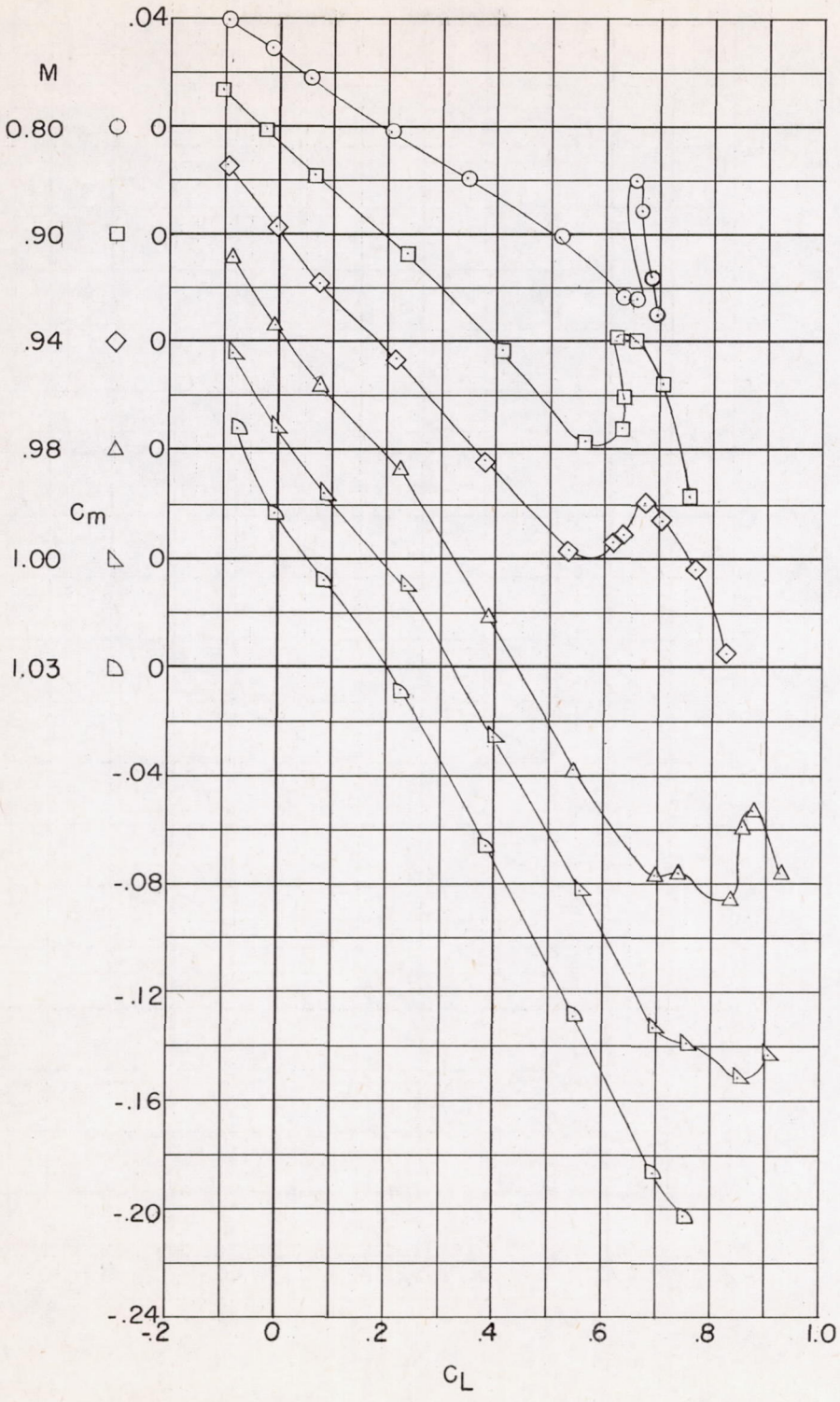
(a) Angle of attack.

Figure 10.- Longitudinal characteristics of the complete model with pylon and store installed. $i_t = 0^o$.



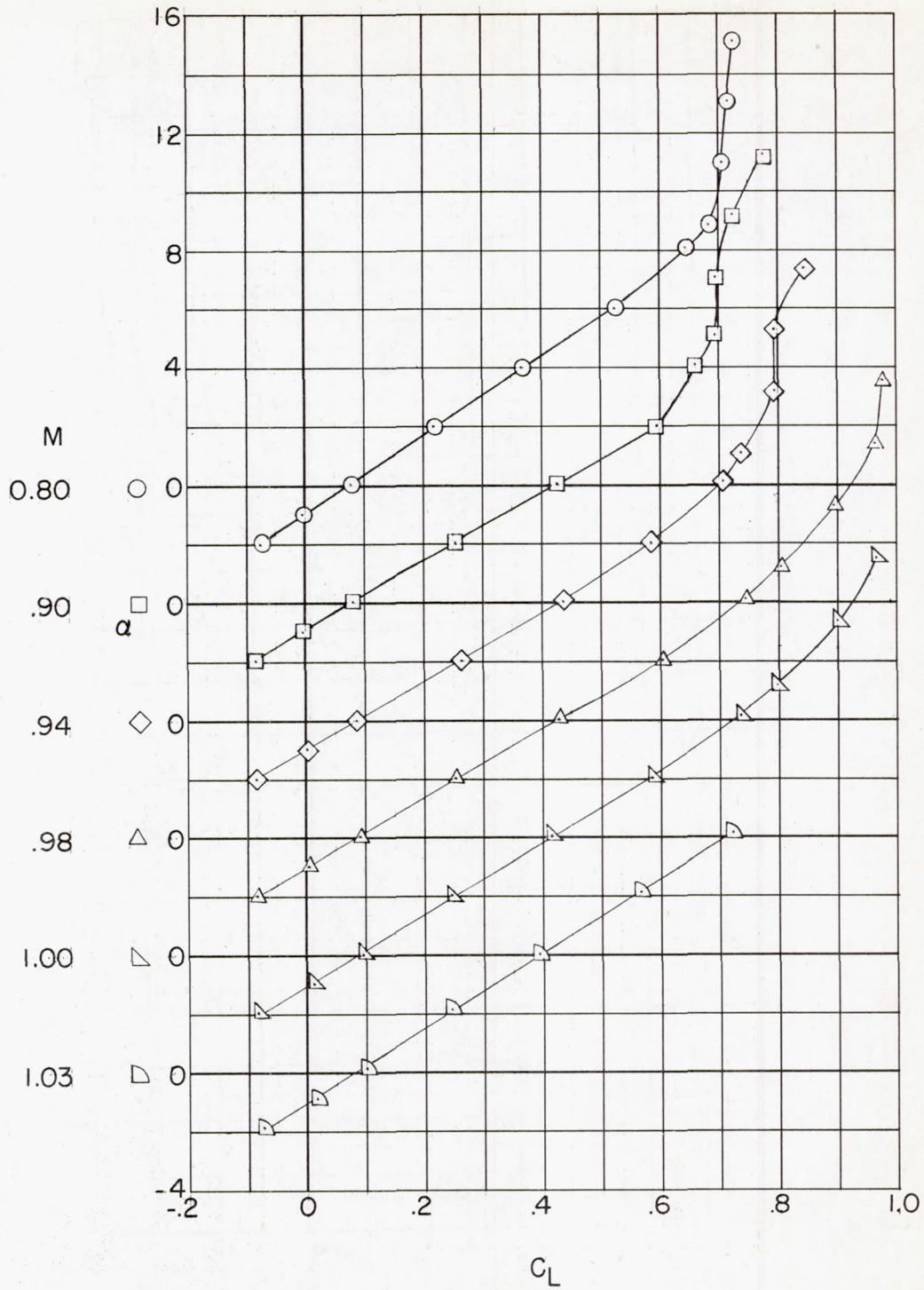
(b) Drag coefficient.

Figure 10.- Continued.



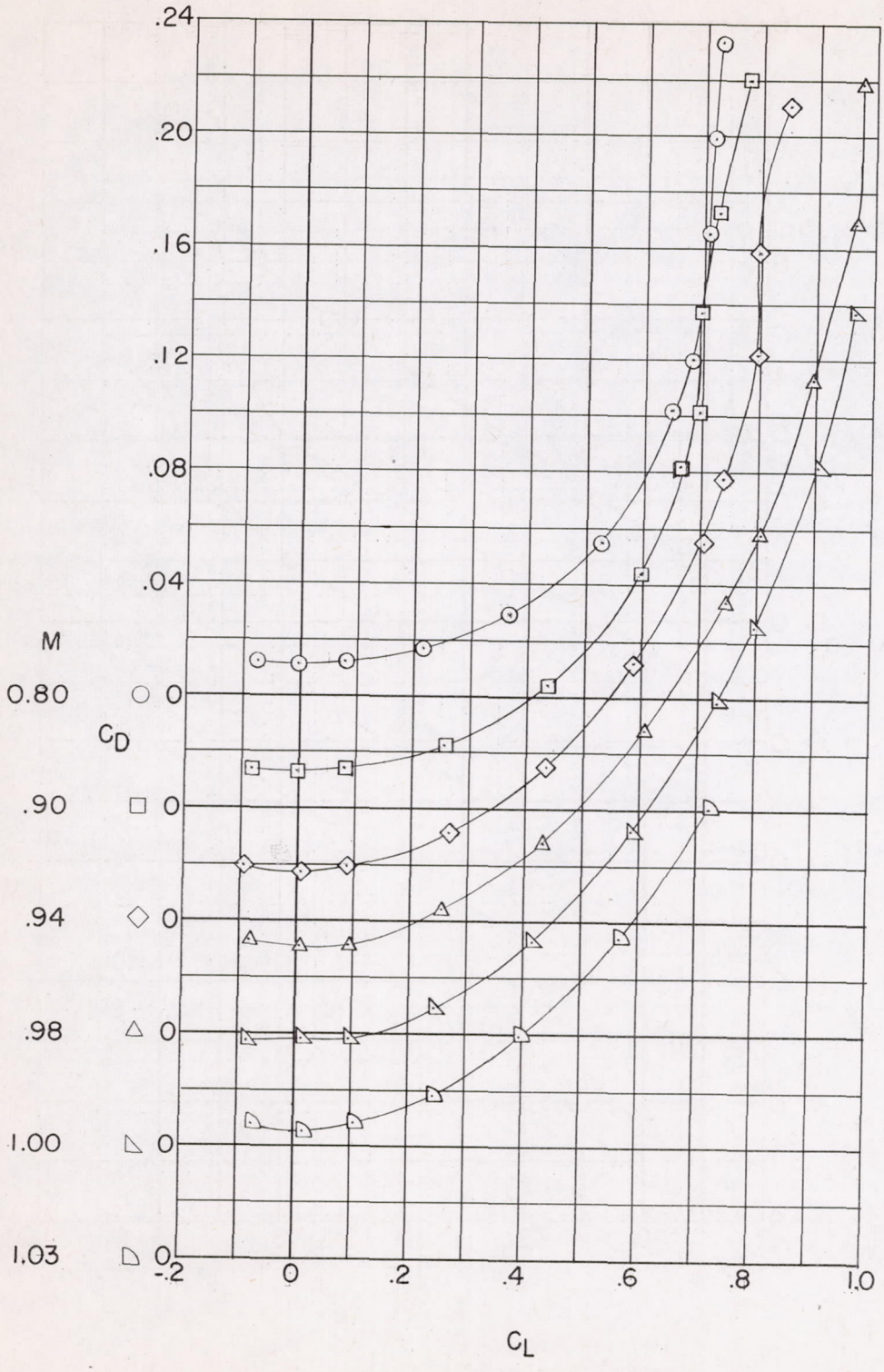
(c) Pitching-moment coefficient.

Figure 10.- Concluded.



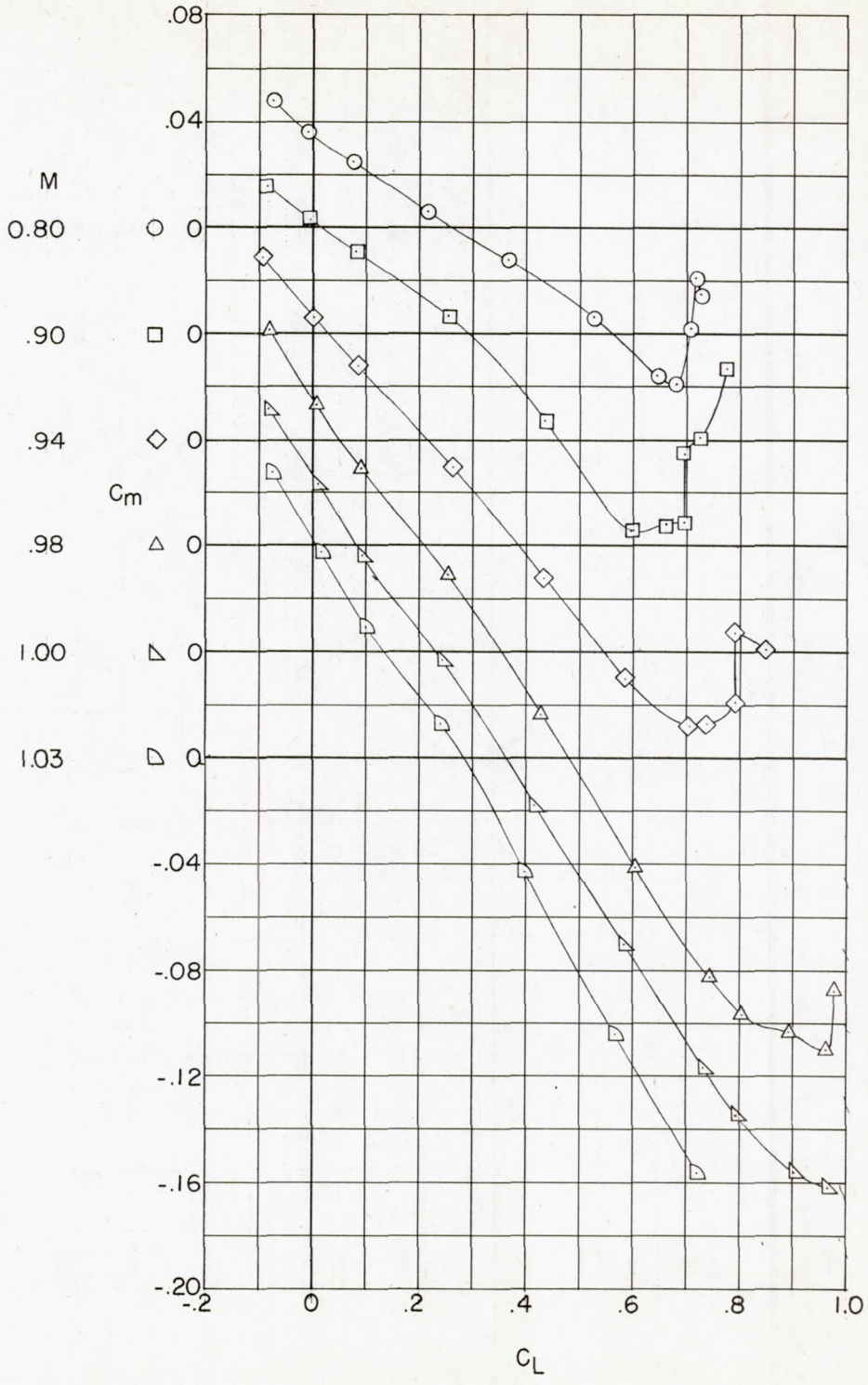
(a) Angle of attack.

Figure 11.- Longitudinal characteristics of the complete model with full afterbody modification. $i_t = 0^o$.



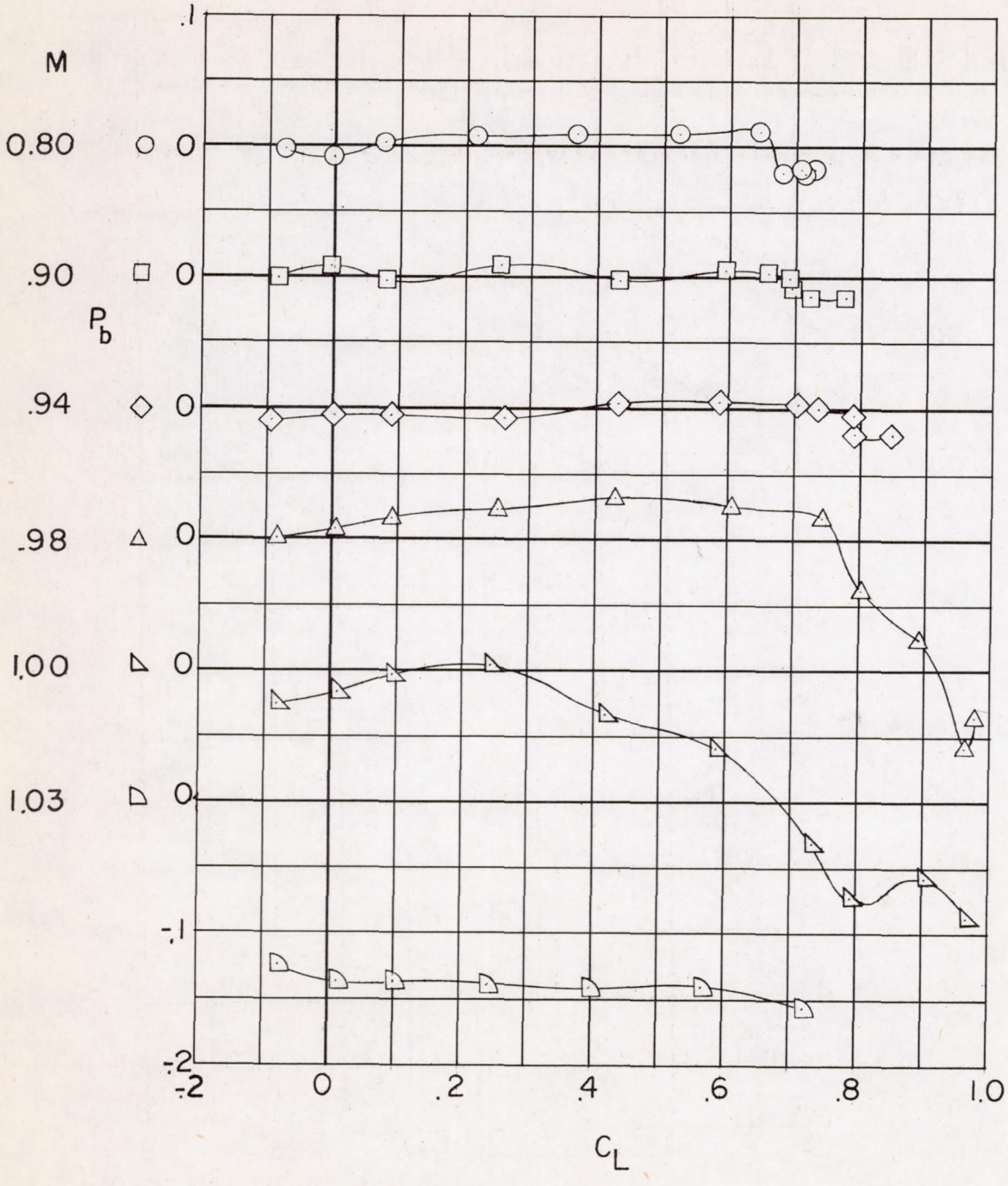
(b) Drag coefficient.

Figure 11.- Continued.



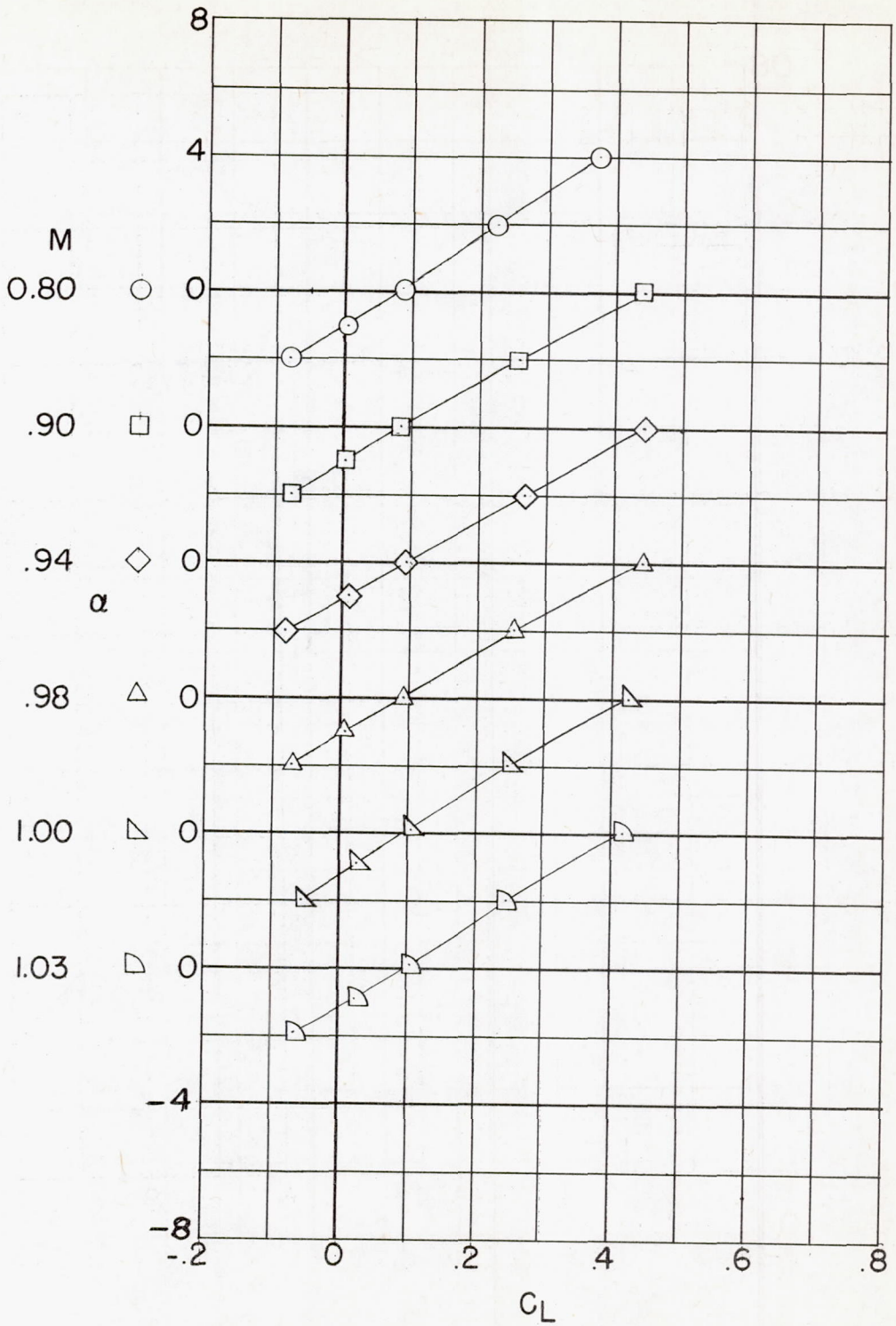
(c) Pitching-moment coefficient.

Figure 11.- Continued.



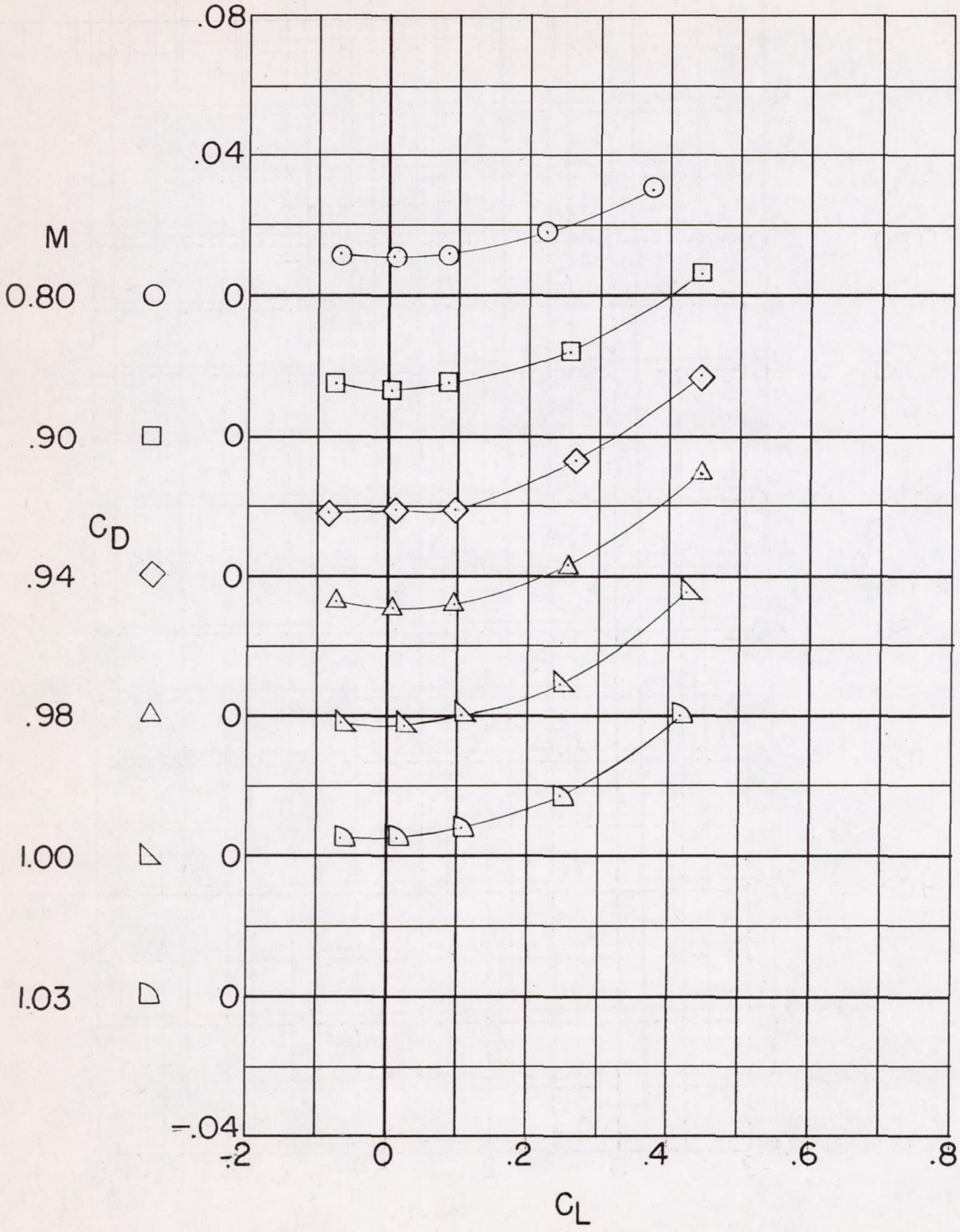
(d) Base pressure coefficient.

Figure 11.- Concluded.



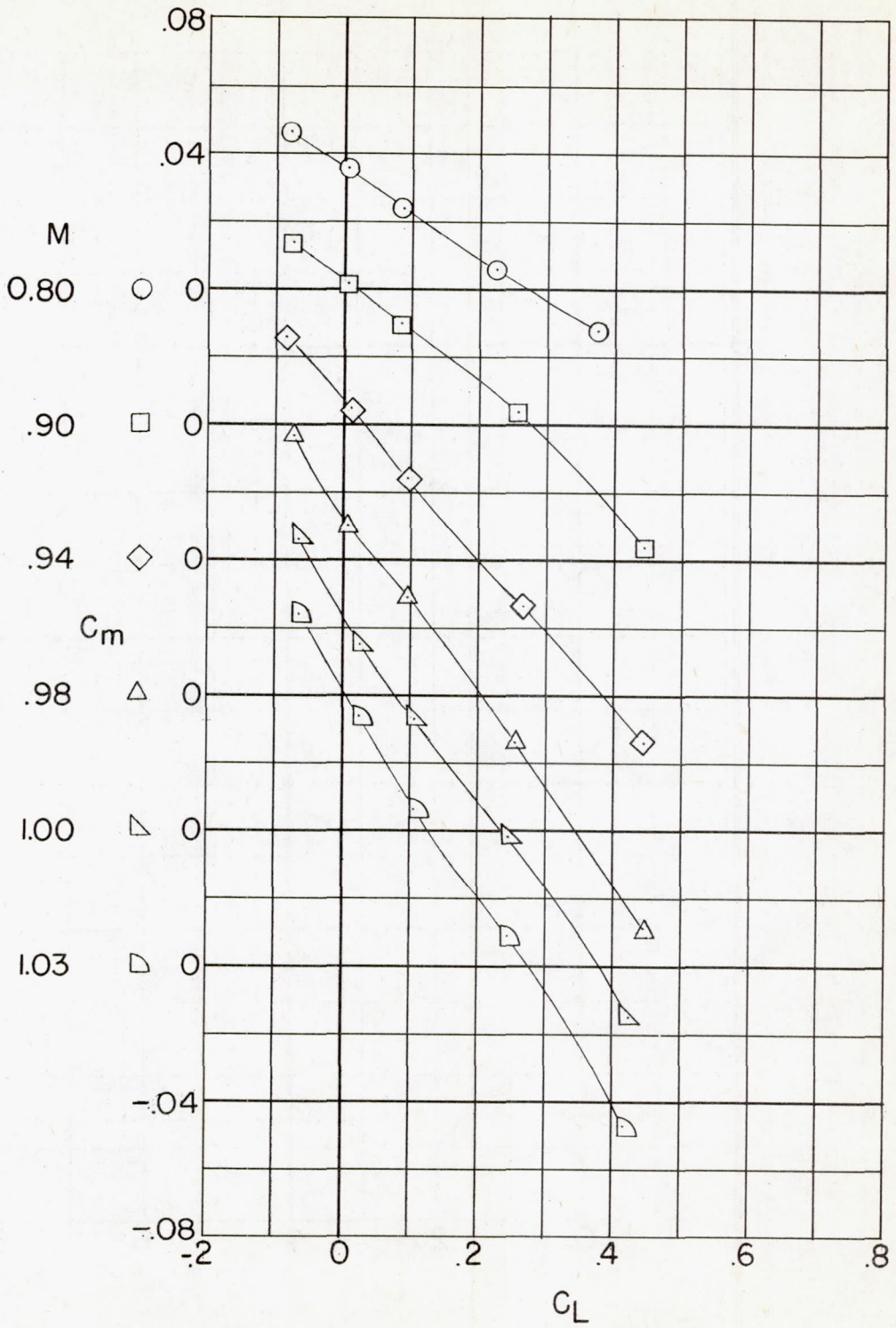
(a) Angle of attack.

Figure 12.- Longitudinal characteristics of the complete model with 75 percent afterbody modification. $i_t = 0^o$.



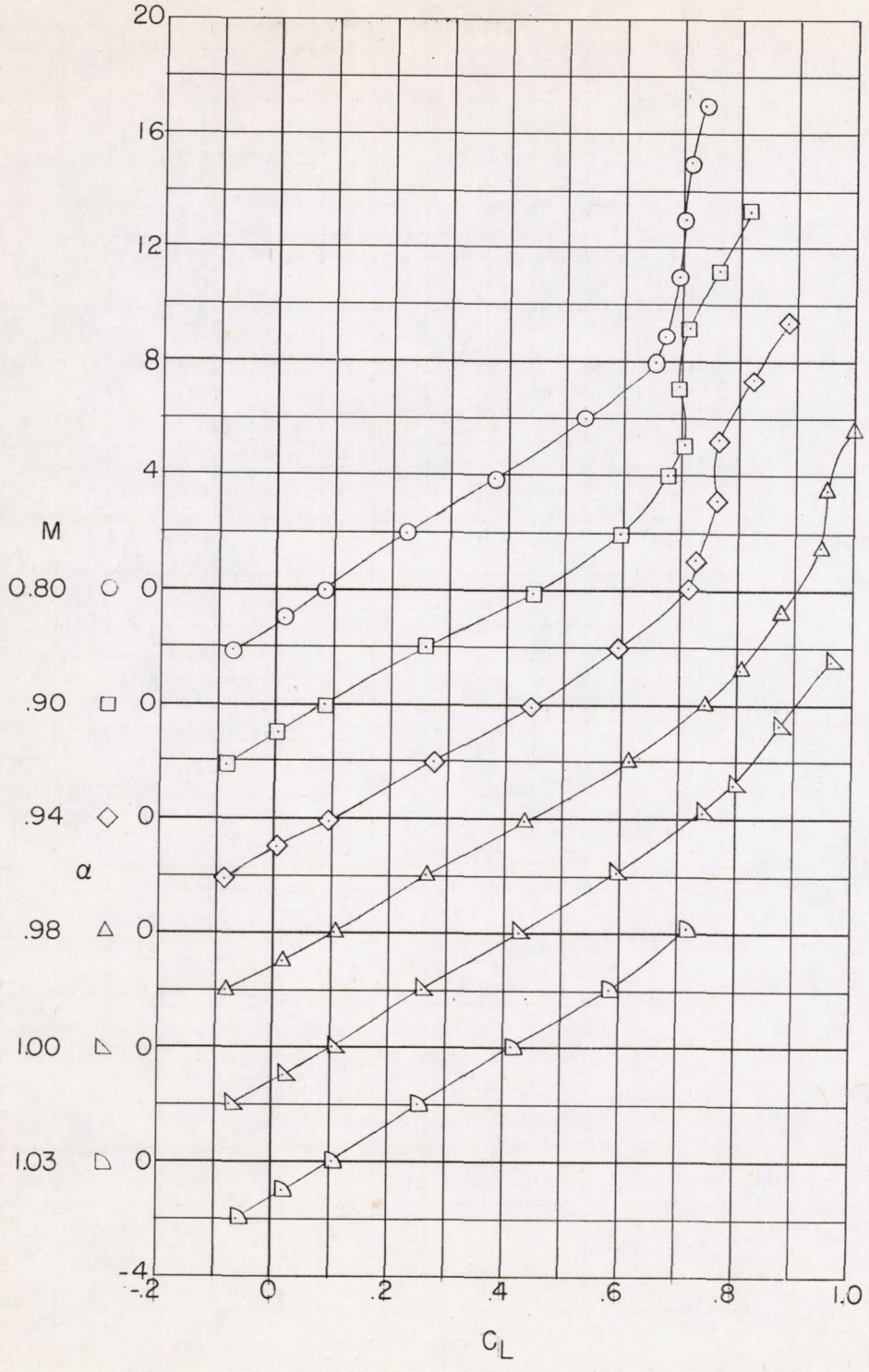
(b) Drag coefficient.

Figure 12.- Continued.



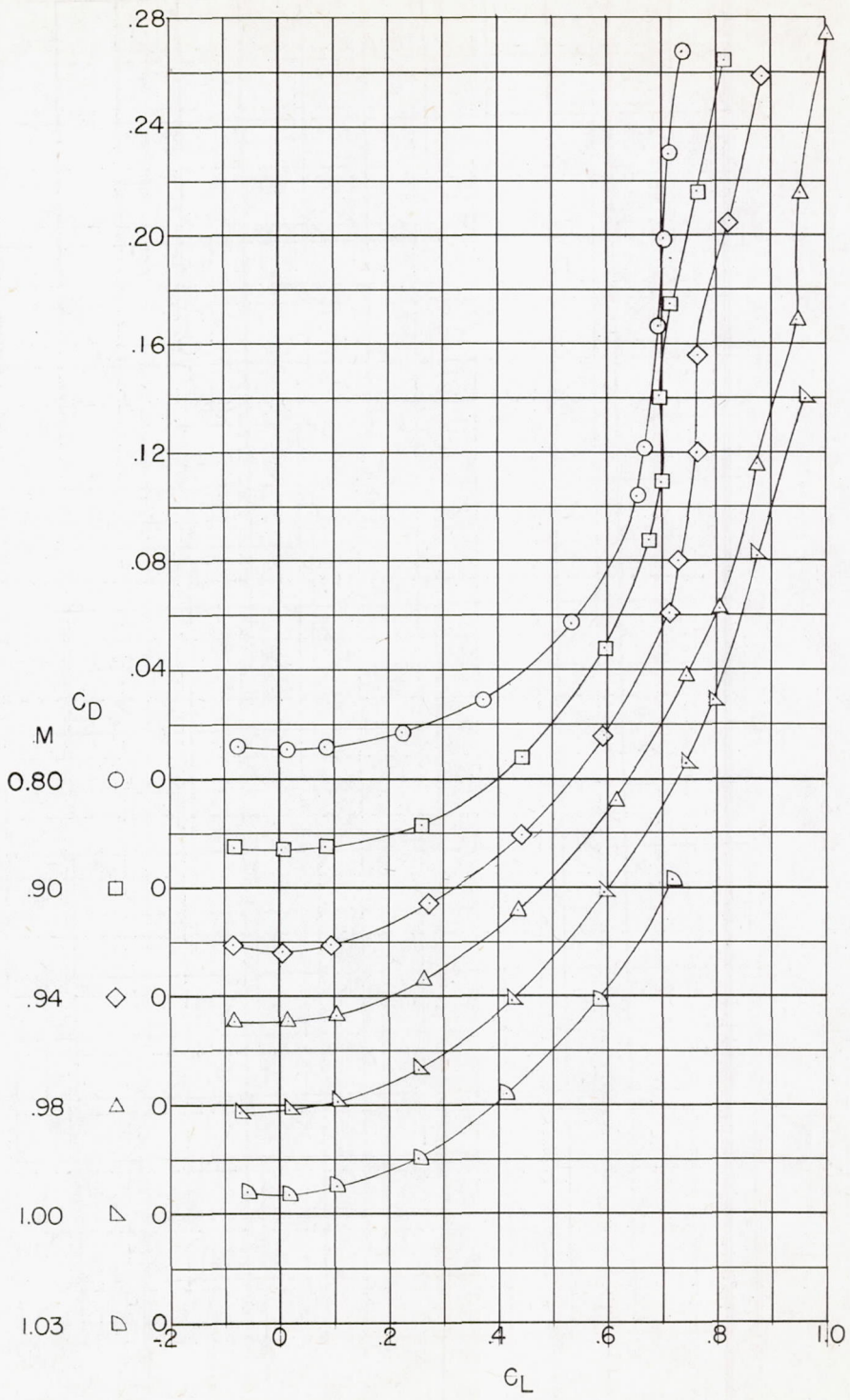
(c) Pitching-moment coefficient.

Figure 12.- Concluded.



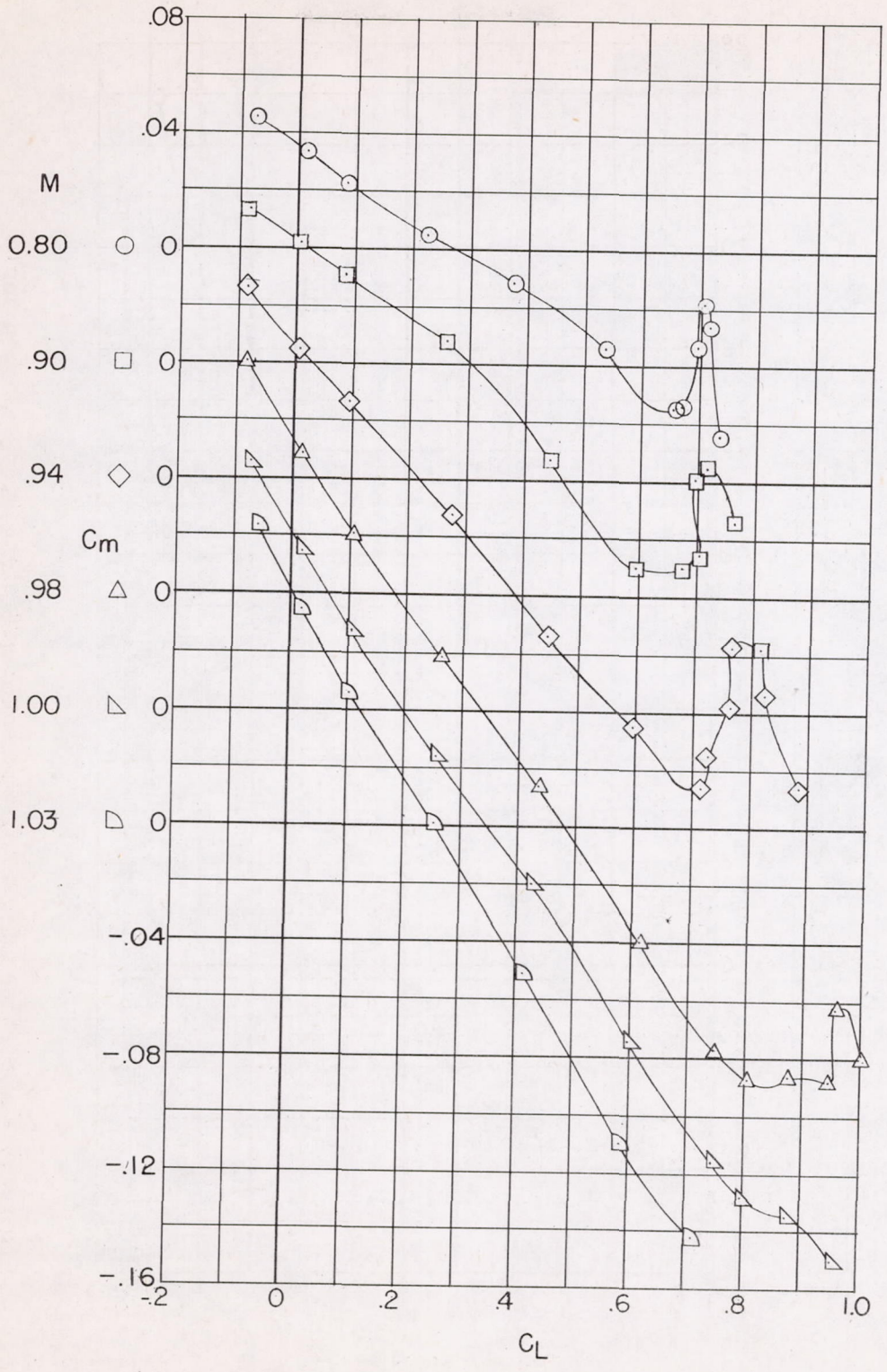
(a) Angle of attack.

Figure 13.- Longitudinal characteristics of the complete model with full afterbody modification and wing-root fillets. $i_t = 0^o$.



(b) Drag coefficient.

Figure 13.- Continued.



(c) Pitching-moment coefficient.

Figure 13.- Concluded.

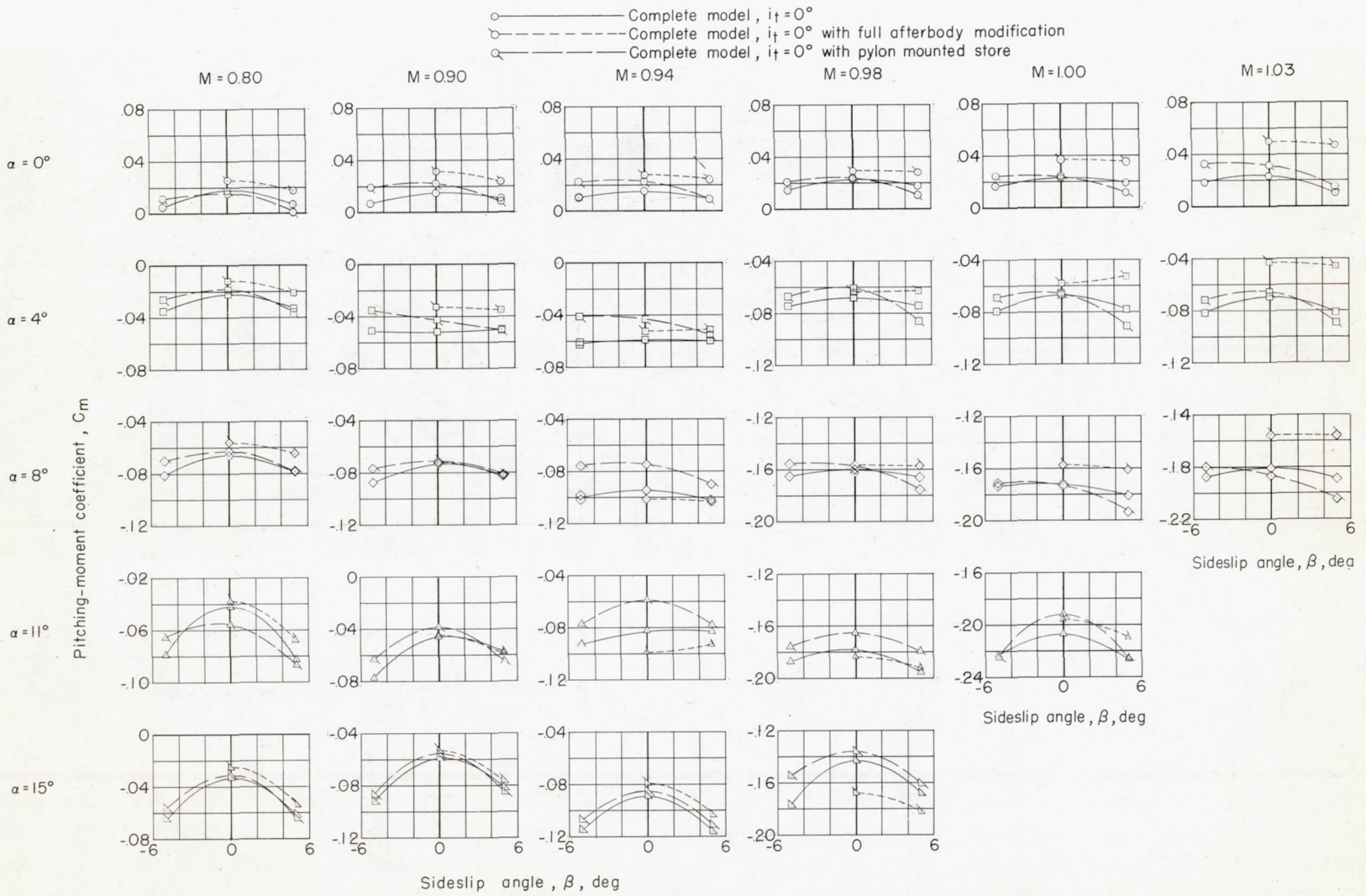
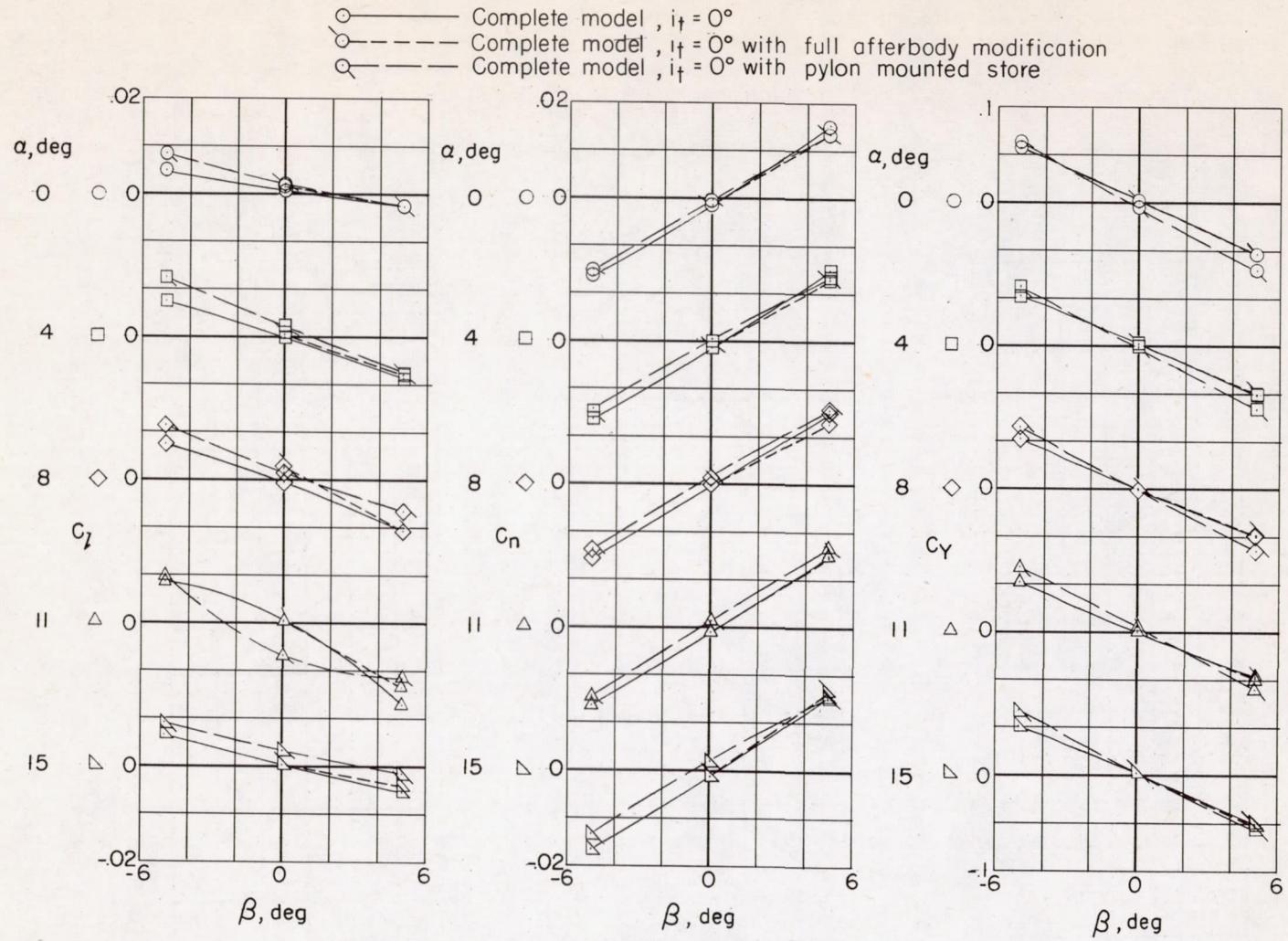
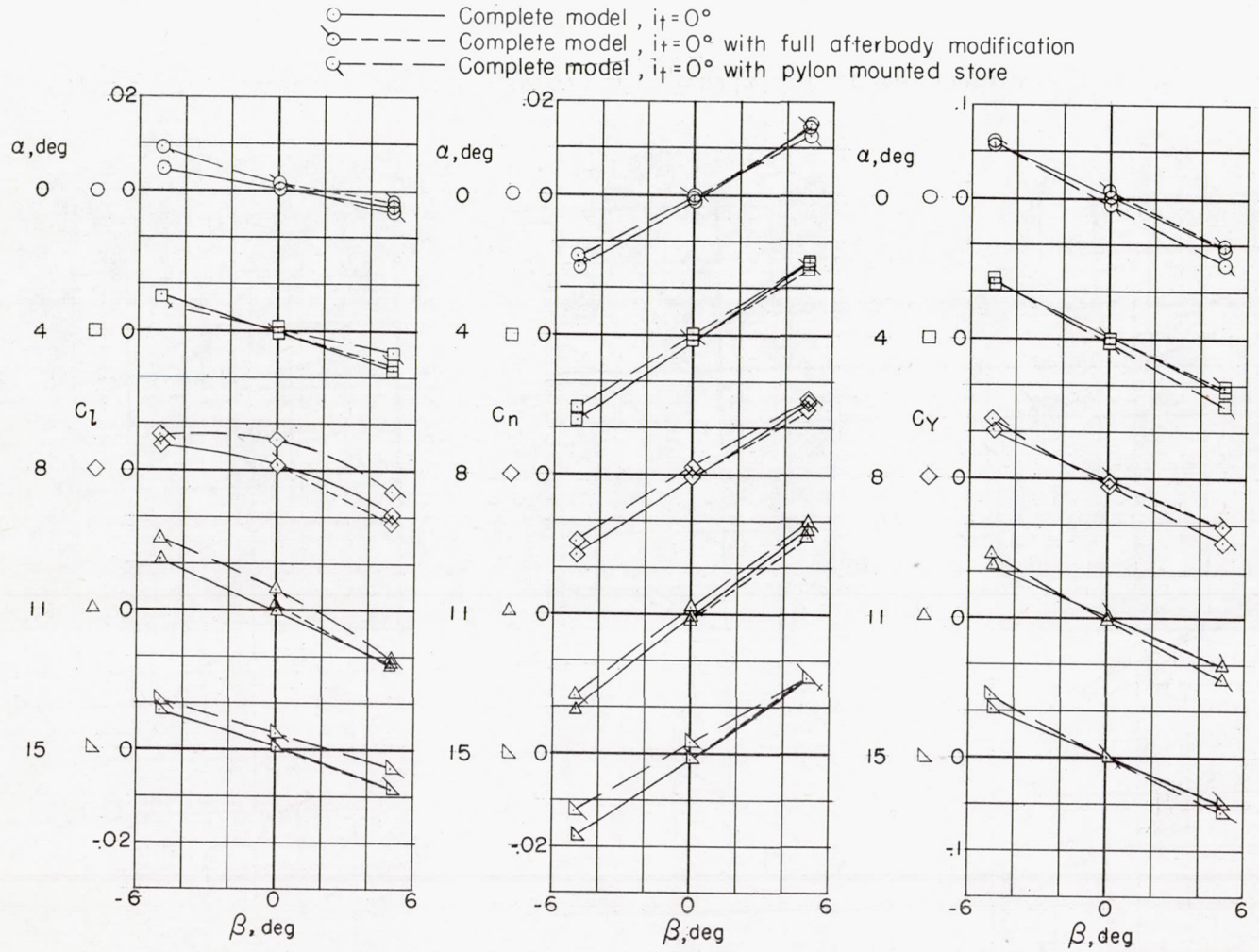


Figure 14.- Variation of pitching-moment coefficient with sideslip angle for three configurations.



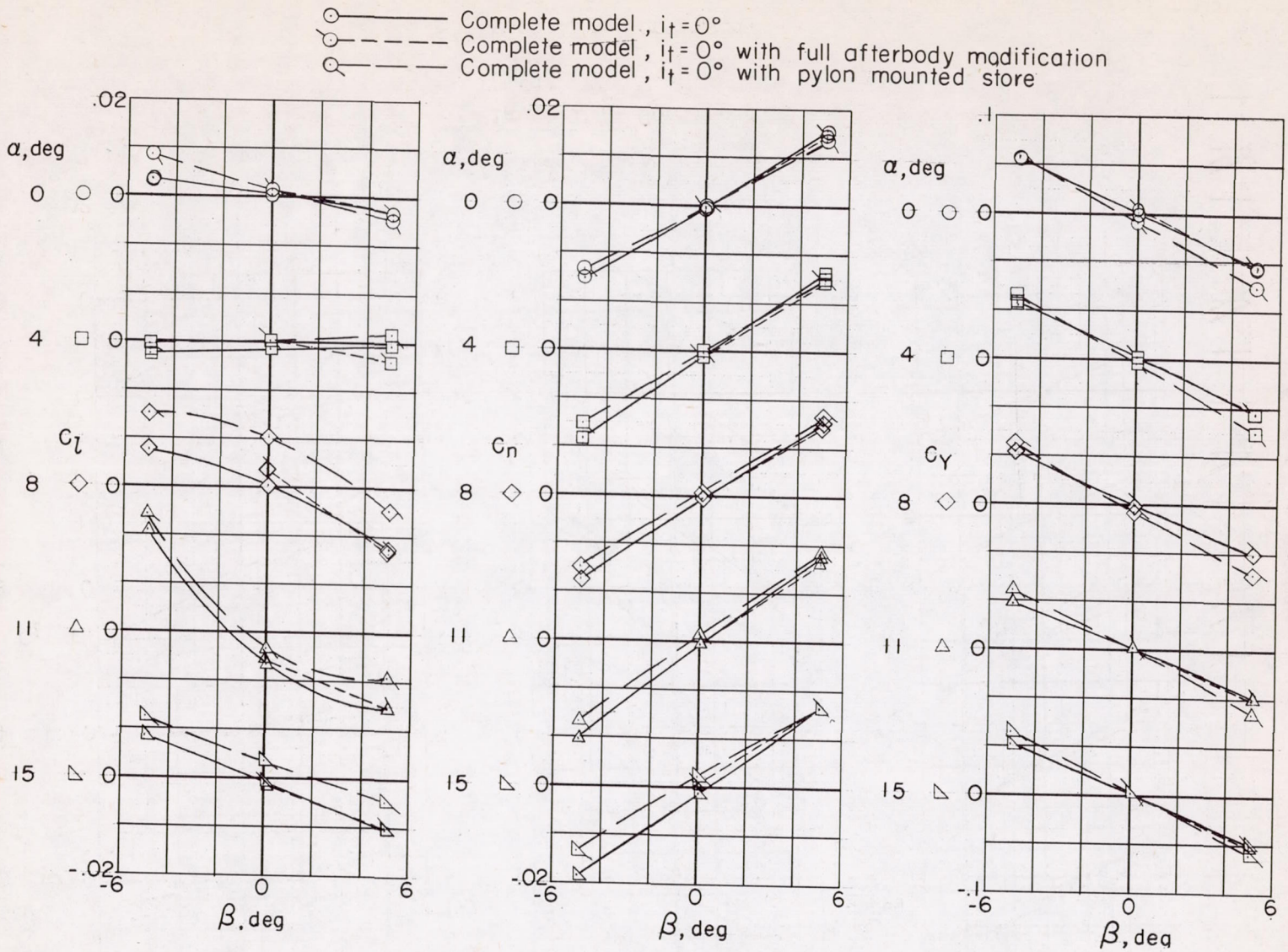
(a) M = 0.80.

Figure 15.- Lateral characteristics in sideslip for three configurations.



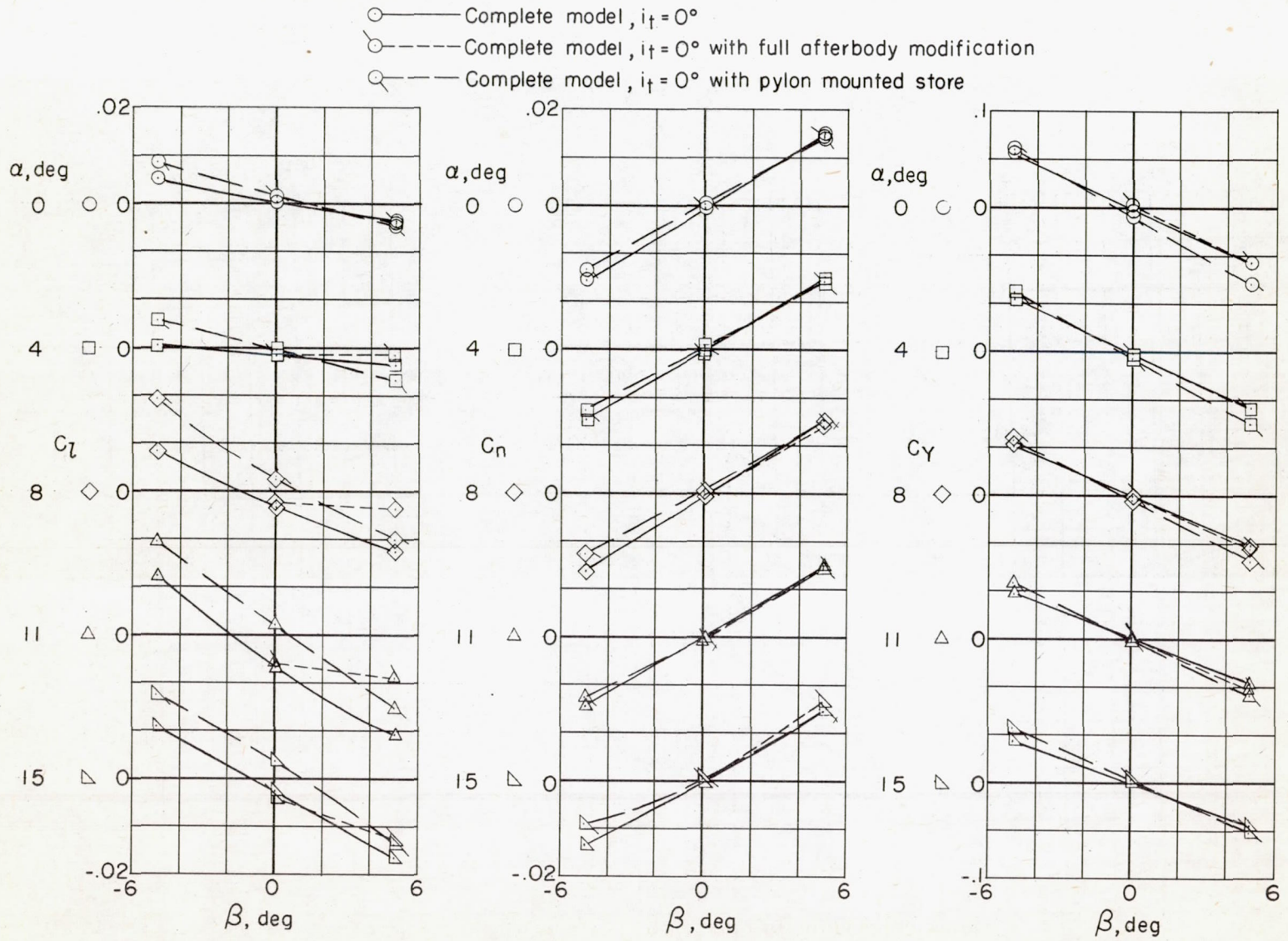
(b) M = 0.90.

Figure 15.- Continued.



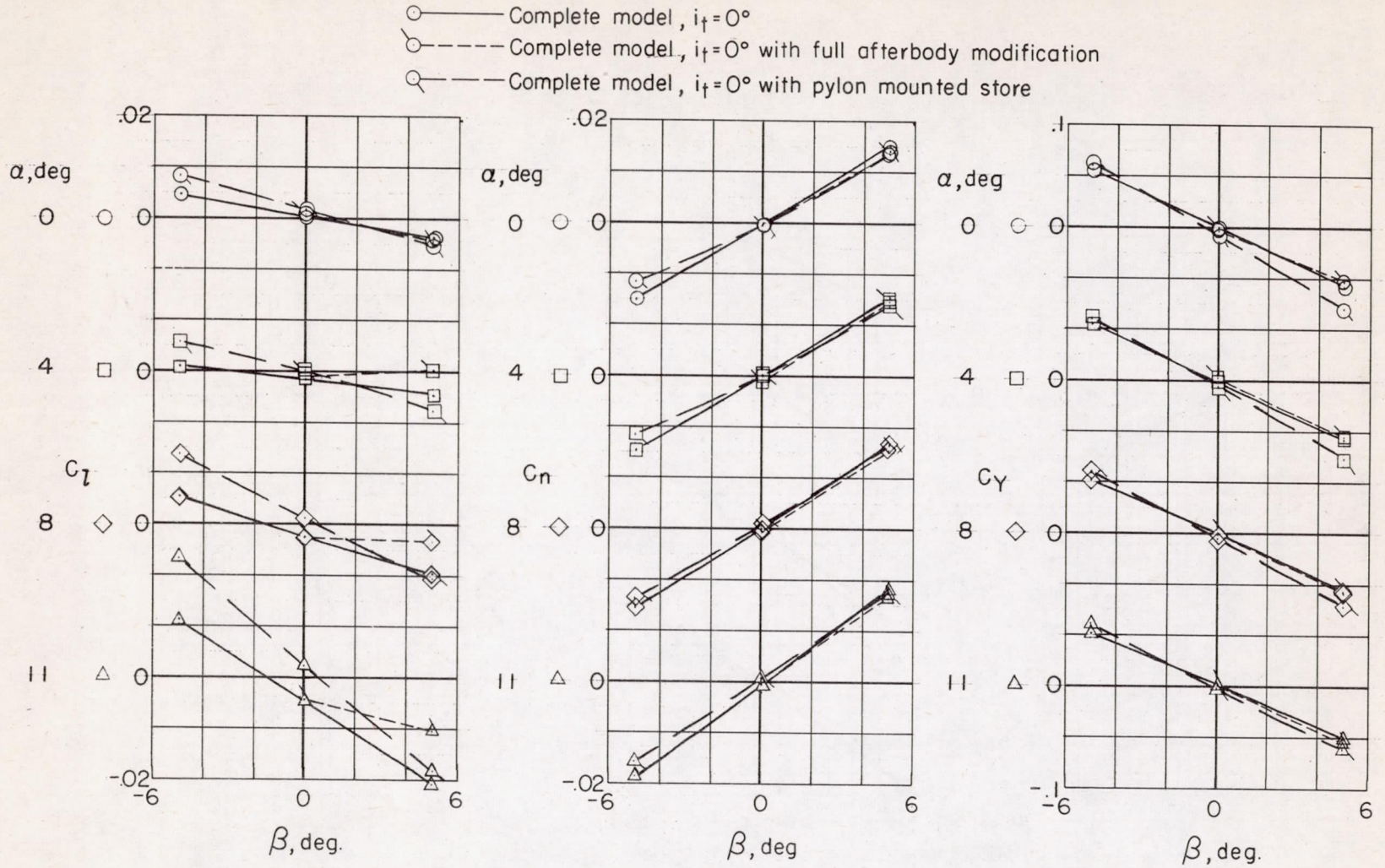
(c) M = 0.94.

Figure 15.- Continued.



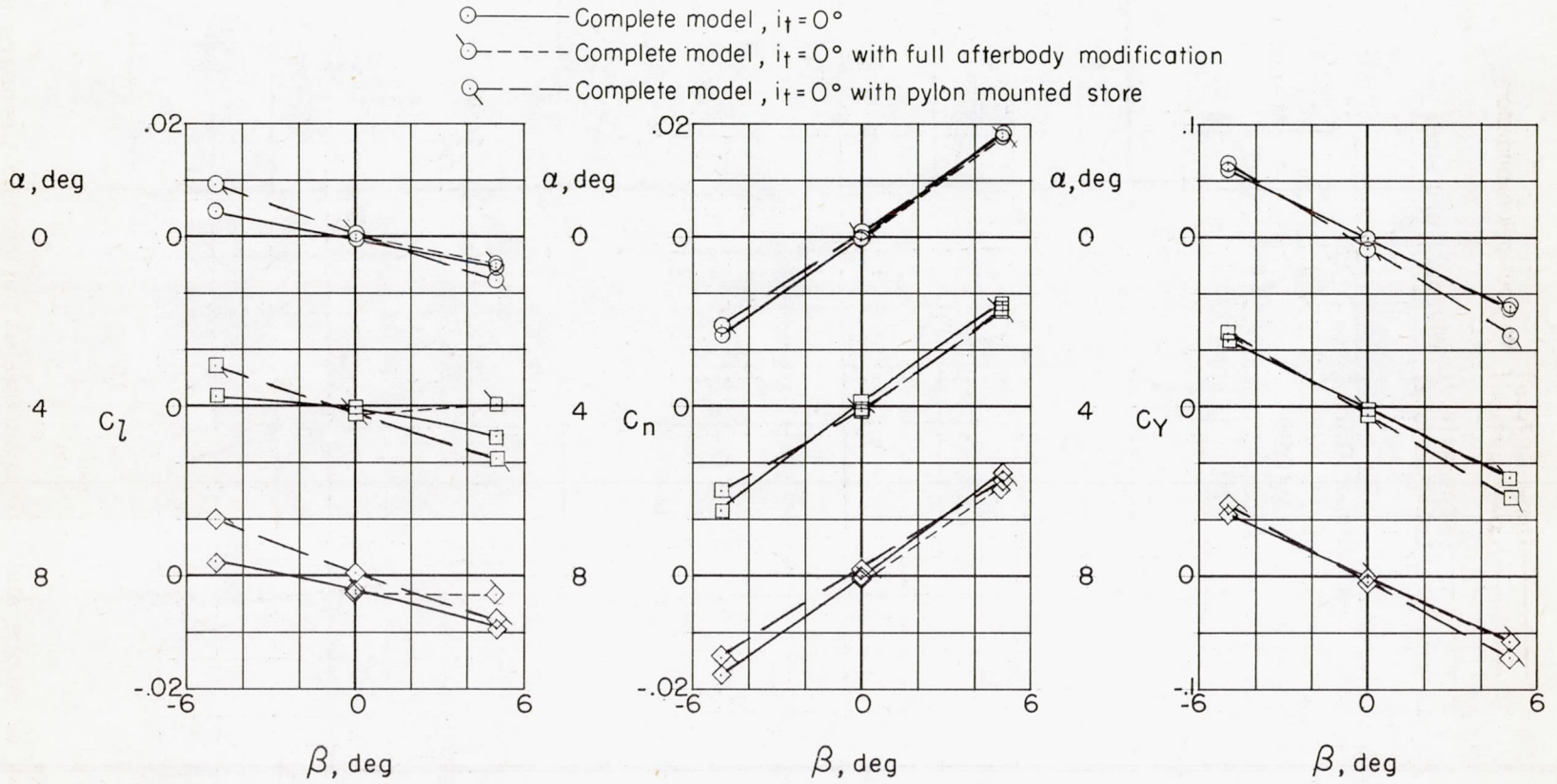
(d) M = 0.98.

Figure 15.- Continued.



(e) M = 1.00.

Figure 15.- Continued.



(f) M = 1.03.

Figure 15.- Concluded.

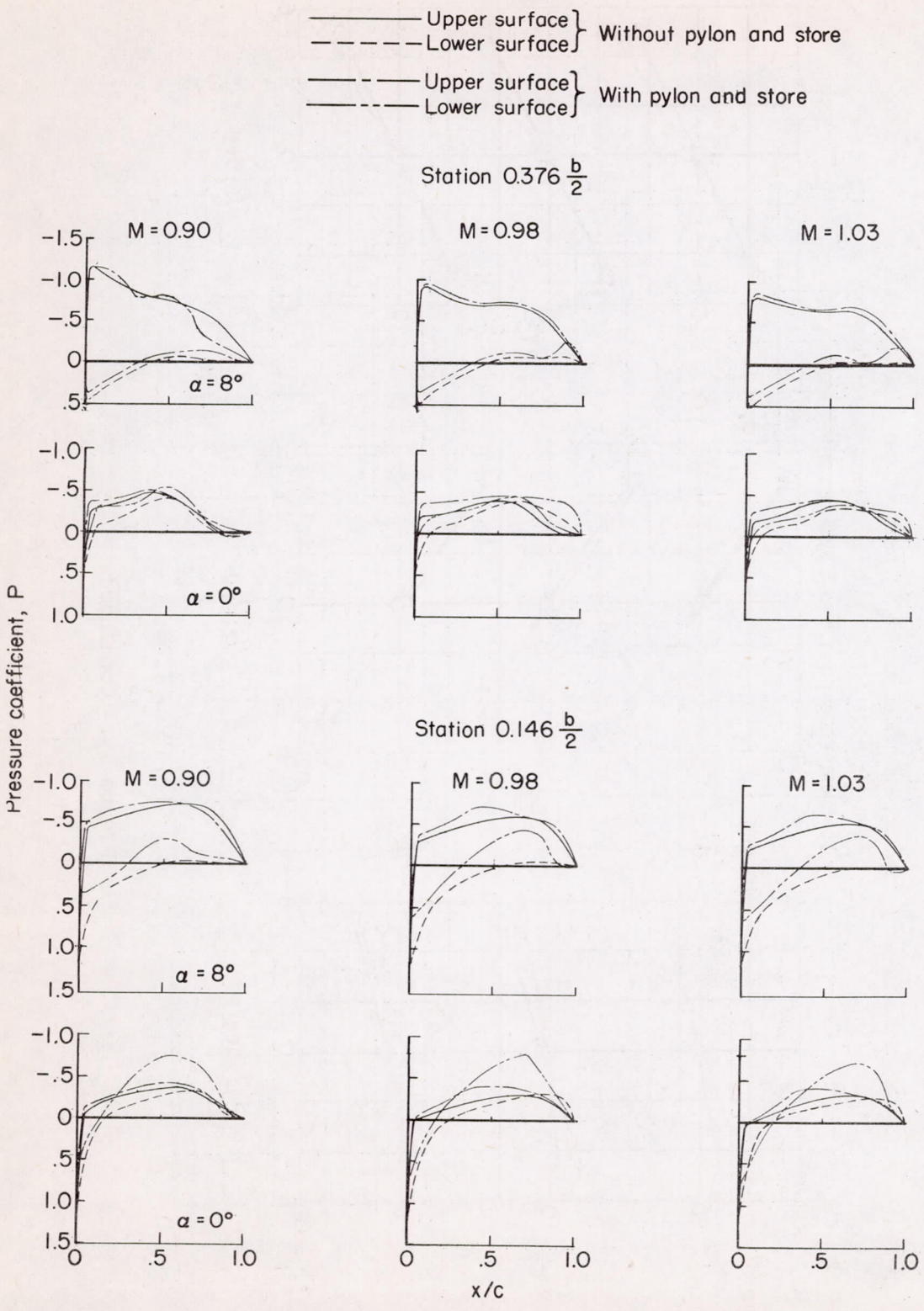


Figure 16.- Effect of store and pylon installation on the pressure distribution of two spanwise wing stations.

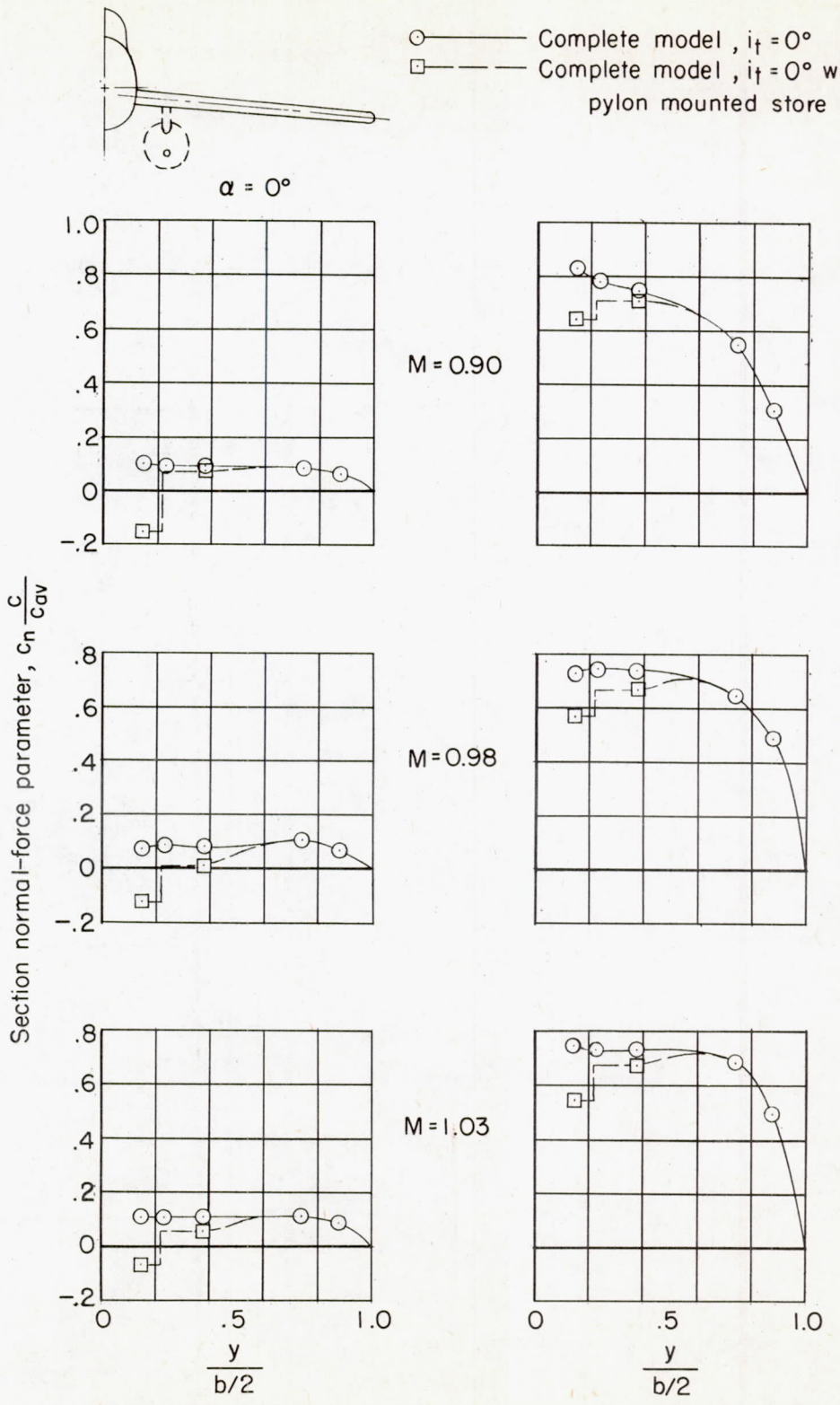


Figure 17.- Typical effect of pylon and store on wing load distribution.

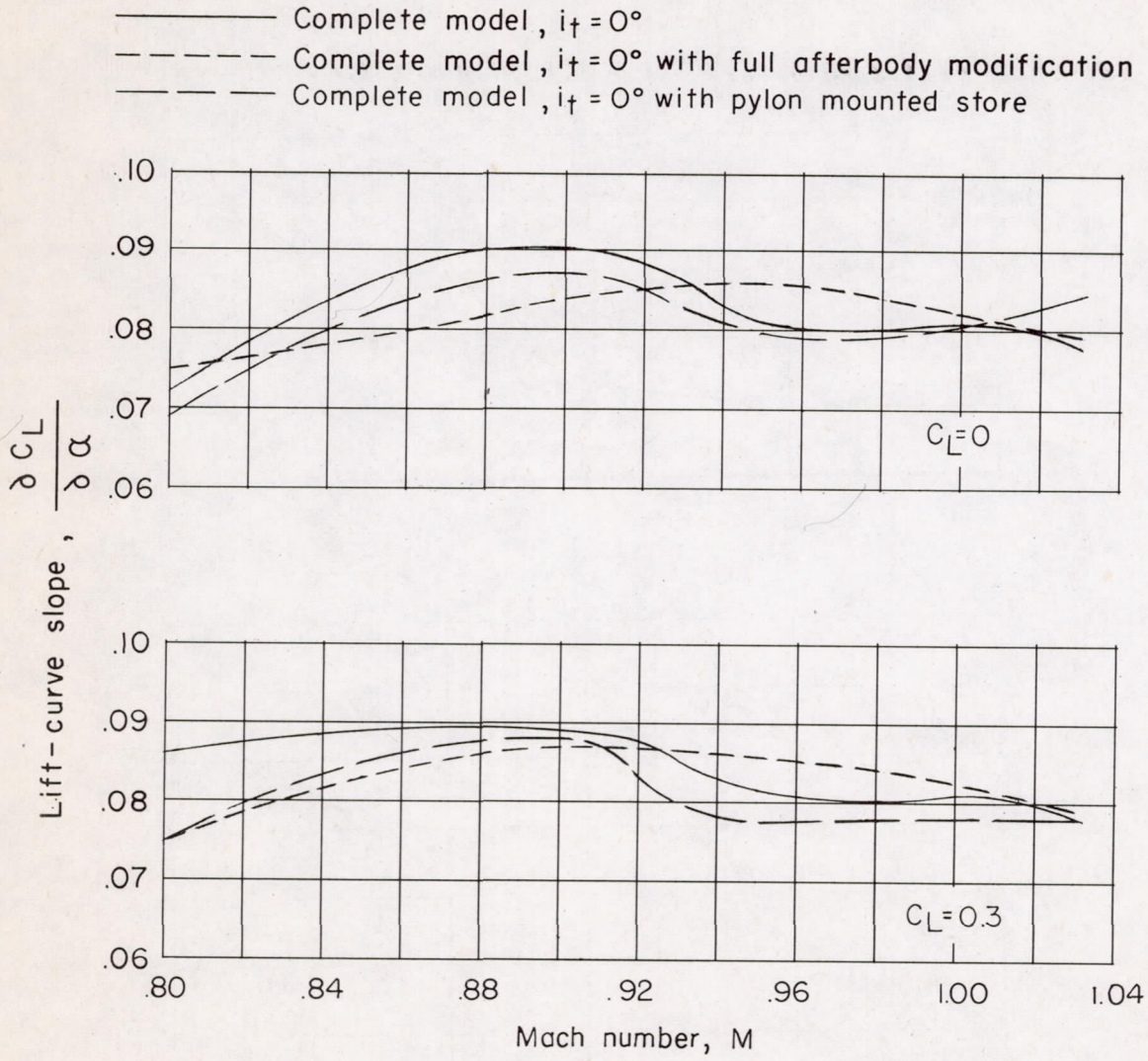


Figure 18.- Variation of the lift-curve slope with Mach number for three configurations.

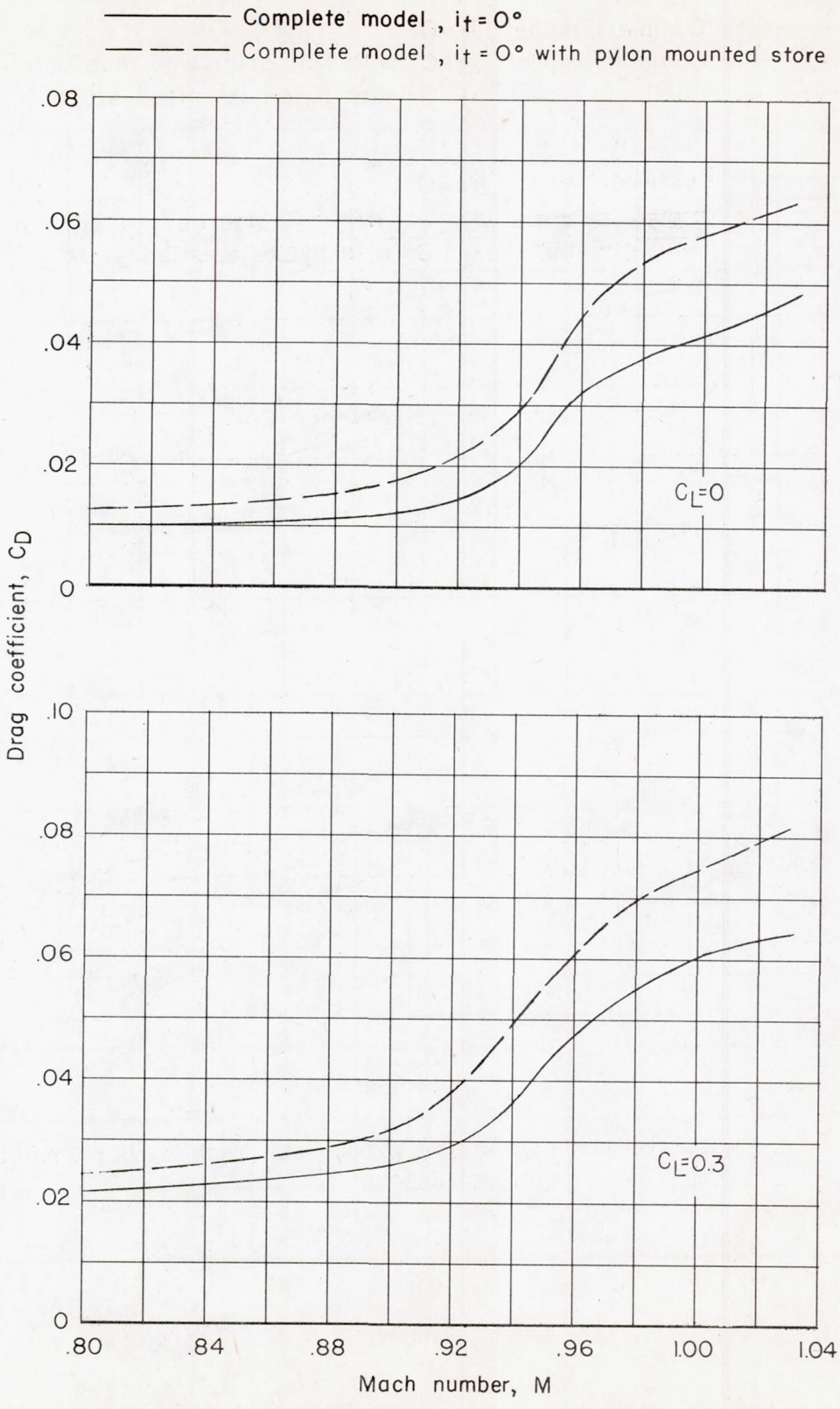


Figure 19.- Effect of pylon and store installation on drag coefficient.

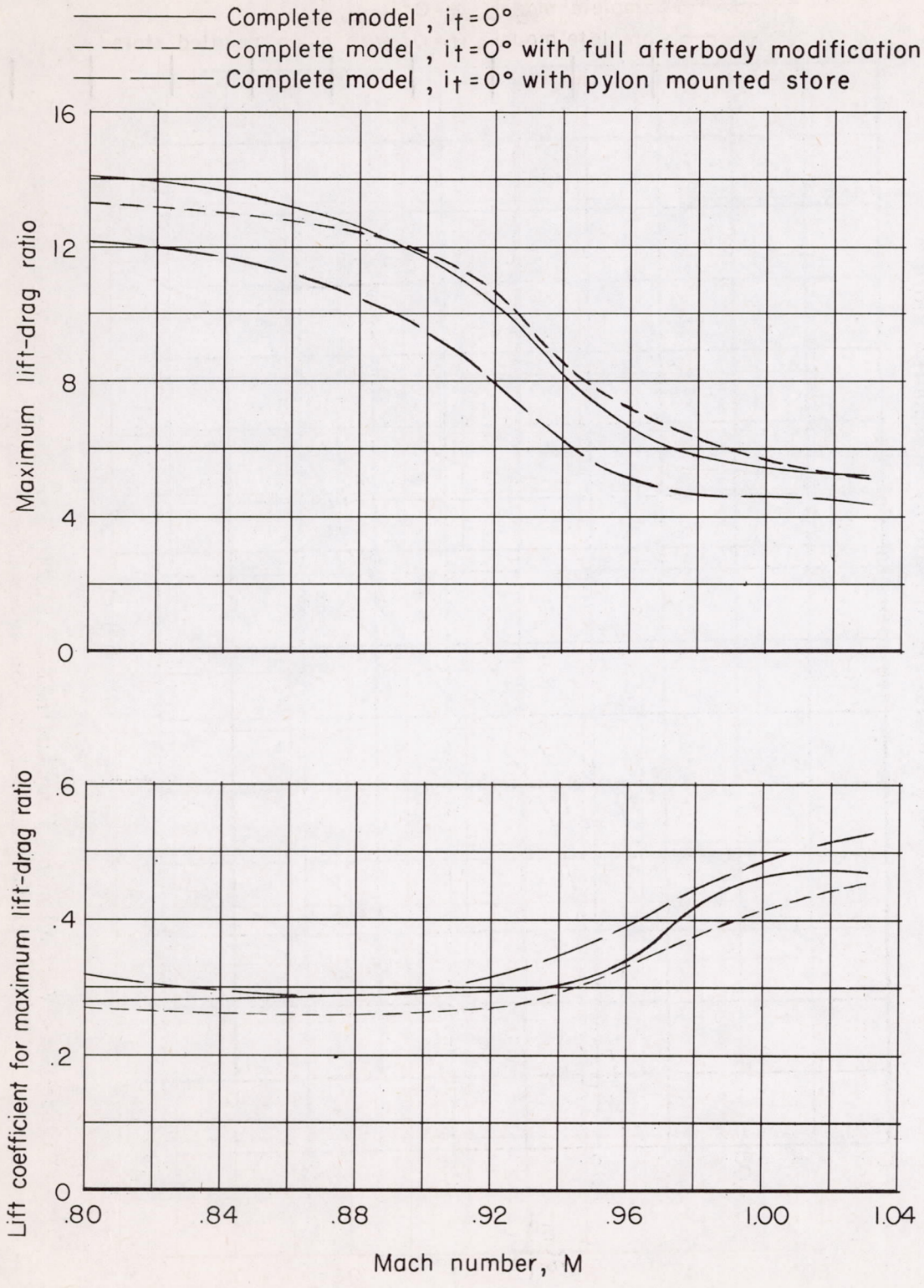


Figure 20.- Effect of Mach number on the maximum lift-drag ratio and lift coefficient for maximum lift-drag ratio.

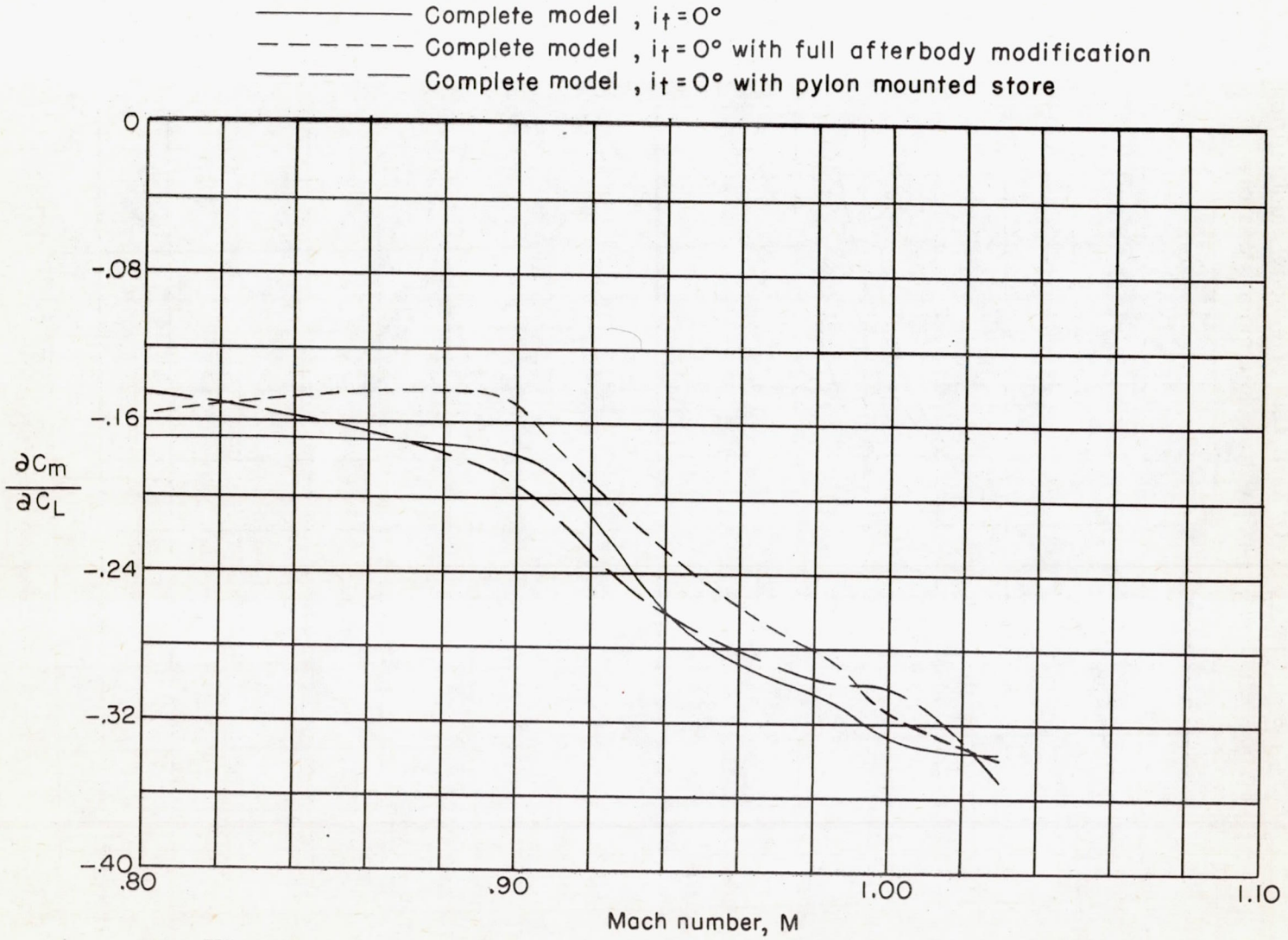


Figure 21.- Variation of longitudinal-stability parameter with Mach number at zero lift coefficient for several configurations.

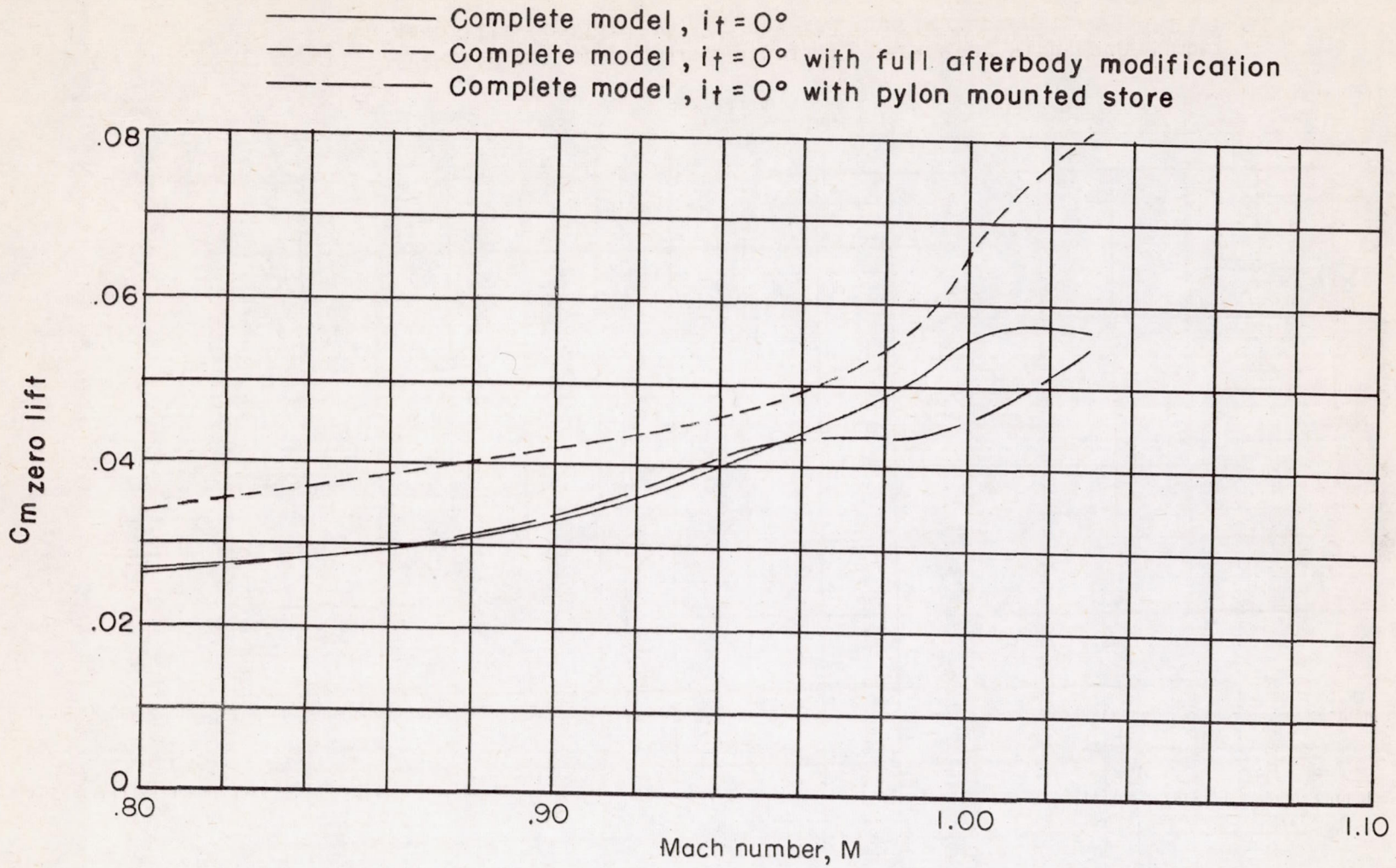


Figure 22.- Variation of pitching-moment coefficient with Mach number at zero lift coefficient for several configurations. $i_t = 0°$.

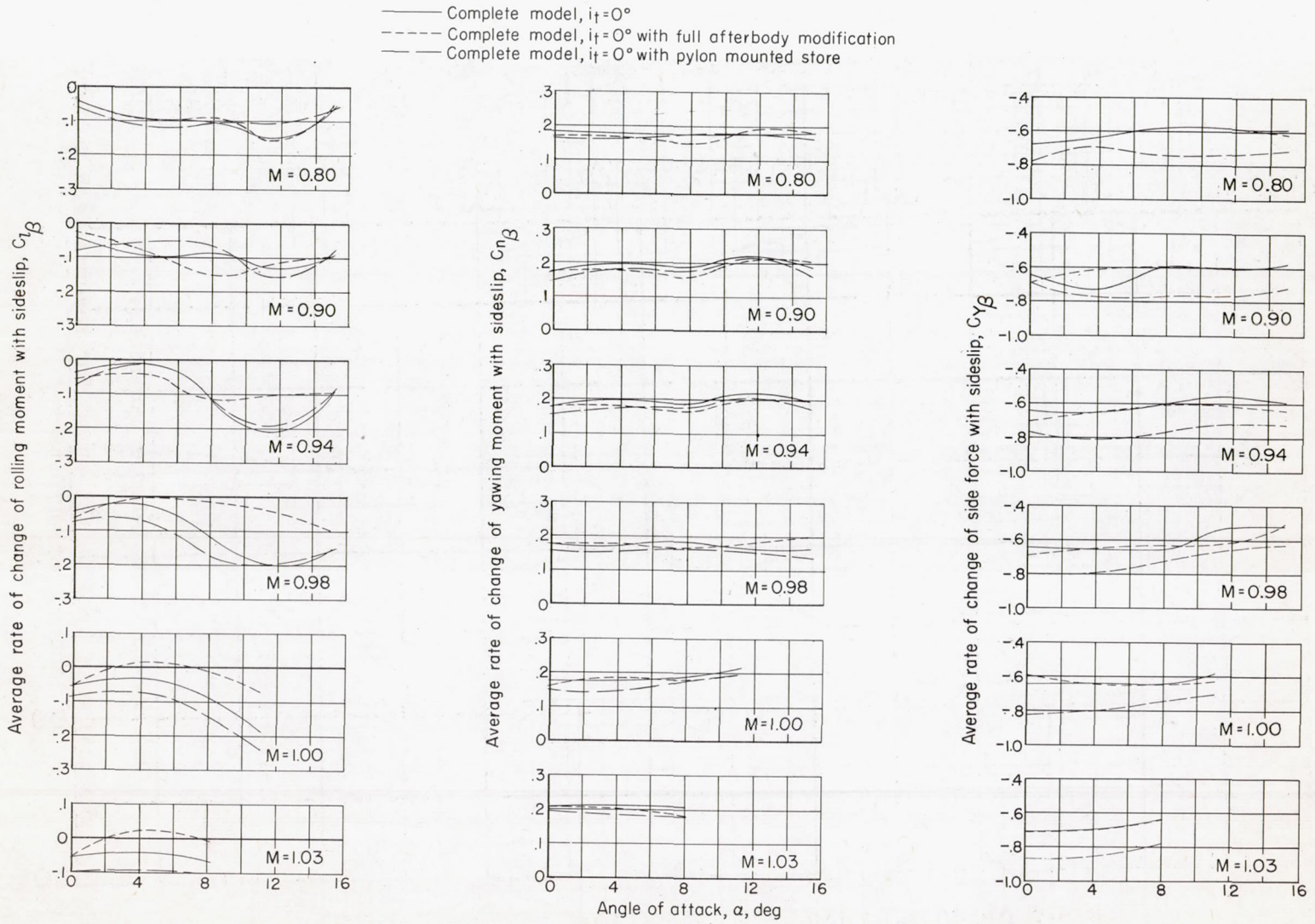
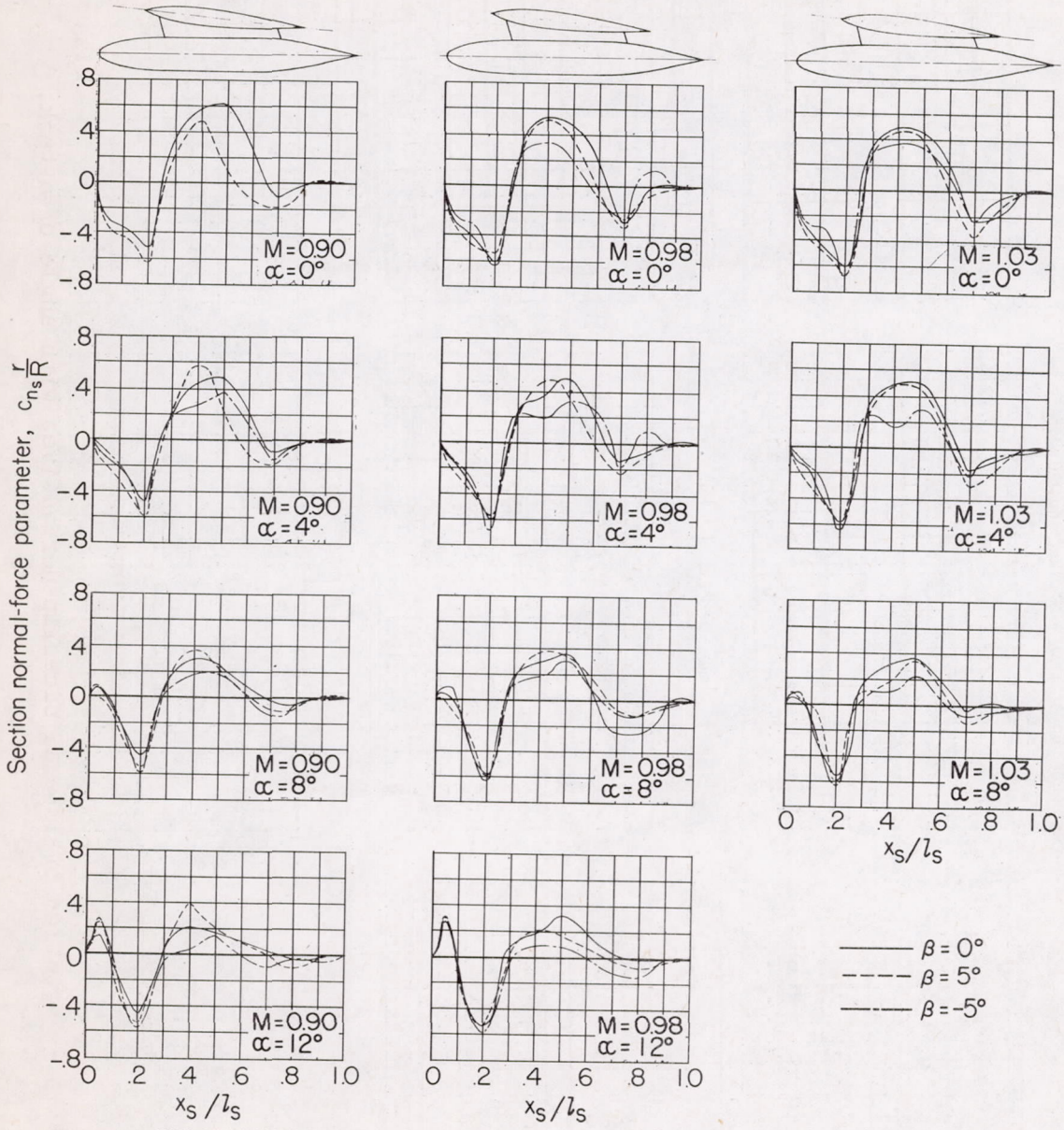
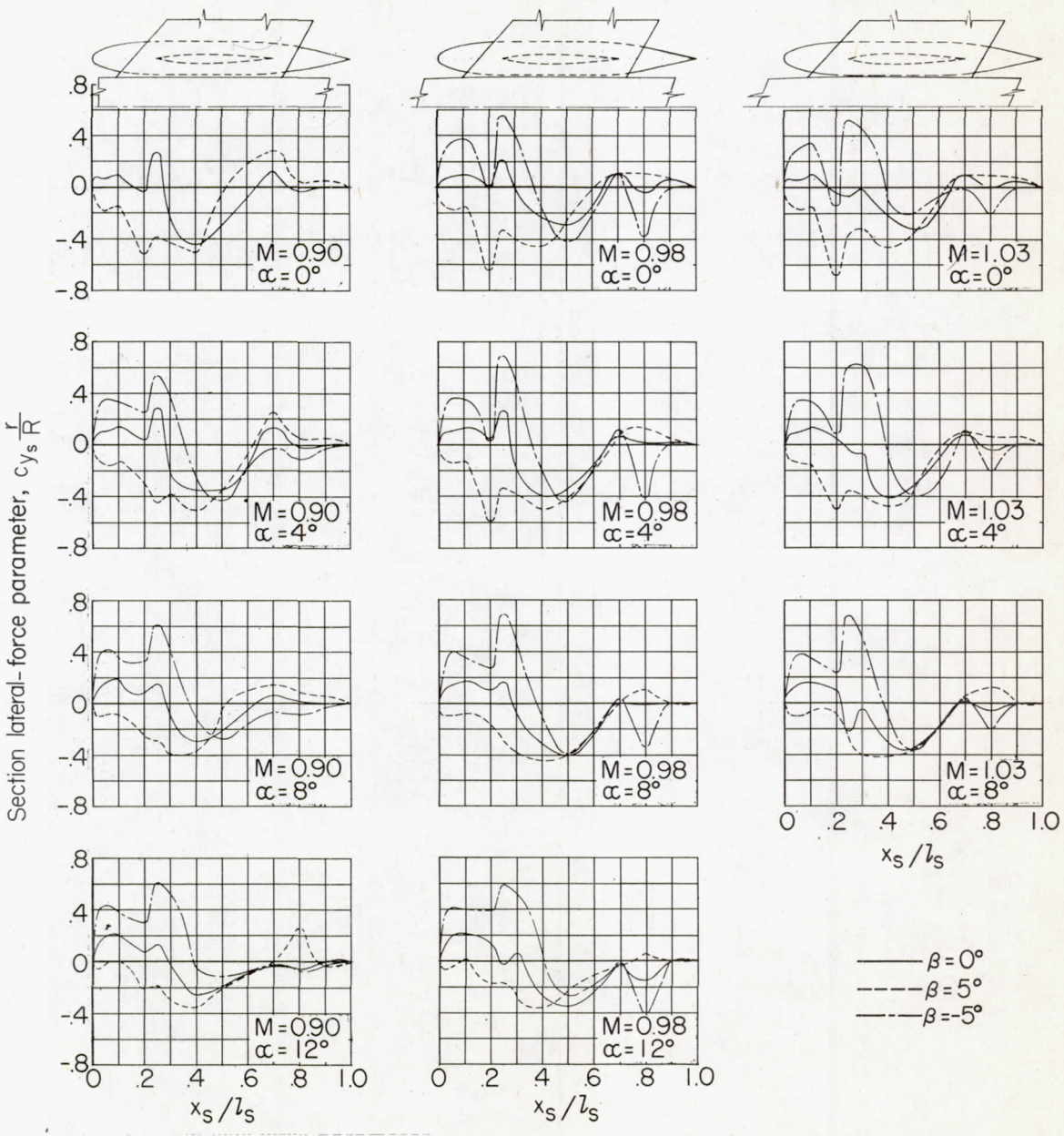


Figure 23.- Variation of lateral sideslip derivatives with angle of attack.



(a) Section normal-force parameter.

Figure 24.- Distribution of load on the store for several Mach numbers and angles of attack.



(b) Section lateral-force parameter.

Figure 24.- Concluded.

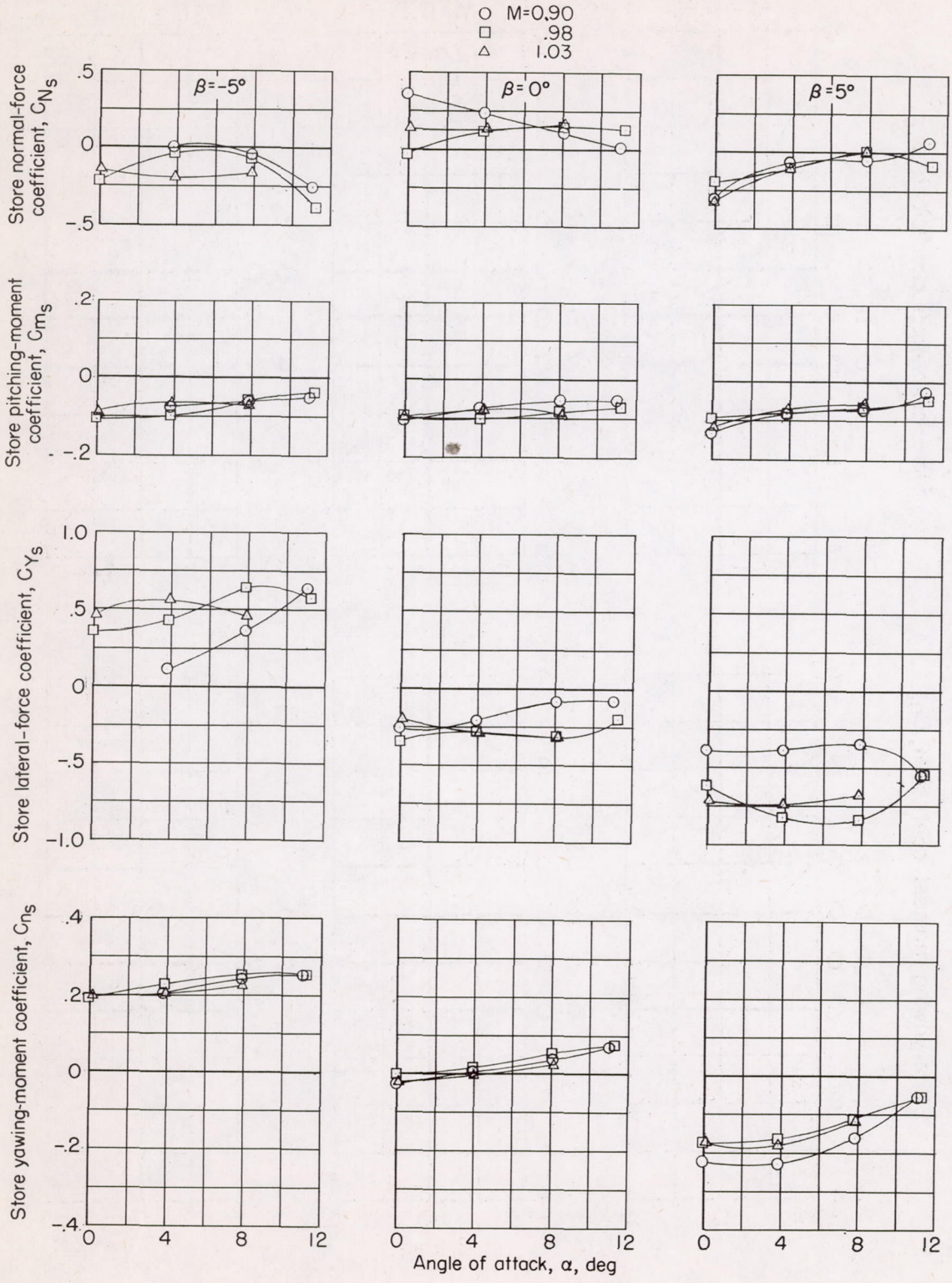


Figure 25.- Store force and moment coefficients.

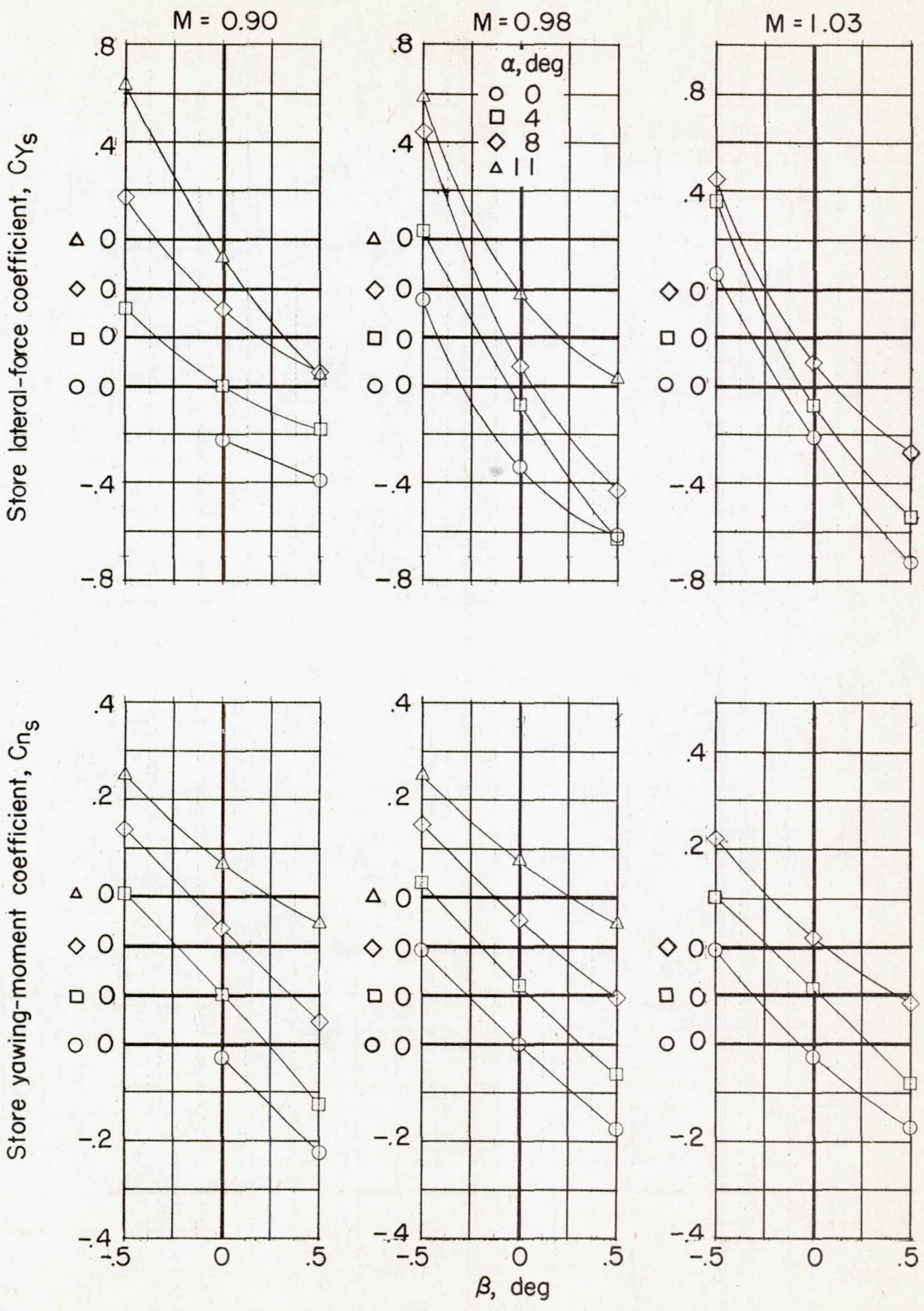


Figure 26.- Variation of store lateral force and yawing moment with angle of sideslip β for several Mach numbers.

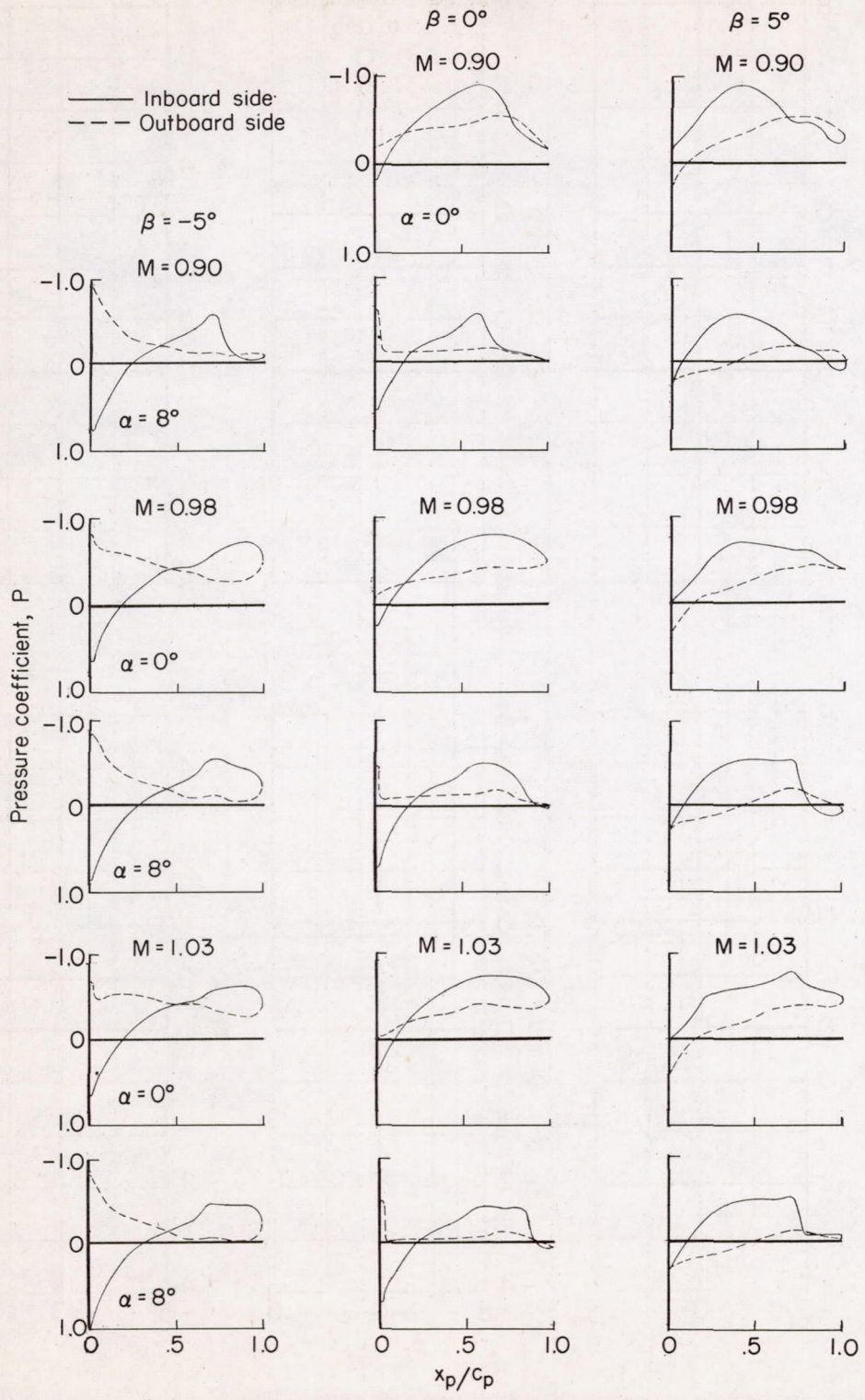


Figure 27.- Pylon chordwise pressure distributions at two angles of attack for several Mach numbers.

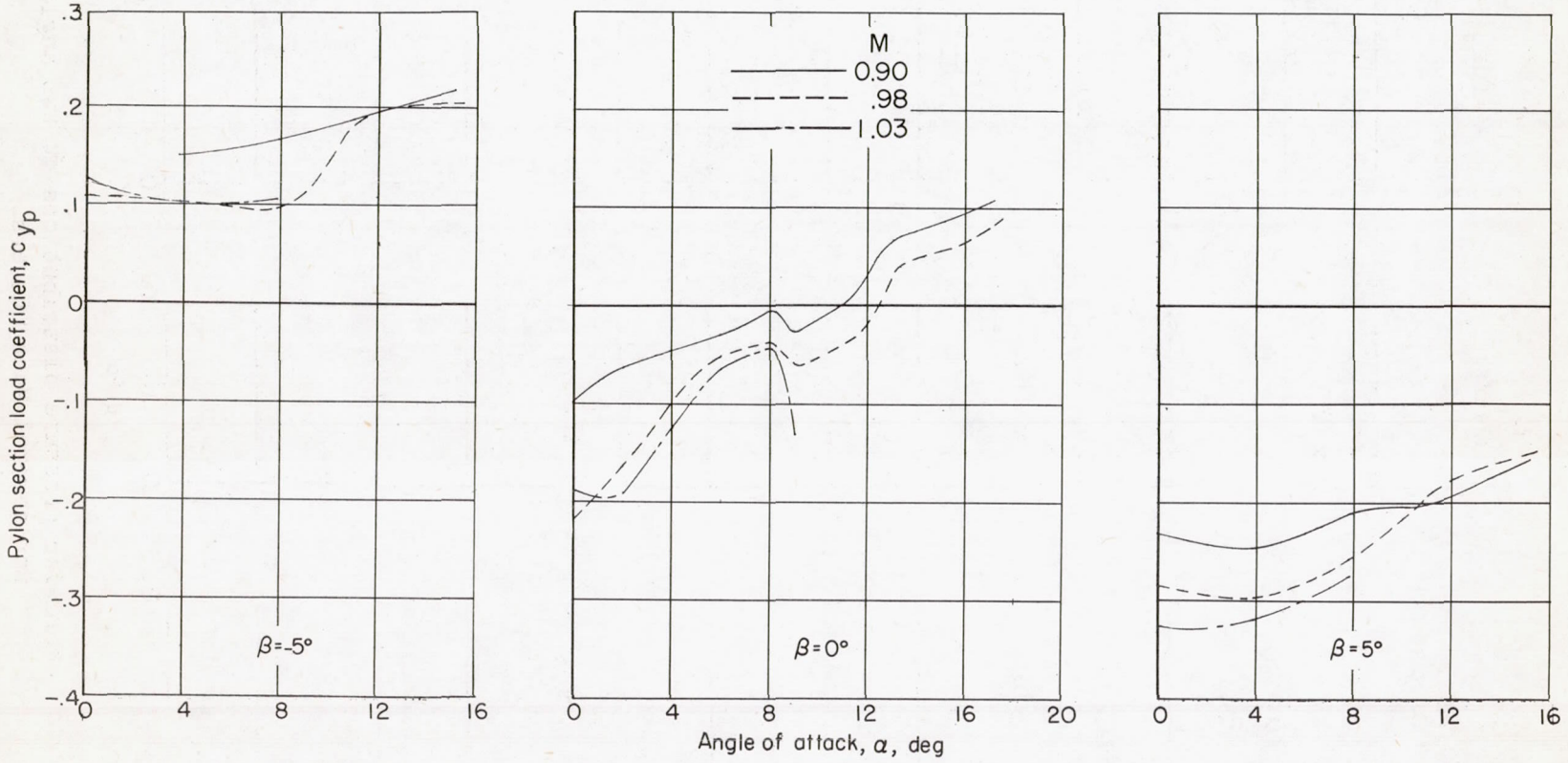


Figure 28.- Pylon section load coefficient for sideslip angles of 0° and ±5° at several Mach numbers.

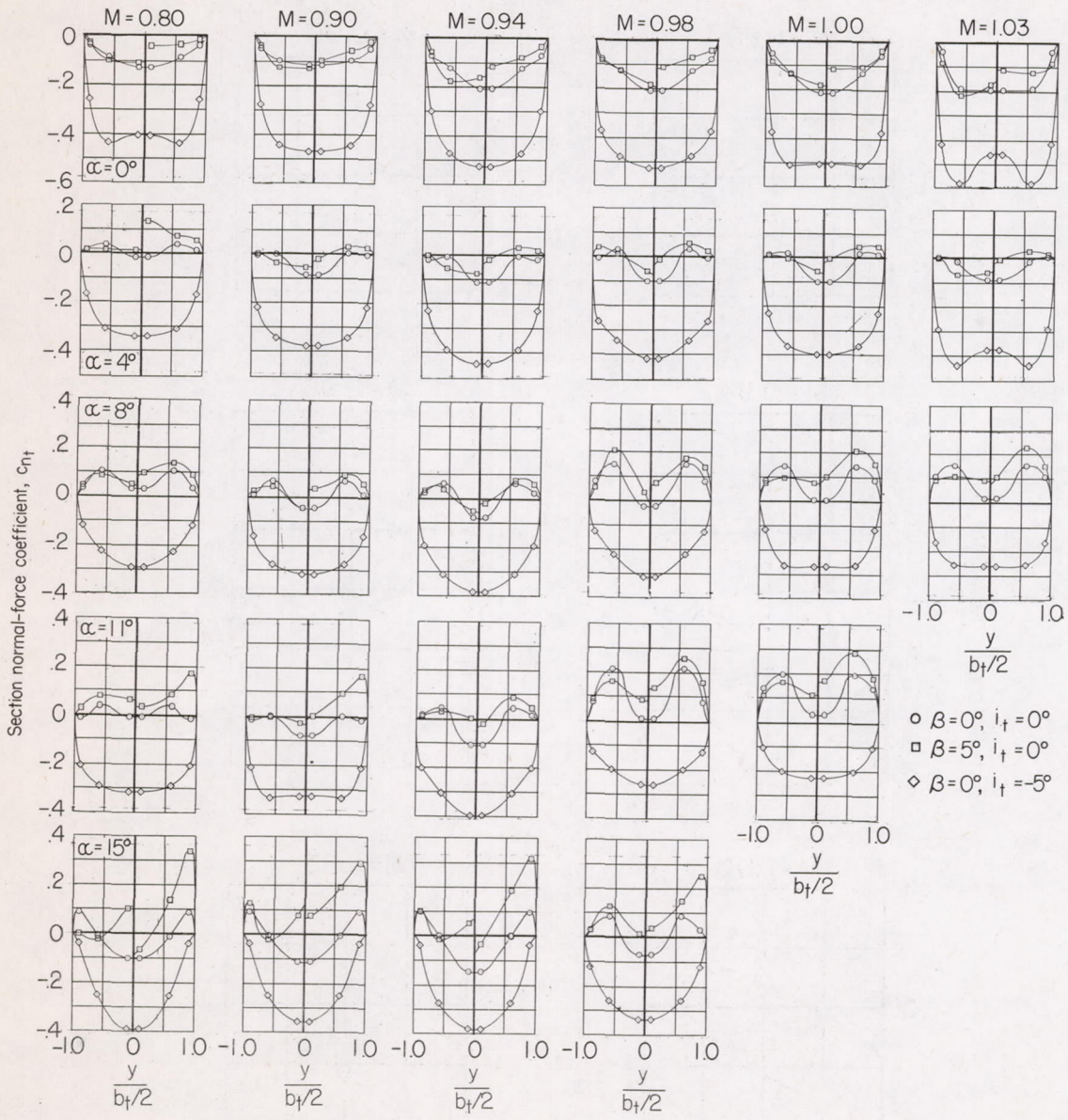


Figure 29.- Load distributions on the horizontal tail. Complete basic model. (Upstream view.)

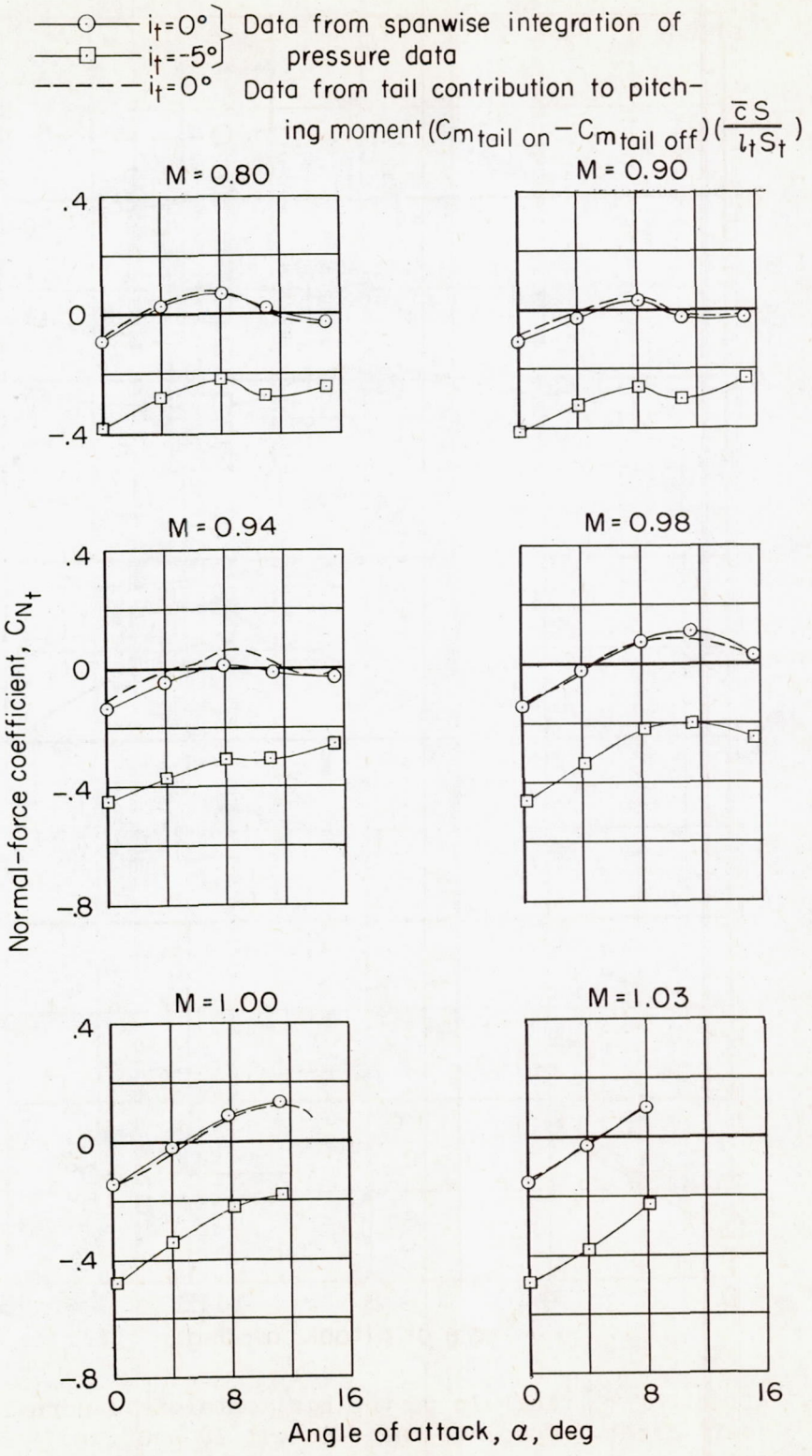


Figure 30.- Effect of angle of attack on the horizontal-tail-normal-force coefficient. Complete basic model; $i_t = 0^o$ and -5^o; $\beta = 0^o$.

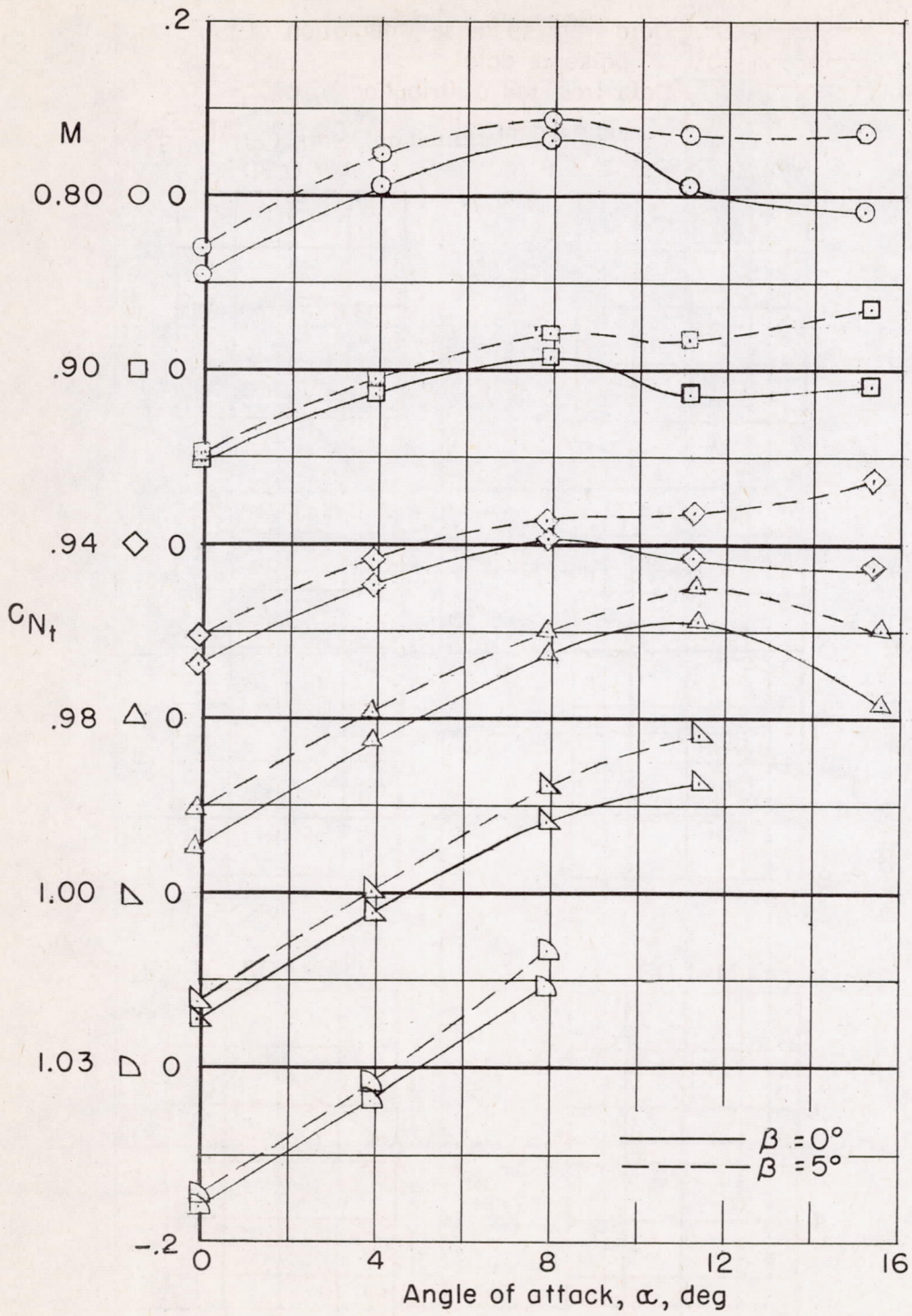


Figure 31.- Effect of 5° sideslip on the horizontal-tail-normal-force coefficient. Complete basic model; $i_t = 0°$.

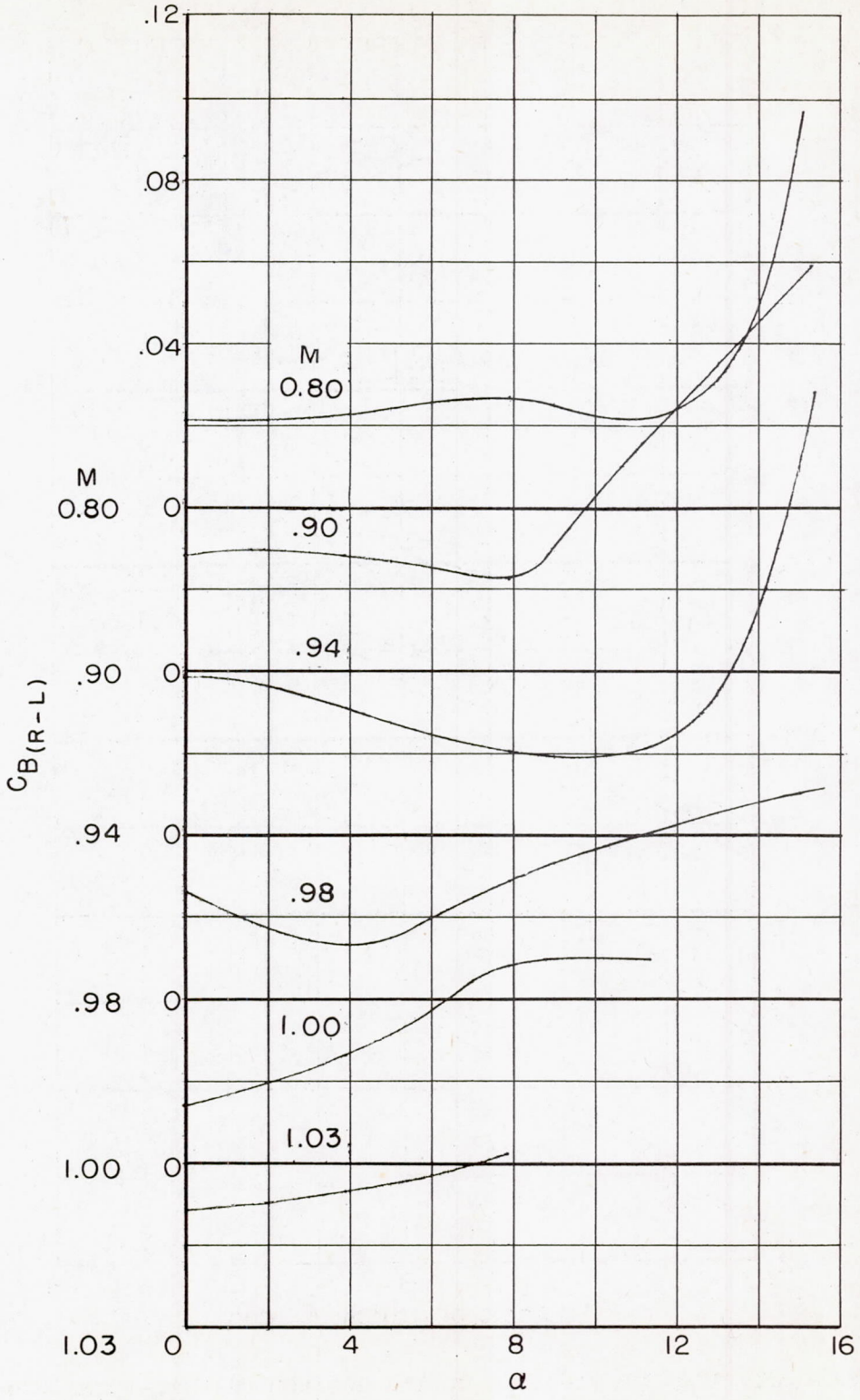
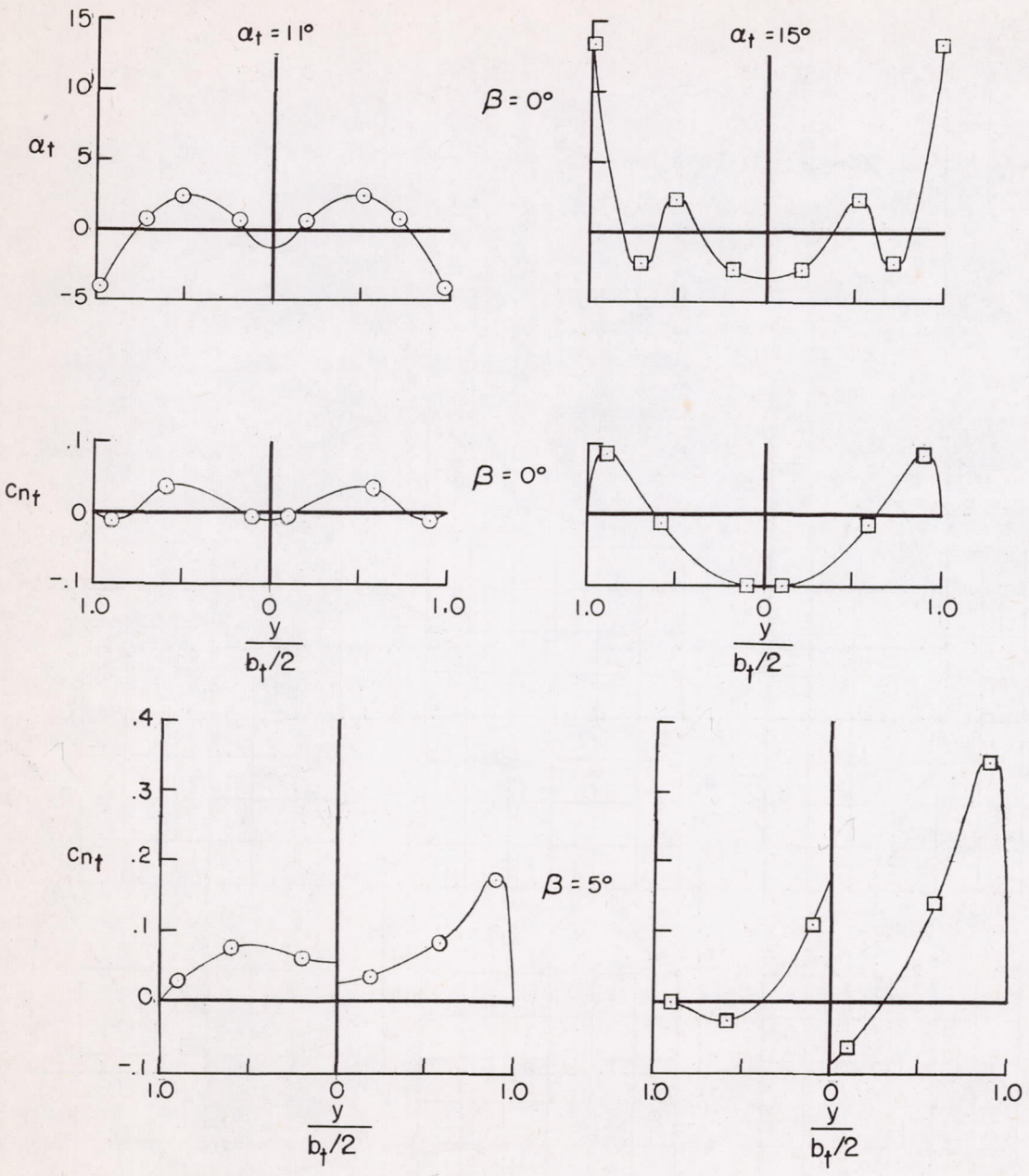
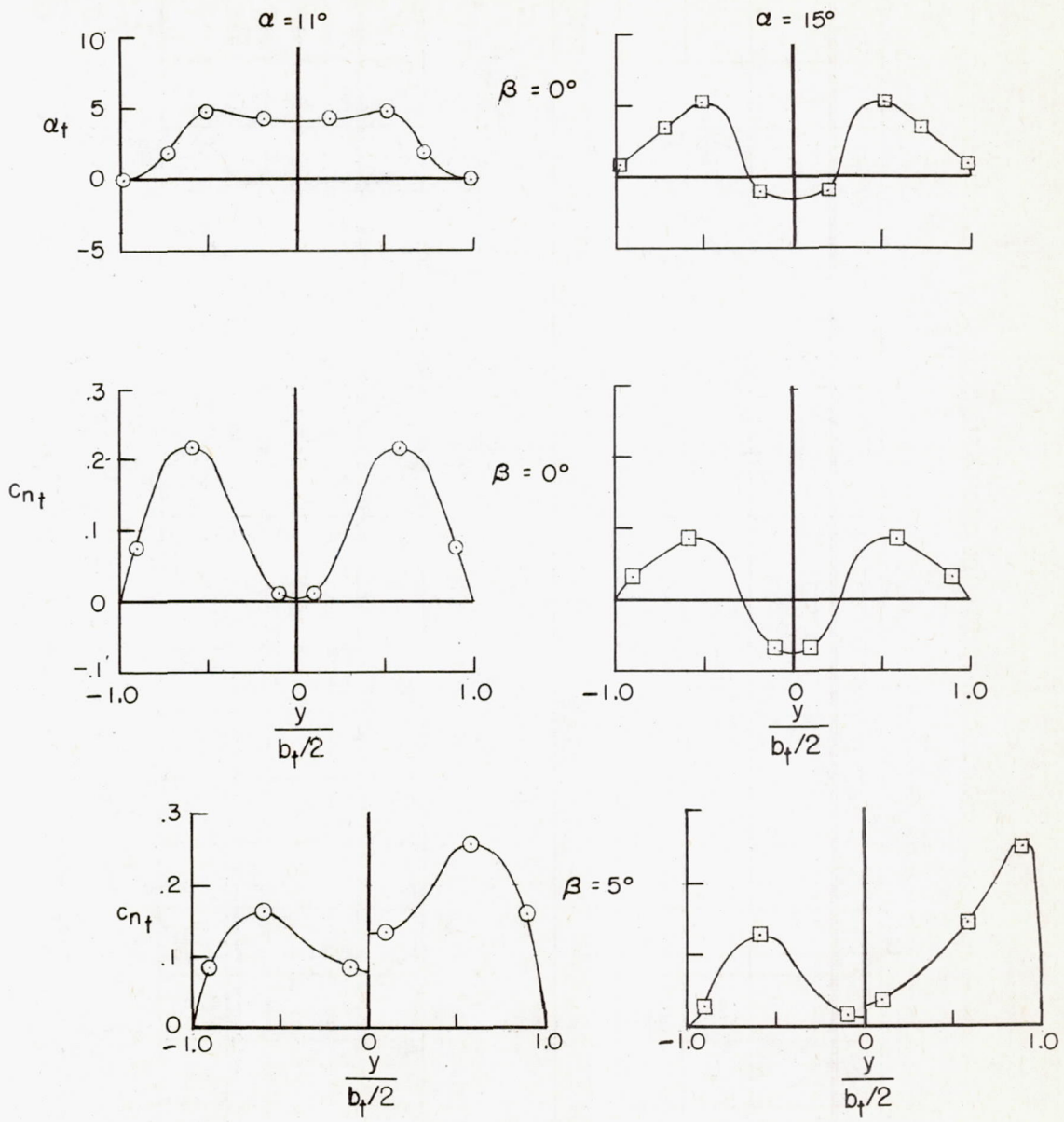


Figure 32.- Horizontal-tail asymmetric root bending moment at $\beta = 5^{\circ}$ for the complete basic model.



(a) M = 0.80.

Figure 33.- Comparison of α_t with section load across tail span at $\beta = 0^\circ$ and 5°.



(b) M = 0.98.

Figure 33.- Concluded.

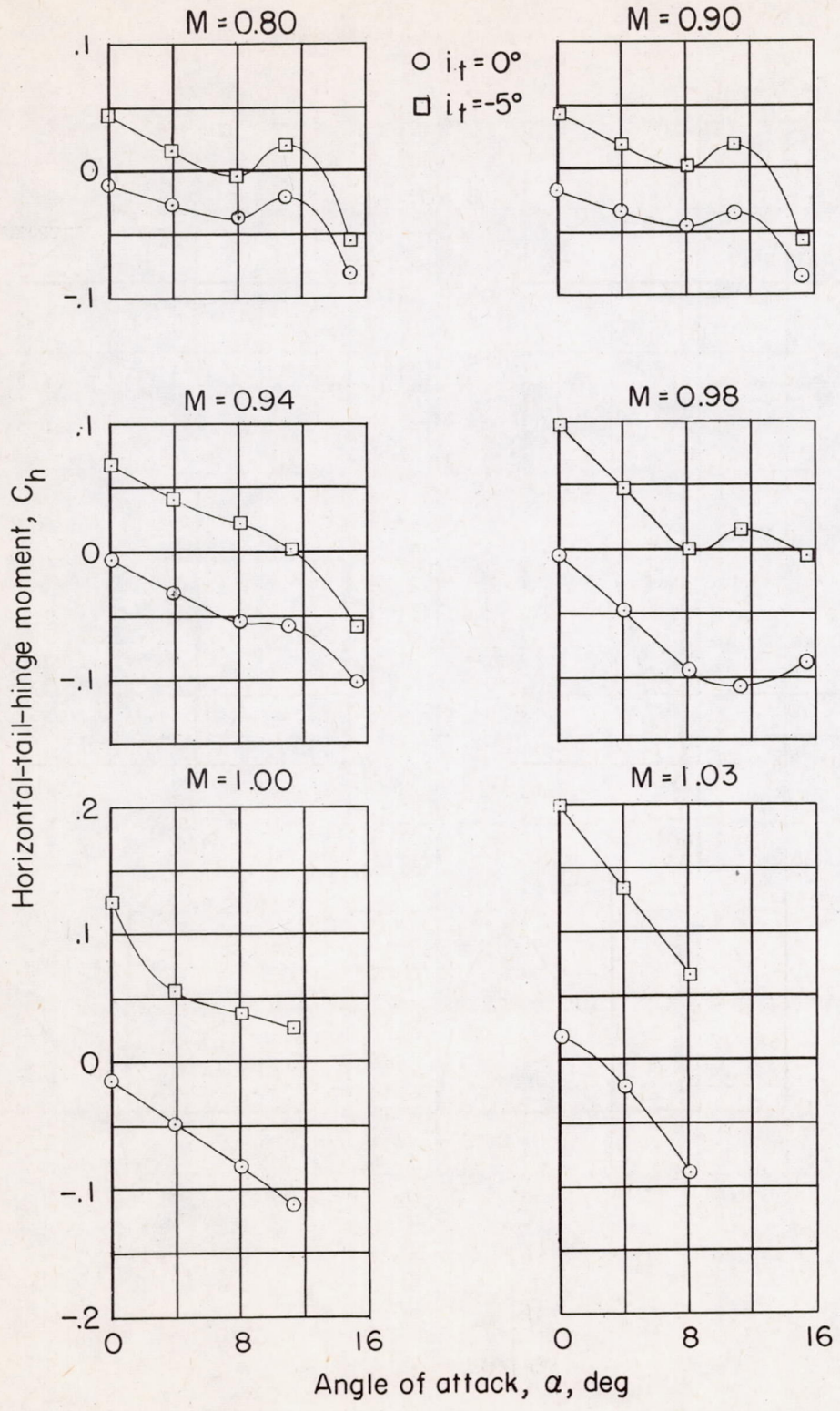


Figure 34.- Effect of angle of attack and Mach number on the horizontal-tail hinge moment.

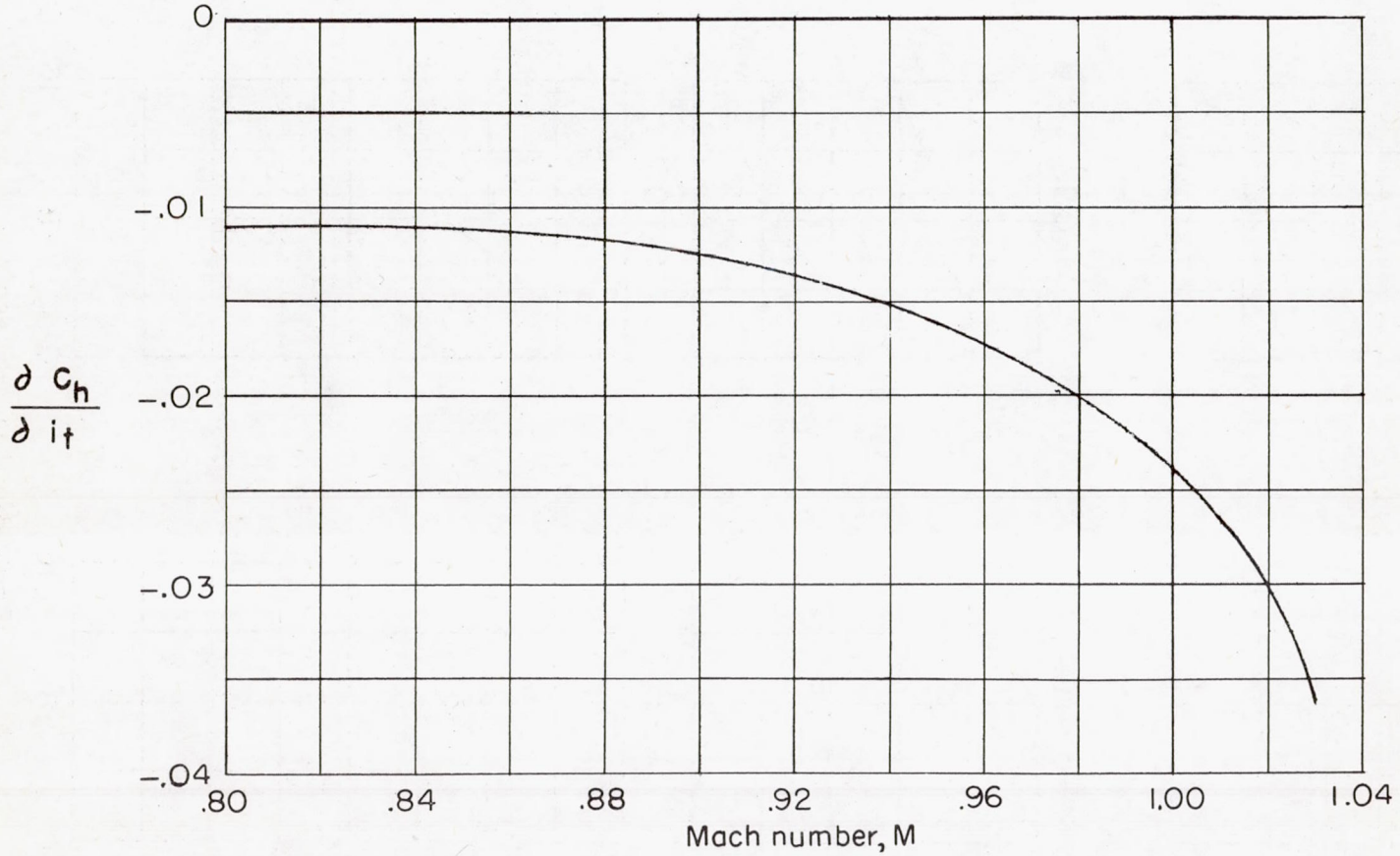


Figure 35.- Average rate of change of hinge-moment coefficient with horizontal-tail incidence through the Mach number range. (Averaged over an angle-of-attack range of 0° to 4°.)

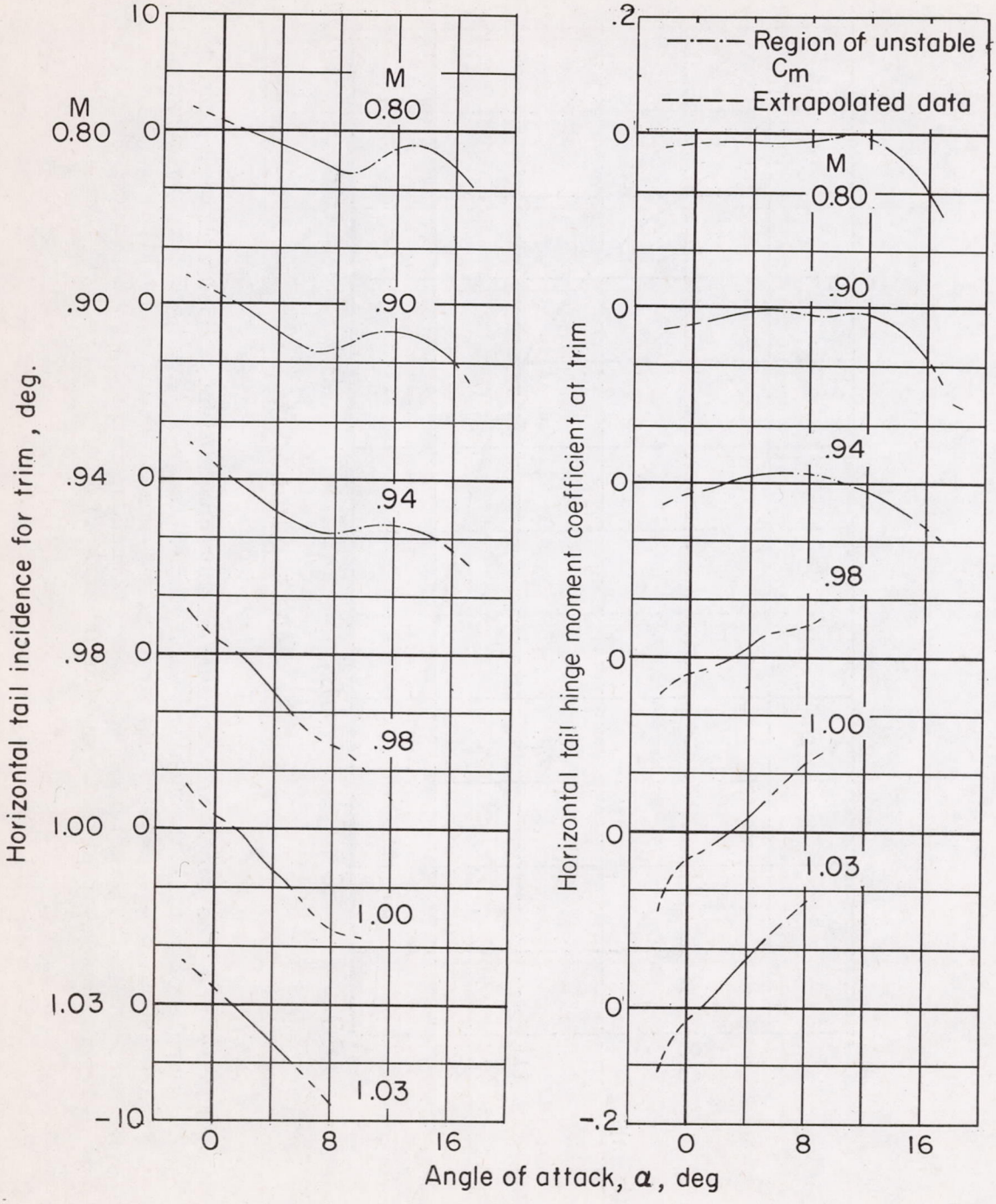


Figure 36.- Effect of angle of attack and Mach number on the horizontal-tail incidence angle and hinge-moment coefficient for trim.

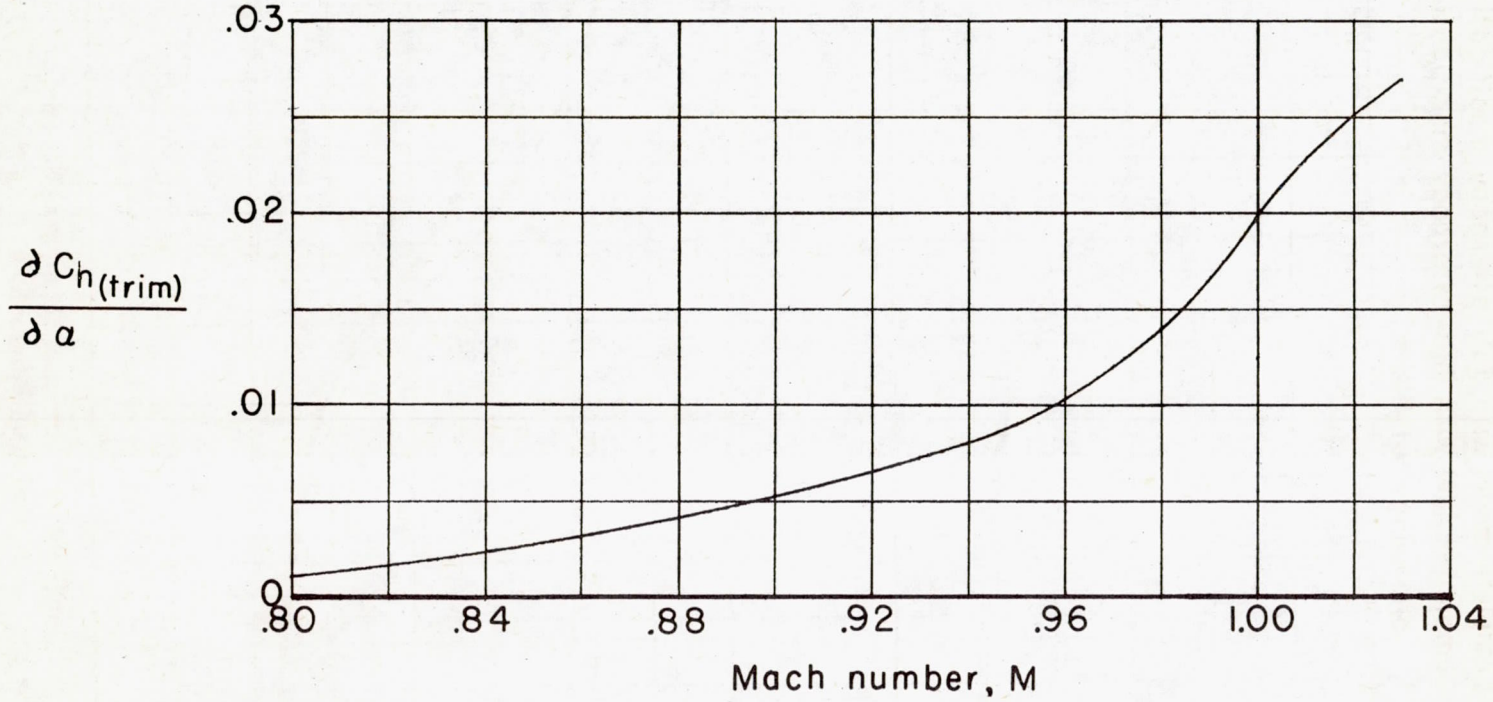


Figure 37.- The slope of the hinge-moment coefficient (model trimmed) with angle of attack through the Mach number range. (Averaged for the range between $\alpha = 0^{\circ}$ and 4°.)

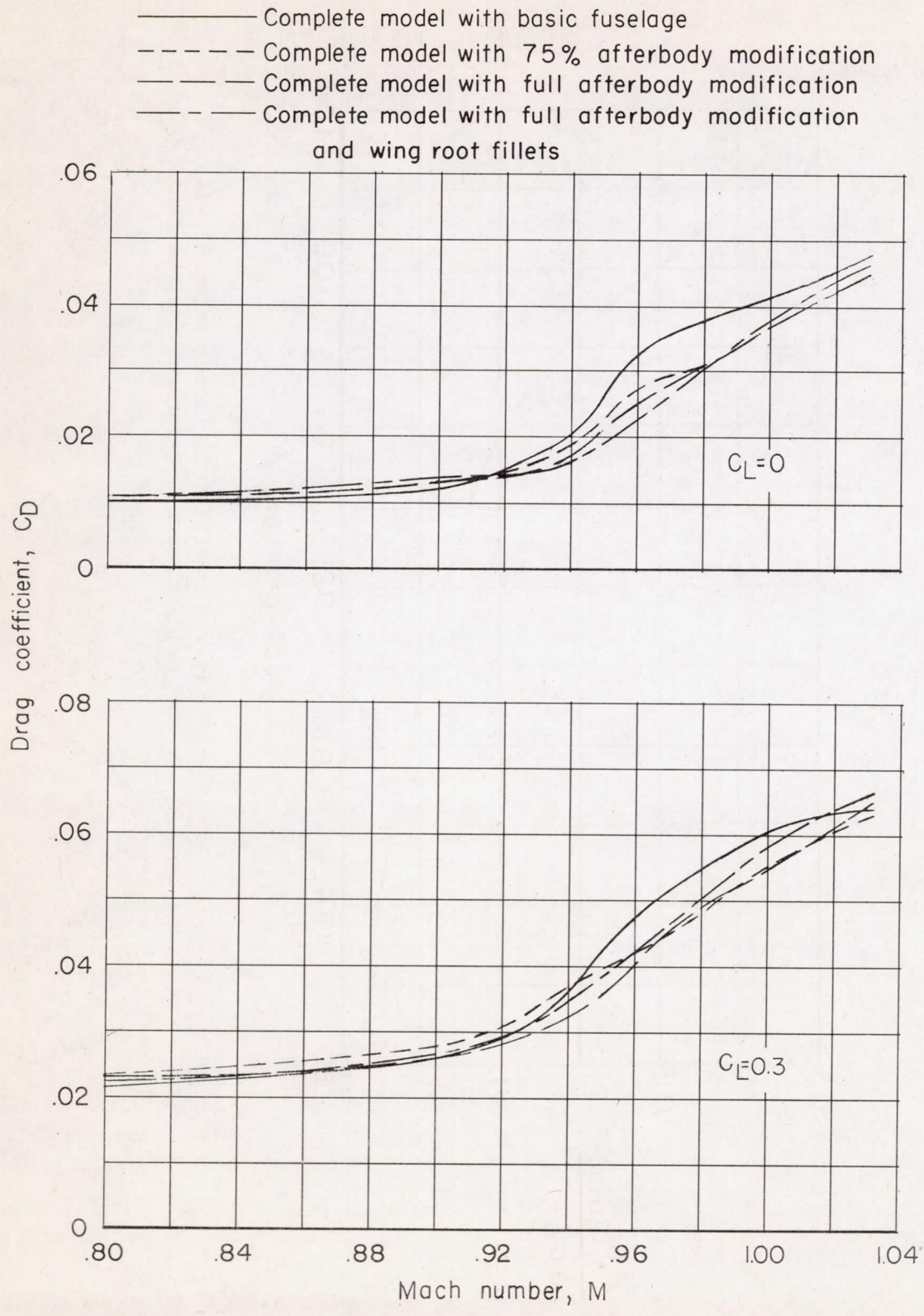


Figure 38.- Effect of various cross-sectional-area modifications on drag.